UT GSBS Dissertations and Theses (Open Access)　　　　Graduate School of Biomedical Sciences

5-2010

Measurement of the vascular input function in mice for DCE-MRI

Dustin K. Ragan

The TMC LIBRARY
Health Sciences Resource Center

MEASUREMENT OF THE VASCULAR INPUT FUNCTION IN MICE FOR DCE-MRI

by

Dustin K. Ragan, M.S., B.A.

APPROVED:

_____
Supervisory Professor, James A. Bankson, Ph. D

_____
John D. Hazle, Ph. D

_____
Edward F. Jackson, Ph. D

_____
R. Jason Stafford, Ph. D

_____
Valen E. Johnson, Ph. D

_____

APPROVED:

_____
Dean, The University of Texas
Graduate School of Biomedical Sciences at Houston

MEASUREMENT OF THE VASCULAR INPUT

FUNCTION IN MICE FOR DCE-MRI

A

DISSERTATION

Presented to the Faculty of
The University of Texas
Health Science Center at Houston
and
The University of Texas
M. D. Anderson Cancer Center
Graduate School of Biomedical Sciences
in Partial Fulfillment

of the Requirements

for the Degree of

DOCTOR OF PHILOSOPHY

by

Dustin K. Ragan, M.S., B.A.
Houston, Texas

May, 2010

Dedication

To my grandfather, Milford Ragan

To Pamela Smith

To mom and dad

To my beloved wife Gwen

Acknowledgements

I would like to acknowledge my advisor, James Bankson for his time, guidance, and support during my dissertation work. I would like to thank my committee, John Hazle, Edward Jackson, R. Jason Stafford, and Valen Johnson, for their time, feedback, and generosity when scheduling committee meetings.

My wife, Gwendolyn Hoben, has been beyond patient and understanding in all of this. Her love and support has kept me sane and able to keep on going through it all. Thank you, my darling.

My parents, Ken and Jennie Ragan, have supported me before and through grad school. Thanks mom. Thanks dad.

My colleagues through grad school have been invaluable fountains of ideas, targets for venting, friends, and just a darn good group of people. I would like to extend particular thanks to Marc Ramirez, Blake Cannon, Ryan Bosca, Hua Ai, Aziz Poonawalla, Rebecca Marsh, and Jennifer O'Daniel.

I would also like to thank God and coffee. Both of them are essential to my life.

Abstract

DCE-MRI is an important technique in the study of small animal cancer models because its sensitivity to vascular changes opens the possibility of quantitative assessment of early therapeutic response. However, extraction of physiologically descriptive parameters from DCE-MRI data relies upon measurement of the vascular input function (VIF), which represents the contrast agent concentration time course in the blood plasma. This is difficult in small animal models due to artifacts associated with partial volume, inflow enhancement, and the limited temporal resolution achievable with MR imaging. In this work, the development of a suite of techniques for high temporal resolution, artifact resistant measurement of the VIF in mice is described. One obstacle in VIF measurement is inflow enhancement, which decreases the sensitivity of the MR signal to the presence of contrast agent. Because the traditional techniques used to suppress inflow enhancement degrade the achievable spatiotemporal resolution of the pulse sequence, improvements can be achieved by reducing the time required for the suppression. Thus, a novel RF pulse which provides spatial presaturation contemporaneously with the RF excitation was implemented and evaluated. This maximizes the achievable temporal resolution by removing the additional RF and gradient pulses typically required for suppression of inflow enhancement. A second challenge is achieving the temporal resolution required for accurate characterization of the VIF, which exceeds what can be achieved with conventional imaging techniques while maintaining adequate spatial resolution and tumor coverage. Thus, an anatomically constrained reconstruction strategy was developed that allows for sampling of the VIF at extremely high acceleration factors, permitting capture of the initial pass of the contrast agent in mice. Simulation, phantom, and *in vivo* validation of all components were performed. Finally, the two components were used to perform VIF

measurement in the murine heart. An *in vivo* study of the VIF reproducibility was performed, and an improvement in the measured injection-to-injection variation was observed. This will lead to improvements in the reliability of quantitative DCE-MRI measurements and increase their sensitivity.

Table of Contents

Table of Figures

List of Tables

List of Abbreviations

AATH ....Adiabatic approximation to the tissue homogeneity model

AIF ....Arterial input function

ART ....Algebraic reconstruction technique

CACTUS.................................... Cardiac anatomy constrained, temporally unrestricted sampling

CV ....Coefficient of variation

DCE .... Dynamic contrast enhanced

DSC...Dynamic susceptibility contrast

ECG ....Electrocardiography

EES ....Extracellular extravascular space

FBP .... Filtered back projection

FPLP ....First pass leakage profile

FOV .... Field of view

FWHM...Full width half max

HYPR...Highly constrained projection reconstruction

IAUC...Initial area under the curve

ID .... Inner diameter

LV ....Left ventricle

MRI.. Magnetic resonance imaging

RF .... Radio frequency

RIGR...Reduced-encoding imaging by generalized-series reconstruction

RMS...Root-mean-square

ROI ....Region of interest

1 Hypothesis and Specific Aims

Tumor growth and progression is intertwined with the growth and development of its associated microvasculature (1). As a result of this relationship, vascular changes in response to therapy are desirable endpoints in preclinical studies of novel interventions (2). Dynamic-contrast enhanced (DCE) magnetic resonance imaging (MRI) enables interrogation of the microvasculature by investigating the dynamics of the uptake and clearance of an exogenous contrast agent, which will be altered by the characteristics of the vasculature in and around tumors (3). DCE-MRI is used both clinically, in the diagnosis (4) and in treatment response monitoring of cancer (5), and investigationally (6-8) in humans, as well as in animal models of disease, with unique and prominent challenges found in the latter.

Quantitative analysis of DCE-MRI data frequently uses pharmacokinetic models(9) to relate the uptake of contrast agent into tissue to the concentration time course in the blood plasma, known as the vascular input function (VIF), and subsequently producing a set of pharmacokinetic parameters. These descriptive parameters permit expressing DCE-MRI data as physiologically meaningful parameters which are related to quantities such as microvascular volume, flow and permeability. Accurate and precise measurement of the VIF, although required for accurate and reproducible parameter measurement, is challenging. Blood vessels are not ideal locations in which to acquire MR data, as artifacts are associated with flowing blood; these artifacts are dependent on the orientation of the blood vessel with regard to the slice and are thus unpredictable. The small size of blood vessels can introduce substantial partial volume effects that depend upon the relationship between the vessel and the acquisition matrix, again resulting in unpredictability. Additionally, small animals have low blood volumes and fast heart rates (over 300 bpm(10)). This introduces very rapid VIF kinetics,

placing difficult demands on the spatial and temporal resolution of the VIF

measurement. These demands are difficult to meet while also providing adequate sampling of

the tumor tissues.

The precision of VIF measurements needs to be increased to improve the precision of

pharmacokinetic parameter measurements in small animal imaging. The objective of this

research is to develop methods for measuring the VIF in a manner that satisfies the need for

both high temporal sampling rates and freedom from artifacts. For the sake of providing a

basis for quantitative comparison of the measurements, it is convenient to express the VIF as a

set of parameters fit to a biexponential model. **We hypothesize that when VIFs measured in

the heart using a highly subsampled acquisition and reconstruction strategy and flow

suppressive RF excitation are compared to VIFs measured in cerebral vessels, subsecond

temporal resolution of the VIF will be achieved and reduced coefficients of variance of the

biexponential parameters will be achieved.** This hypothesis was tested in the following

specific aims:

1. Develop, characterize, and test a novel RF excitation pulse for flow suppression.

A family of RF pulses that produce spoiled regions adjacent to the primary slice were

developed. These provided spatial presaturation in the regions adjacent to the slice, allowing

for steady state imaging of inflowing spins, reducing the flow enhancement effect. The

efficacy of the pulse for the suppression of inflow enhancement was demonstrated in

simulations, phantom, and *in vivo*, and an improvement in the sensitivity of the MR signal

measurement to the presence of contrast agent was demonstrated.

**2. Develop, characterize, and test a novel constrained reconstruction technique to

allow analysis of data from a highly undersampled data set.** A novel constrained

reconstruction technique which permits measurement of the signal in regions of interest within

a slice in the heart using very large undersampling factors was developed. Simulations and *in vivo* data testing was performed to demonstrate that the algorithm provides an accurate interpretation of the acquired data in the presence of both dynamic contrast enhancement and cardiac motion.

3. Compare the characteristics of VIFs in a population of healthy mice using both conventional and developed techniques. A population of eight mice was individually injected with contrast agent and the resulting VIFs were measured. Each mouse was injected three times with contrast agent, and a sufficient delay was allowed between injections for clearance of the contrast agent from blood and soft tissue. The coefficients of variations (CV) of a parametric representation of the VIF were compared to determine the intra-subject reproducibility of the pharmacokinetic parameters.

2 Introduction

2.1 Dynamic Contrast Enhanced MRI

Pathological conditions frequently involve the microvasculature and associated blood flow of the affected tissues. Angiogenesis is a prominent example from cancer models, for without the development of new blood vessels, tumors are incapable of growth beyond the diffusion range of oxygen (1), which is a few tenths of a millimeter (11). The growth and decay of the tumor vasculature can therefore provide information about the response of tumors to therapy, and the use of non-invasive imaging modalities to probe the microvascular characteristics of tissue is critical to biomedical research (2). This may be achieved by exploiting the fact that vessels produced by tumors are often malformed and leaky, resulting in hyperpermeability to small molecules, such as contrast agents (12), producing signal changes which may be observed using advanced imaging techniques.

MRI is widely used for non-invasive investigation of pathology because of its excellent soft tissue contrast and sensitivity to a wide variety of biochemical effects (13). In particular, MRI may be used to dynamically observe changes in tissue contrast due to the uptake of exogenous contrast agents. Dynamic Contrast Enhanced-MRI is achieved by exploiting the T_1-shortening effects of contrast agents, while a focus on the T_2^*-shortening effects is the basis for Dynamical Susceptibility Contrast (DSC)-MRI. Both techniques are used in the study of microvasculature, with DSC more commonly used in studies of blood volume and flow in the brain with an intact blood brain barrier, and DCE generally used in studies of microvascular permeability and perfusion in the body (14,15) and in brain tumors(16). This work is primarily concerned with DCE-MRI applications in small animal models of cancer.

DCE-MRI has been found useful in the management of many tumor types, which underscores its relevance to a wide variety of models. It has been found, in either qualitative or quantitative form, to be a sensitive and specific technique for the detection and staging of disease, with examples including, but not limited to, breast cancer (17), prostate cancer (18), and bone marrow lesions (19), and in many cases it has been shown to be effective for the monitoring of patient response to therapy (20,21). Quantification becomes more important preclinically, in which changes in vasculature measured using DCE-MRI are a common endpoint in drug development (2), and precise measurements are essential for reliable evaluation of efficacy. Quantification of DCE-MRI has shown much recent use in relation to the development of antiangiogenic drugs (22,23), response to radiation (24), and chemotherapy (25,26).

2.2 Data acquisition and analysis for quantitative DCE-MRI

A typical DCE-MRI protocol for quantification of dynamics consists of several sequences for localization and anatomic imaging. After these images are acquired, the pre-contrast T_1 of the tumor is often measured before dynamic data are acquired to enable calculation of the contrast agent concentration, although an assumed value may be used (27). Finally, a dynamic series of images is acquired, typically with a short-TR spoiled gradient echo sequence, during which a bolus of contrast agent is injected after the acquisition of a few baseline images. This sequence allows both a relatively high frame rate and short echo times, which minimizes T_2*-related dephasing produced by the contrast agent. The dynamic protocol must strike a difficult balance between high temporal resolution for measuring the uptake dynamics, spatial coverage, and high spatial resolution, which is required due to the heterogeneity of tumor tissue (28). Relatively fast uptake and clearance is expected in areas of

highly permeable vasculature, such as in many tumors, while in healthy tissue contrast agent extravasates and clears at a slower rate (29).

The analysis and interpretation of the dynamic MR data is most easily performed in terms of the contrast agent concentration, a physical quantity, as opposed to the MR signal, which has an arbitrary meaning and a non-linear relationship to the concentration. Because the MR signal depends indirectly on the contrast agent concentration through the relaxation rates, the path from MR signal to final measurement of the vascular state requires several steps and relies upon several measured, known, or assumed parameters.

In order to calculate the concentration levels *in vivo*, the signal time course is measured from the dynamically acquired images. For an ideal spoiled gradient echo sequence with perfect spoiling of the signal between excitations, the signal is given by the equation (30):

$$S = \rho \frac{\left(1 - e^{-TR/T_1}\right)\sin\theta}{1 - e^{-TR/T_1}\cos\theta} e^{-TE/T_2^*} \qquad \text{(Eq. 2.1)}$$

where S is the measured signal, ρ is a term including the spin density, as well the receiver gain and other constant factors, TE is the echo time, TR is the repetition time, θ is the excitation flip angle, and T_1 and T_2^* are the longitudinal and transverse relaxation times, respectively. When the signal changes dynamically, this is due to temporal dependence in T_1, caused in turn by the changes in the contrast agent concentration. Often the effects of a temporally varying T2* are ignored due to the use of a short echo time; ignoring these effects simplifies the necessary calculations (31).

The above equation can be solved for the T_1 of tissue after contrast agent administration, assuming that baseline values for the tissue signal and its longitudinal relation time are known. The equation for the time dependant T_1 becomes

$$T_1(t) = TR \left[\ln \left(\frac{1 - \Xi(t)\cos\theta}{1 - \Xi(t)} \right) \right]^{-1}, \text{ where}$$

(Eq 2.2)

$$\Xi(t) = \frac{S(t)}{S_0} \frac{1 - \exp\left(-TR/T_{1,0}\right)}{1 - \exp\left(-TR/T_{1,0}\right)\cos\theta}$$

(Eq 2.3)

and *S(t)* is the dynamically measured signal, S_0 is the baseline signal, $T_{1,0}$ is the native T_1 of the tissue, θ is the flip angle, and TR is the repetition time. The concentration can be calculated using the relation:

$$\frac{1}{T_1(t)} = \frac{1}{T_{1,0}} + r_1 C(t)$$

(Eq 2.4)

where C(t) is the contrast agent concentration as a function of time, and r_1 is the contrast agent T_1 relaxivity. This is a parameter of the contrast agent that describes the agent's effect on the T_1 relaxation rate. Values for this parameter, reported for human blood at 3T are 3.3 $M^{-1}s^{-1}$ for gadopentetate dimeglumine, 3.6 $M^{-1}s^{-1}$ for gadobutrol, and are 6.3 $M^{-1}s^{-1}$ for gadobenate dimeglumine.

2.3 Pharmacokinetic modeling of DCE-MRI Data

Three different modes are found in the analysis of dynamic uptake data: qualitative curve shape analysis, semi-quantitative analysis, and quantitative analysis. Although it is sometimes possible to interpret the shape of the tissue-enhancement curve directly to provide diagnostic information, this is not reproducible across imaging systems (32). It also relies on non-quantitative, subjective assessment and is thus not a useful approach for small animal DCE-MRI studies. Visual changes in enhancement curves are also much less sensitive indicators of changes in the tumor than quantitative analysis; a difference of approximately

50% in quantitative measurements is required to produce a perceptible qualitative change (33). As a result, small animal studies, which hope to detect smaller and earlier changes in the tumors require more rigorous quantification that is more sensitive and reproducible than curve-shape analysis provides.

Semi-quantitative analysis relies upon the calculation of an empirically useful descriptive parameter from the tissue uptake curve. These parameters include the initial area under the curve (IAUC) and the initial slope of the enhancement curve (34). Although they do not have directly interpretable physiological meanings, they have been used for many clinical applications (34). However, semi-quantitative analysis has been found to be less reproducible than a full kinetic analysis (35), and the lack of interpretability has led to a desire for analyses that are based on the physiology of tissue.

Quantitative analysis (34) is based upon simple physiological models which permit transforming the contrast uptake curves measured in tissue into physically meaningful terms. These models provide parameters which are sensitive to flow, permeability, and blood volume, although in some models their effects may become indistinguishable.

The models most frequently cited in the literature were adapted from the work of Kety, which is based in indicator-dilution theory (36), and the same models are generally used in both human and small animal imaging. Although many variations are present, the most common models present in literature related to the Tofts-Kermode model, which as presented here uses a consensus terminology from many early workers in the field of DCE-MRI (3). This model is derived from compartmental assumptions, that is, that blood and tissue are two well-mixed, disjoint units that exchange contrast agent, shown in Figure 2-1. The extracellular components of blood and tissue are assumed to be two pools which exchange contrast agent according to a differential equation(3):

$$\frac{dC_T}{dt} = K^{Trans}C_p - \frac{K^{Trans}}{v_e}C_T$$

<div align="right">(Eq 2.5)</div>

where K^{Trans} represents the forward transfer constant, a mixed term describing both flow and perfusion effects, and the concentrations in the blood plasma and tissue are C_p and C_T, respectively. The fractional extracellular extravascular volume is given by v_e.

The most general expression for K^{Trans} is (29):

$$K^{Trans} = \left[1 - \exp\left(-\frac{PS}{F(1-\text{Hct})}\right)\right]F\rho(1-\text{Hct})$$

<div align="right">(Eq 2.6)</div>

where F is the blood flow, Hct is the hematocrit, ρ is the tissue density, and PS is the permeability-surface area product. In the case of high perfusion, uptake is limited by flow and $K^{Trans} = F\rho(1-\text{Hct})$. In the case of high flow, $K^{Trans} = PS\rho$. When neither flow nor perfusion dominates, the two quantities are not distinguishable (3), in tumors the mixed case generally applies(8). An alternative parameterization with a second rate constant in place of the EES volume, $k_{ep} = K^{Trans}/v_e$ is also quite common. This allows consideration of the dynamics in terms of the mean residence time of the contrast agent instead of the volume of the EES. Tissue and blood plasma contrast agent concentrations are denoted by C_t and C_p, respectively. The blood plasma concentration is frequently given a special name, either the arterial input function (AIF), or the vascular input function (VIF). We use the term VIF exclusively in this work. The VIF represents the blood supply of the tissue, which is typically approximated by a measurement performed in a nearby artery or vein. These equations assume a lipophobic contrast agent that does not penetrate the cell walls; which leads to the factors accounting for the extracellular volume and the hematocrit. The convolution equation below is a solution to Eq. 2.5 (3):

$$C_T(t) = K^{Trans} C_p(t) * e^{-\frac{K^{Trans}}{v_e}t} \qquad\qquad \text{(Eq 2.7)}$$
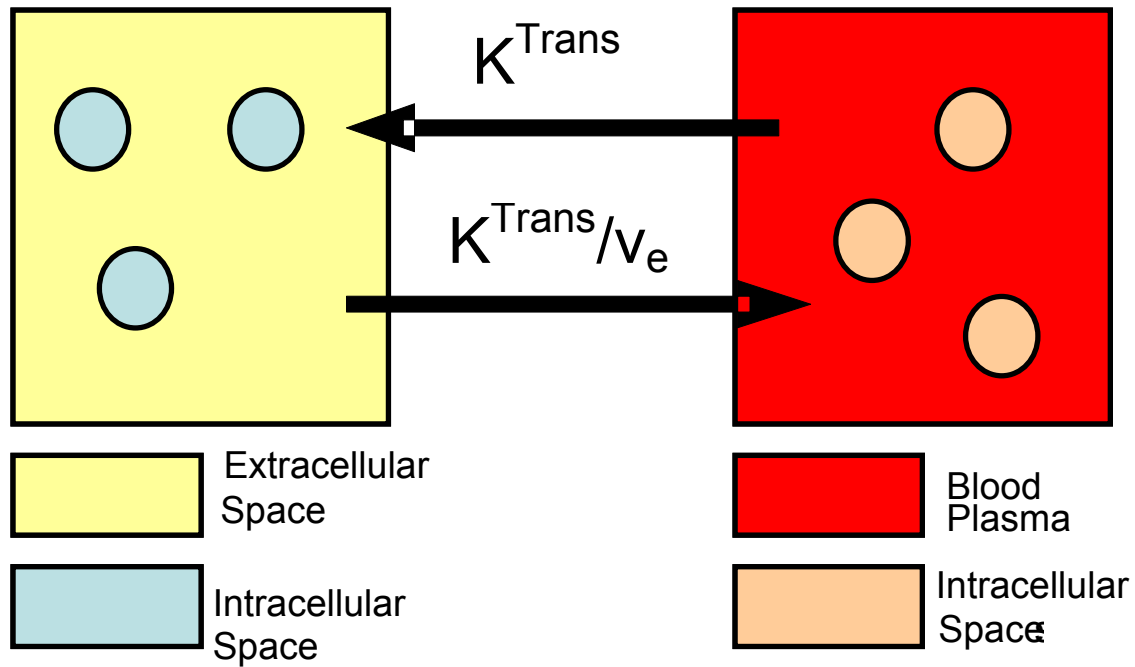
Figure 2-1 Diagram showing the differential compartmental model.

In practice, use of the two parameter model is often associated with spuriously large values for K^{Trans}, which result from the presence of blood vessels in the tissue voxel; this is known as the pseudopermeability artifact (37). A threshold of 1.2 min^{-1} is commonly used for identifying voxels that are corrupted by pseudopermeability (16). This criteria is strangely uncontroversial in the DCE-MRI literature, however, voxels which are only partially affected will not be identified by thresholding (38). No alternate threshold for small animal imaging has been proposed. These effects may be mitigated by the use of the extended model (39,40), where v_b is the fractional intravascular space:

$$C_T(t) = K^{Trans} C_p(t) * e^{-\frac{K^{Trans}}{v_e}t} + v_b C_p(t) \qquad\qquad \text{(Eq 2.8)}$$

An implicit assumption of this model is that there is a single T_1 behavior for both the intravascular space and the EES, which is equivalent to assuming fast proton exchange between vessels and tissue. This assumption has been experimentally tested and it was concluded that the assumption held in most tissues, with a notable exception in the cerebrovasculature resulting from the blood-brain barrier (41).

A simplification of the three-parameter model was put forth by Li (42), called the First-Pass Leakage Profile (FPLP) model, which only analyzes the first pass of the contrast agent in the blood. This simplifies calculations of pharmacokinetic parameters and allows for shortened acquisition times, which may be useful in cases of severe motion or a non-compliant patient. The simplified model assumes that no appreciable amount of contrast backflows from tissue into the blood over this interval, that is, neglecting k_{ep}. This model is not commonly used in small animal models.

Other models that are not based on compartmental assumptions have been proposed, most notably the adiabatic approximation to the tissue homogeneity model (AATH) (43,44), where

$$C_T(t) = C_p(t) * H(t) \tag{Eq 2.9}$$

$$H(t) = \begin{cases} F\rho(1-\text{Hct}), t < T_c \\ K^{Trans} e^{-\frac{K^{Trans}}{v_e}(t-T_c)}, t > T_C \end{cases} \tag{Eq 2.10}$$

In the above equation, T_c is the time that contrast agent spends in the capillary before entering the tissue, and other quantities are as previously defined. This model fails to be a compartmental model because it does not include the assumption that blood is well-mixed (45). Instead, it assumes that the blood dynamics occur on a much faster timescale than the exchange of contrast agent between blood and tissue. If the tissue is sampled faster than T_c, this model is able to separate flow and perfusion effects. When the temporal sampling rate is slower than T_c,

the model becomes indistinguishable from the three-parameter two-compartment model. In humans, values for T_c have been measured on the order of 40 s in a particular tumor model (46); in rats, values of approximately 11 s have been measured (47) using dynamic CT. The tissue homogeneity model itself is rarely used because it does not have a closed form solution when written as a function of time (43,48). Another variation of this model includes a distribution of capillary transit times within a single voxel (46).

Some investigators have used models that rely on the same contrast agent dynamics, but which explicitly account for the exchange of water between the intracellular space and the EES. Conventionally, it is assumed that water exchange is in the so-called fast exchange limit, in which water exchanges sufficiently rapidly to only have a single T_1 behavior in the voxel. This form of modeling introduces an additional parameter that describes the exchange rate of protons between the two components of tissue (49). The significance of these effects remains controversial (41,50).

An alternative to the use of an explicit model is to perform a non-parametric deconvolution to produce a residue function (51). This allows for improved fitting of the concentration time courses by avoiding model errors during the deconvolution step. Although interpretation of the residue curves for measurements of blood flow and blood volume is commonly done in DSC-MRI (52), there has not yet been a method for interpreting permeability in this context, other than fitting the residue curve itself to one of the aforementioned models (51).

Limited comparisons have been performed between the various pharmacokinetic models. Buckley performed a simulation study in which an independent model for blood transport was used to compare both forms of the two compartmental model and the AATH to the actual simulated values. The latter was capable of producing the most accurate results, but

also had the most strenuous requirements for temporal sampling and was subject to

the most difficulties in fitting. The extended Toft's model was found to avoid the

pseudopermeability artifact, but in general tended to overestimate K^{Trans} and underestimate v_p

(39).

Comparisons have also been performed using *in vivo* data. Harrar, *et al*. found in

glioma patients that the FPLP and the extended Tofts model provided comparable results, and

that both were considerably less sensitive to the pseudopermeability artifact than the two-

parameter Tofts model (37). Haroon, *et al*., directly compared the FPLP and the two-parameter

Tofts model, and came to a similar conclusion regarding the presence of the

pseudopermeability artifact (38).

2.4 Uncertainty in the calculation of kinetic parameters

Fundamentally, the calculation of the pharmacokinetic parameters relies on two

measurements: the concentration time courses in tissue and that in blood. Uncertainty and

errors in those two measurements contribute to uncertainty and errors in the final calculated

parameters. Because concentration measurements in MRI are indirect, several quantities,

which are themselves subject to uncertainty, are required for precise and accurate calculation of

the pharmacokinetic parameters. These quantities include the baseline T_1 of blood and tissue,

the flip angle used to excite the spins in the dynamic acquisition, the T_1 relaxivity of the

contrast agent used, and the individual signal time courses of both tissue and blood (53).

The variations in the final pharmacokinetic parameters that result from errors in the

individual input parameters have been estimated by various investigators. While the contrast

agent relaxivity affects the absolute values of the parameters measured, it is constant across an

experiment and does not introduce imprecision into the final values (53). It has been argued

that the accuracy of the baseline T_1 measurement is not a major factor in the accuracy and

precision of the final kinetic parameter measurement. Specifically Dale, et al. (53),

found that uncertainties in measuring the baseline T_1 resulted in a coefficient of variation (CV)

in the final kinetic parameters of between 5 to 6%, over a wide range of T_1 and parameter

values, and Haacke, et al.(27) even found that reproducibility was enhanced by assuming a

constant value for T_1. The effects of flip angle errors depend on the analysis performed, but

proper measurement of the transmit field strength B_1 (*e.g.*, (54)) and appropriate choice of

protocols can reduce the error to a few percent, and this is less problematic in small animal

imaging due to the small size of the RF coils (55).

Both the temporal sampling rate of tissue (56) and the spatial resolution (28) affect the

accuracy and precision of pharmacokinetic parameters. The effects of these factors were not

investigated in this work. However, the techniques presented here are anticipated to ease the

necessary protocol compromises by enabling optimization of the VIF measurement without

affecting the encoding of the tissue.

2.5 Uncertainty resulting from the VIF measurement

As one of the main components of the kinetic model, it should not be surprising that the

accuracy and precision of the VIF has a strong impact on the accuracy and precision of the

measured pharmacokinetic parameters, and these effects have been studied by several

investigators. The prominence of this measurement in the DCE-MRI literature, as opposed to

that in tissue or the common issues of quantifying contrast agent concentrations in MR, is due

to the fact that the measurement of the VIF presents unique artifacts beyond those associated

with the conversion of signal into concentration. Errors in the VIF will have substantial effects

on the accuracy and reproducibility of all pharmacokinetic parameters (11) and the VIF has

been identified as a major source of error in these parameters (57). Improved measurement of

the VIF is an important goal for improvements in the reliability of DCE-MRI. Because of the

limitations imposed by partial volume effects, blood flow, and sampling

requirements, many groups have proposed strategies for improved measurement of the VIF

(58-63), and improved VIF measurement has been identified as an important need by the

Pharmacodynamic/Pharmacokinetic Technologies Advisory Committee for the UK (8,64). Key

contributors to the uncertainty in VIF measurement are partial volume effects due to the small

size of blood vessels, inflow enhancement due to blood flow, and inadequate temporal

resolution of VIF sampling. As will be discussed in the next few paragraphs, these effects are

estimated to produce errors and uncertainties in pharmacokinetic parameter measurements in

excess of 30%.

Partial volume and flow effects tend to scale the entire VIF (65), as a first order effect,

although distortion of the VIF due to partial volume effects has also been reported when the

amount of tissue in the voxel is above 30-40% (66). Uncertainty in the peak concentration

manifests directly as uncertainty in both K^{Trans} and v_b, and therefore variance of the

concentration amplitude appears directly as variance in both parameters (65), implying that

these artifacts tend to introduce unpredictable scaling into the measurement of pharmacokinetic

parameters. It has also been estimated that uncertainties in the measurement of kinetic

parameters of over 20% have been attributed to uncertainties in the measurement of the

VIF (67).

Another commonly studied source of error in the VIF is insufficient temporal sampling

of the VIF. For example, Karmonik and Jackson (68) found that sampling at least once every 4

seconds in humans is associated with variations in excess of 10% into the measurement of

K^{Trans} and over 30% in v_b; these figures would likely be higher for the faster kinetics of small

animal models. Using parameter estimates typical of human breast cancer, Henderson et al.

recommended that the VIF be sampled at least once per second in order to reduce the 95%

confidence interval of kinetic parameter measurements to within 10% of the true

value for all three parameters in the extended Toft's model (56), and this is a widely accepted

guideline (55). Notably, the needs for sampling of the uptake in tissue are considerably

different than in blood: much more modest temporal resolution and higher spatial resolution are

preferred, and this has resulted in suggestions that acquisition schemes be capable of separate

behaviors for blood and tissue; this is achieved with the techniques proposed in this work.

Faster VIF sampling may be required in mice than in humans due to the smaller blood volumes

and faster heart rates, exacerbating this challenge (10,69), although no specific criteria has been

established.

Additional artifacts arise from considering the use of Cartesian phase encoding in MR.

The use of conventional phase encoding when measuring the VIF may also lead to substantial

artifacts in the measurement of pharmacokinetic parameters, because the bolus of contrast

agent may arrive at any time during the acquisition of k-space. This can lead to distortion of

VIF solely due to the arrival of the contrast agent arriving while sampling the edge of k-space.

Roberts, *et al*., found that this introduces uncertainties in the measurement of K^{Trans} of

approximately 10% and in excess of 50% in v_p (70). This is consistent with the recent work by

Cheng (65), which reported that the errors in pharmacokinetic parameter measurements

associated with incorrect sampling of the initial passage were at least 10%.

2.6 Previous approaches to measuring the VIF

Due to the peculiar challenges of VIF measurement in mice, many approaches have

been put forth in an attempt to solve what has been described as a "notoriously difficult

problem" (71). Early approaches to VIF measurement included blood draws (72); these are

unsuitable for small animal imaging due to insufficient mouse blood volume (71). Both

population average VIFs (72) and assumed functional forms (73) have also been used, although

these methods are discouraged because they may not appropriately describe the kinetics within each individual (55,74) and have been found to provide less reproducible results than individual measurements (75). However, it has been argued that population averaging may be appropriate in some cases with highly distal tumors, where dispersion of the VIF reduces individual variations (76). It seems unlikely that dispersion comparable to that encountered along the entire length of a human leg would be encountered in most murine applications, and because of the anatomic specificity, this is not a general solution to the problem of VIF measurement.

One of the most common and natural methods for subject-specific measurement of the VIF is to measure in a blood vessel local to the tissue of interest, however, this approach is not without the limitations of flow and partial volume effects which can also substantially affect quantification (77). In addition, identification of blood vessels in which to perform the measurement is problematic. Manual identification is both tedious and subjective; while automatic techniques (78) may address this issue, they are still unable to address fundamental artifacts, such as partial volume and inflow effects, within the data.

In rats, a highly invasive technique has been used which provides accurate measurement of the VIF (79), that involved inserting a shunt off of the carotid artery and running the shunt through an RF coil. This presented none of the difficulties associated with blood vessel identification or partial volume effects, but was obviously highly invasive. There have been no reports of the use of this technique in mice, and to do so in a large study would be costly, and to use it in a longitudinal study would raise issues of the long term effects of the shunt on the subject.

Recently, some groups have proposed using a reference tissue method, which infers a VIF from the contrast agent dynamics in normal tissue (59,63,71,80,81). This is not

susceptible to the limitations of measurements in local blood vessels, but it requires assuming a pharmacokinetic parameter value for healthy tissue, such as muscle, and any variations of the tissue will be transferred to measurements in tumor. In addition, this technique has not been found to provide superior reproducibility as compared to measurement in a local blood vessel (63).

A direct approach to measurement of the VIF was used by Pickup, *et al.*(10) They acquired very low-resolution images (24 phase encode lines) of the heart during contrast agent injection, achieving a temporal resolution as low as 2 s but with only coverage of a single slice. This allows the measurement of the VIF in a structure that is sufficiently large to avoid in-plane and through-plane partial volume effects, as well as improved noise performance resulting from the large size of the heart. Images were prospectively gated using an ECG signal. This technique has been used to measure the pharmacokinetics of tumors (10,69), but it requires the tumor to be in the same plane as the heart, compromising both tumor coverage and spatial resolution of the tumor kinetics.

Similarly, McIntyre, *et al.* (60), used a dedicated transceiver coil around the tail to perform measurement of the VIF in the tail veins in rat models. A saturation-recovery protocol was used to provide suppression of inflow enhancement; they were able to acquire three slices of tumor tissue in the delay between saturation and imaging of the tail. Imaging in the tail allowed high resolution through the use of a small field-of-view (FOV), and the saturation-recovery approach provided flow suppression. However, the temporal resolution and coverage of the tumor were both limited by the timing restrictions imposed by the saturation preparation pulse: only three slices of tumor could be imaged, and temporal resolution for both the VIF and tissue was only 6.7 s.

A technique to rapidly sample signal from blood vessels was proposed by Taylor, *et al.* (82). That work used a radial projection acquisition to measure the VIF in major blood vessels from individual projections. This allowed measurement of the VIF each repetition period, however, the partial volume correction was crude and approximate. Flow suppression was performed using a saturation slab adjacent to the slice of interest, although at a cost of extending the minimum TR of the sequence by over 20 ms. This reduced the rate of tissue sampling from once every 9 s to once every 12 s, although the VIF sampling rate remained faster than once every 80 ms.

No MR technique yet proposed has been able to provide high temporal resolution measurements of the VIF in mice that are simultaneously insensitive to inflow enhancement and partial volume artifacts. The objective of this work is to develop and test a novel approach for VIF measurement in mice while satisfying these criteria. It is demonstrated that flow suppression can be accomplished by applying spatial presaturation during excitation, which does not require additional RF pulses, gradients, or delays, providing considerably faster flow enhancement than is otherwise possible. Measurement in the left ventricle allows for minimization of partial volume effects. Also, a constrained reconstruction technique that allows measurement from an extremely reduced number of views is used to provide high temporal resolution VIF sampling. Finally, these developments are applied to VIF measurement in mice in an *in vivo* study of reproducibility.

3 Specific Aim 1 – A composite RF pulse for flow enhancement suppression

3.1 Introduction

As previously mentioned in §2.5 , inflow enhancement reduces the sensitivity of the MR signal to contrast-related T_1 alterations due to the spurious hyperintensity caused by fresh spins entering the imaging plane. The partial replacement of saturated with fully relaxed spins substantially reduces the signal sensitivity to T_1 changes due to the addition of contrast agent. The only effective counter to this artifact is to prepare spins with a non-trivial history of RF pulses before they enter the area of interest.

Flow enhancement suppression is commonly accomplished using a 90° preparatory pulse to saturate a wide region around the slice; this fully saturates the incoming magnetization and avoids flow enhancement by suppressing the signal entirely. This prevents vascular hyperintensity in images, but for quantification of vascular signals requires a delay to obtain a useful signal level from blood, which compromises sequence timing. The requirement for additional delays has compromised several approaches for VIF measurement employing flow suppression. One such acquisition strategy acquires only a single slice containing both the vascular structure of interest and the tumor (10). In an alternative approach, three tumor slices may be acquired during the delay between saturation and excitation, as was done by McIntyre, *et al*. (60). Both approaches ultimately restrict tumor coverage, and the use of discrete RF pulses for preparation and measurement, along with their associated gradients, does not make optimal use of time during the pulse sequence.

Alternatively, presaturation can also be performed at a lower flip angle, which requires multiple repetition periods to bring flowing blood into steady state, but which does not necessitate the use of a delay. While a 90° pulse brings spins into steady state after a single pulse (83), lower flip angles require multiple pulses (30). Because spins must experience more pulses, this extends the width of the saturation region that spins must pass through in order to reach steady state. However, in this work it is demonstrated that presaturation may be made a very efficient part of the pulse sequence by combining the saturation and excitation components into a single pulse and exploiting the slice select gradient for signal spoiling.

3.2 Theory

3.2.1 Desired slice profile

The efficiency of presaturation may be improved by combining separate excitation and presaturation pulses into a single composite pulse. The slice-select gradient may be used to spoil the signal excited in the presaturation region. This may be represented as a single slice profile that describes the magnetization produced during both the excitation and saturation phases of the pulse sequence. The regions excited for presaturation, where signal is both excited and spoiled, may be represented as a section of the slice profile with uniform magnitude and linear phase dependence. The resulting phase incoherence causes no net signal to be produced in this region. The excitatory component corresponds to a segment with uniform magnitude and a constant phase.

Because relatively shallow flip angles are used, the RF pulse has a Fourier relationship to the desired slice profile (84). One possible slice profile, specified relative to the Larmour frequency, (Figure 3-1a) is:

$$s(\omega) = \begin{cases} 0 & \omega < -\dfrac{\omega_1}{2} - \omega_2 \\[2ex] e^{-2\pi i \frac{\alpha}{\omega_1}\left(\omega + \frac{\omega_1}{2}\right)} & -\dfrac{\omega_1}{2} - \omega_2 \le \omega < -\dfrac{\omega_1}{2} \\[2ex] 1 & |\omega| \le \dfrac{\omega_1}{2} \\[2ex] e^{2\pi i \frac{\alpha}{\omega_1}\left(\omega - \frac{\omega_1}{2}\right)} & \dfrac{\omega_1}{2} < \omega \le \dfrac{\omega_1}{2} + \omega_2 \\[2ex] 0 & \omega > \dfrac{\omega_1}{2} + \omega_2 \end{cases}$$ (Eq. 3.1)

where ω_1 is the bandwidth of the coherent region of the slice, and ω_2 is the additional bandwidth that is excited, but spoiled for flow enhancement suppression. The rate of phase change over distance is given by $2\pi\alpha/\omega_1$.

An alternative profile choice is to keep the direction of the phase gradient the same in both saturation regions (Figure 3-1b):

$$s(\omega) = \begin{cases} 0 & \omega < -\dfrac{\omega_1}{2} - \omega_2 \\[2ex] e^{-2\pi i \frac{\alpha}{\omega_1}\left(\omega + \frac{\omega_1}{2}\right)} & -\dfrac{\omega_1}{2} - \omega_2 \le \omega < -\dfrac{\omega_1}{2} \\[2ex] 1 & |\omega| \le \dfrac{\omega_1}{2} \\[2ex] e^{-2\pi i \frac{\alpha}{\omega_1}\left(\omega - \frac{\omega_1}{2}\right)} & \dfrac{\omega_1}{2} < \omega \le \dfrac{\omega_1}{2} + \omega_2 \\[2ex] 0 & \omega > \dfrac{\omega_1}{2} + \omega_2 \end{cases}$$ (Eq. 3.2)

This profile is, in theory, equivalent to the first from a flow saturation perspective, however it results in a different RF waveform, with some advantages and disadvantages.
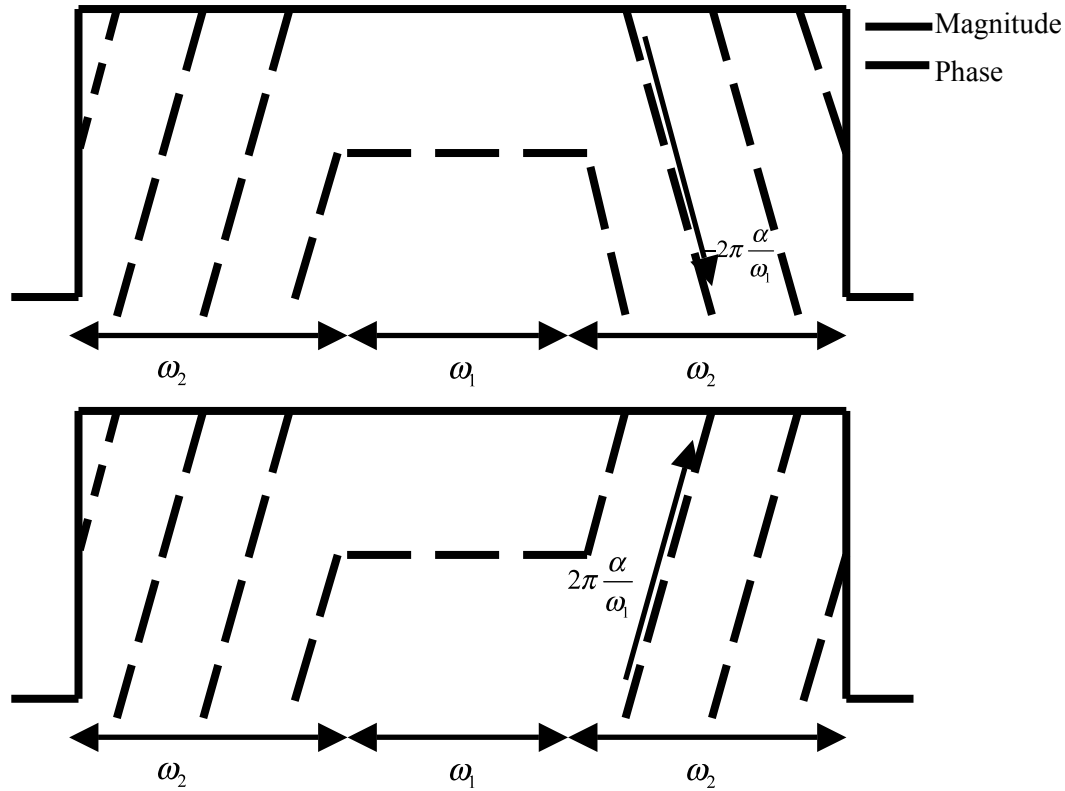
Figure 3-1 The two basic forms of the flow suppressive slice profile.

The profile generated by the symmetric pulse (Eq. 3.1) is shown in (a), while the

antisymmetric pulse (Eq. 3.2) generates (b). The only difference between the two profiles,

in principle, is the sign of the phase gradient in the spoiled region on one side.

3.2.2 RF waveform

Because the flip angles used in DCE-MRI are relatively small, the slice profile is related

by the Fourier transform to the desired RF waveform. For the first slice profile (Eq. 3.1, shown

in Figure 3-1a), the corresponding RF pulse is (85):

$$s(t) = \omega_1 \text{sinc}(\omega_1 t) + \omega_2 e^{it\left(\frac{\omega_1}{4} + \frac{\omega_2}{2}\right)} \text{sinc}\left(\omega_2 \left[t - \frac{2\alpha}{\omega_1}\right]\right) + \omega_2 e^{-it\left(\frac{\omega_1}{4} + \frac{\omega_2}{2}\right)} \text{sinc}\left(\omega_2 \left[t + \frac{2\alpha}{\omega_1}\right]\right) \quad \text{(Eq. 3.3)}$$

The reversal of the phase gradient in the slice profile comes from the symmetry of the two

components that are time-shifted before and after the first term of the equation: one component

is under-refocused by the rephasing gradient, the other is over-refocused. The pulse

which generates the asymmetric slice profile (Eq. 3.2, shown in Figure 3-1b) is:

$$s(t) = \omega_1 \text{sinc}(\omega_1 t) + 2\omega_2 \cos\left(\frac{\omega_1 + 2\omega_2}{4} t\right) \text{sinc}\left(\omega_2\left[t - \frac{2\alpha}{\omega_1}\right]\right)$$ (Eq 3.4)

We refer to the first pulse as a symmetric pulse because of the shape of its envelope; the second

pulse shape will be called an asymmetric pulse. Example asymmetric pulses are shown in

Figure 3-2 and symmetric pulses are shown in Figure 3-3.

The composite flow suppression pulse consists of two or three separate sinc pulses, each

exciting different regions of the slice.   Increasing the phase gradient in the sidebands

corresponds to increasing the shift between the centers of the pulses, which results in those

excited components being more over- or under- refocused by the slice rephase gradient. The

maximum phase gradient is limited by the duration of the RF pulse. Compared to the

symmetric pulse, the asymmetric pulse requires greater peak RF power and a higher RF slew

rate. However, because the high-power region of the RF pulse is more compact, with

appropriate hardware it would be possible to truncate the pulse more aggressively and shorten

the excitation time. This possibility was not explored in this work because very short duration

versions of the asymmetric pulse required more power than was achievable on the system

hardware.

The use of a sinusoidally modulated sinc pulse to achieve spatial suppression was

previously proposed by Doddrell, et al. (86) We have taken the further step of reducing the

time for the pulse by incorporating the spatial suppression and excitation components into a

single composite pulse, which further reduces the time required by the pulse.

When using a sinc pulse for excitation, one of the fundamental design decisions is the

number of zero-crossings of the truncated waveform. In this pulse, the number of zero-

crossings of the component producing the coherent region provides the equivalent tradeoff

between pulse duration and slice thickness; this decision restricts the timeshift of two component pulses, limiting the maximum value of α. The saturation region width becomes primarily limited by the peak RF power needed and the acceptable duration of the pulse, which increases with the width of the saturation regions. The relative amplitudes and durations of all pulse components are fixed in the raw pulse waveform because they are identically scaled during excitation to achieve the desired flip angle. For this reason, it is convenient to refer to a pulse by the ratio of the widths of the two regions, rather than an absolute width. We chose a sinc pulse with three zero crossings on each side of the central lobe for consistency with the equivalent 2D excitation pulse.

Although only integer values for α and ω_2/ω_1 are used in this study, this is not a necessity. Because we investigate the effects of the saturation width in this work, the use of an integer value for α allows for a natural increment of the saturation width in units of the coherent slice thickness. The use of an integer for both parameters simplifies pulse construction because it forces all three components of the pulse to have several zero-crossings in common, allowing for simple construction of the pulse with a finite slew rate at the beginning and end of the pulse.
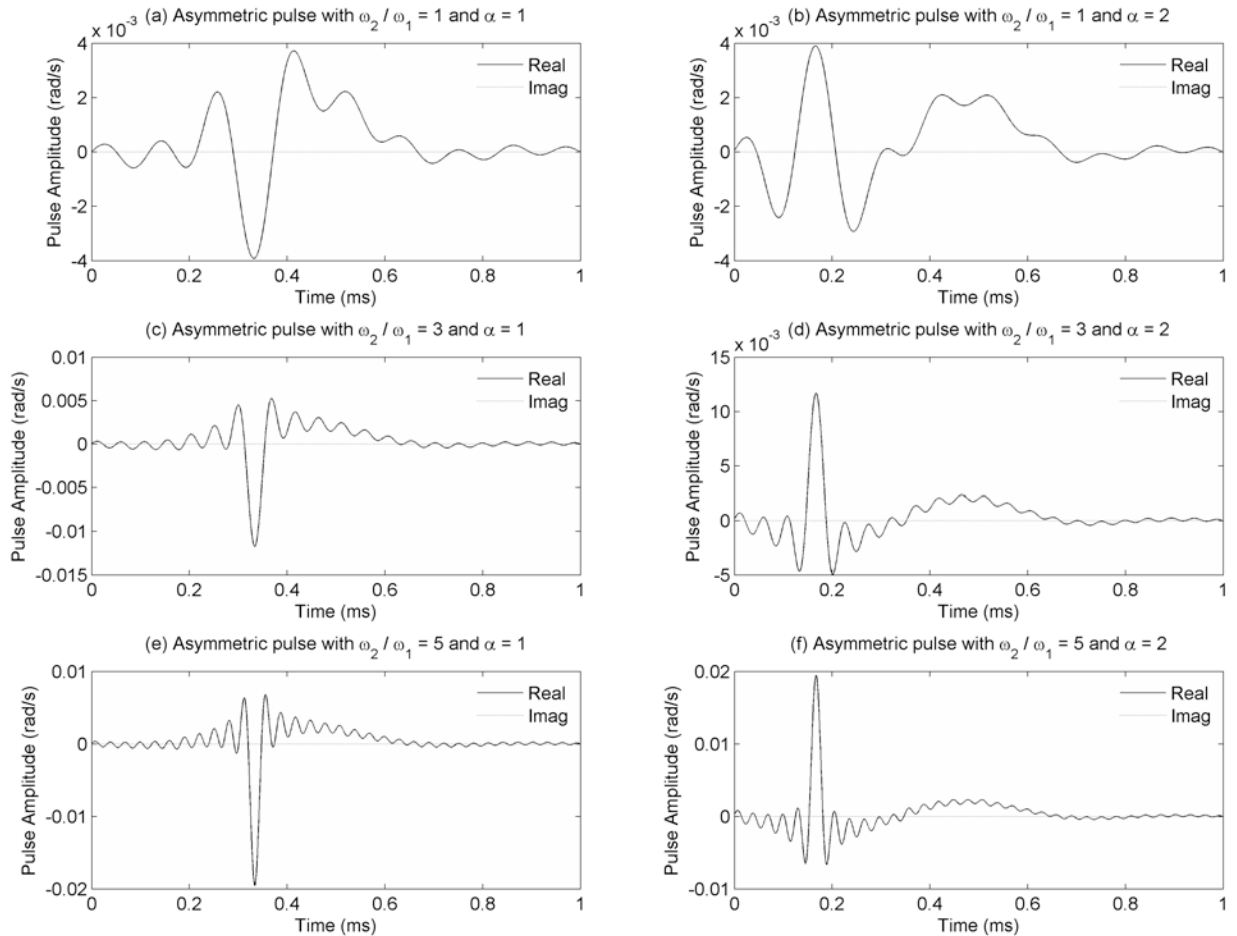
Figure 3-2 Asymmetric pulses used in the simulations and measurements.

The pulses from the asymmetric family that were used are shown; units are specified as

γB_1. Increasing the width of the sideband (a to c to e and b to d to f) both makes the

spoiling pulse more narrow and increases its amplitude. Increasing the separation of the

spoiling lobe and the main lobe (a to b, c to d, and e to f) corresponds to a larger phase

gradient in the resulting slice profile.
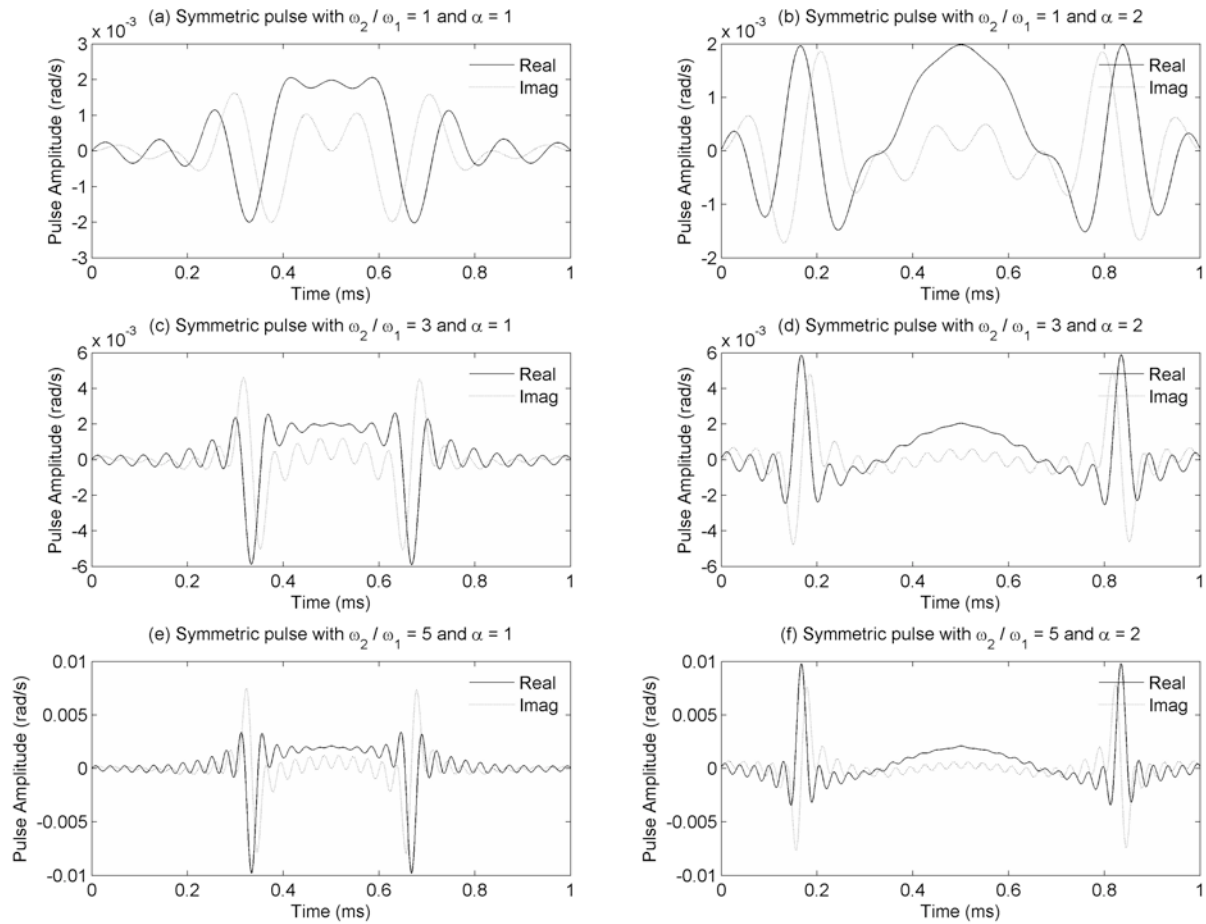
Figure 3-3 Symmetric pulses used in the simulations and measurements.

The relationships between the sideband width and the degree of spoiling to the RF pulse that were mentioned regarding the asymmetric pulse apply here. The prominent imaginary components of the suppression lobes occur because the two pulses are centered on a different frequency than the zero of the rotating reference frame; in the asymmetric case the imaginary components of the two sub-pulses cancel. The peak amplitude of these pulses is half that of the corresponding asymmetric pulse, as given in the Eq 3.3 and 3.4.

3.3 Calculated slice profiles

3.3.1 Methods

To validate the theoretical slice profile calculation and to evaluate the artifacts resulting

from the truncation of the pulses, numerical simulations were performed of the composite RF

pulses by numerically solving the Bloch equation using Matlab (Mathworks, Natick, MA).

Simulations were performed by assuming a linear slice-encoding gradient for the duration of

the RF pulse, which was amplitude-reversed for 50% of the pulse duration immediately

afterwards. Stationary spins were simulated at 1024 evenly-spaced points along the gradient

providing to peak frequency offsets from -42 kHz to +42 kHz when the gradient was present.

The RF pulses simulated had ω_2/ω_1 of 1 through 5 and $\alpha = 1$ and 2; both symmetric and

asymmetric pulses were used. The flip angle was 30°; the RF pulse amplitude was calibrated to

the appropriate area under the slice profile according to a Fourier relationship. Relaxation

effects were neglected due to the short (1 ms) pulse duration. The residual transverse and

longitudinal magnetization after the rephase gradient was plotted, as was the phase of the

transverse magnetization. The flip angle of the slice profile was calculated by taking the

arccosine of the ratio of the signal in the saturation band to the signal outside the excited

region; the standard deviation of the flip angle in the saturation band was calculated to estimate

the ripple in the profile. Example asymmetric pulses used are shown in Figure 3-2 and

symmetric pulses are shown in Figure 3-3.

3.3.2 Results

The calculated slice profiles are flat in each region of the profile, although a slight

artifact at the transition between the regions is observed in all three profiles, resulting from the

truncation of the edges of the saturation pulses. The ripple in the saturation band was

equal for both symmetric and asymmetric pulses; it was $\pm 0.15°$ for pulses with $\alpha = 1$ and $\pm 0.33°$

for pulses with $\alpha = 2$. Greater ripple, as well as an artifact at the transition of the regions, is

found in the profiles with a greater phase gradient. The artifacts do not vary with the width of

the saturation region because they are a Gibbs effect arising from the truncation of the RF

pulse, as opposed to cross-talk between the coherent and incoherent regions. The artifacts are

larger with the greater value of α because the pulse is truncated at a larger amplitude level of

the time-shifted component. A slight bowing of the profile is observed as the saturation width

increases; this is a change of less than $1.5°$ over the width of the profile shown. The profiles for

the asymmetric pulses are shown in Figure 3-4 and the symmetric pulse profiles are in Figure

3-5.
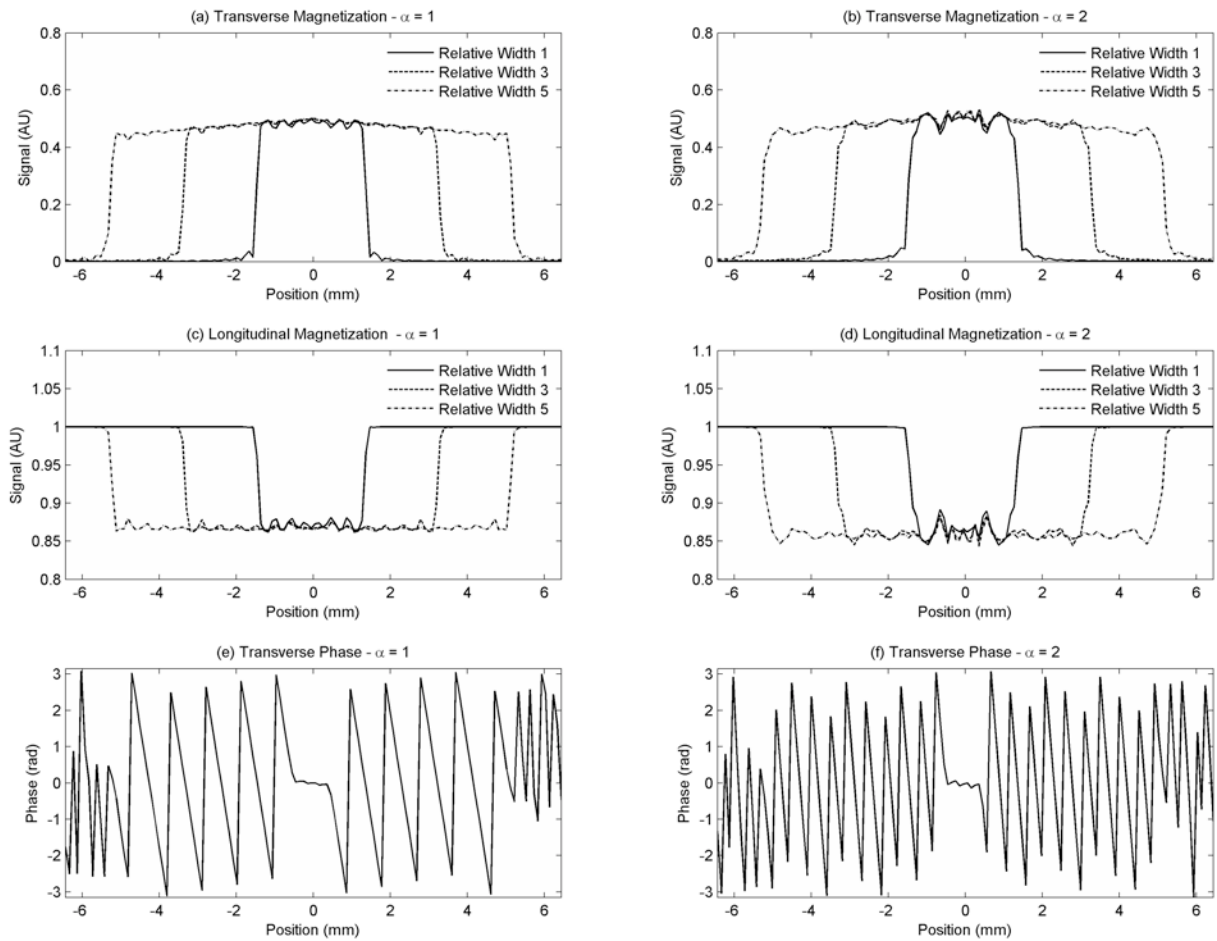
Figure 3-4 Simulated slice profiles with from the asymmetric pulses.

The transverse magnetization of the slice profiles shows a flat response (a), which is matched by the residual longitudinal magnetization (c). The 4π pulse shows some artifacts at the transition between the coherent and the incoherent regions (b,d). The phase profile is identical on both sides of the coherent region (e,f), as both sides are under-refocused by the slice select gradient.
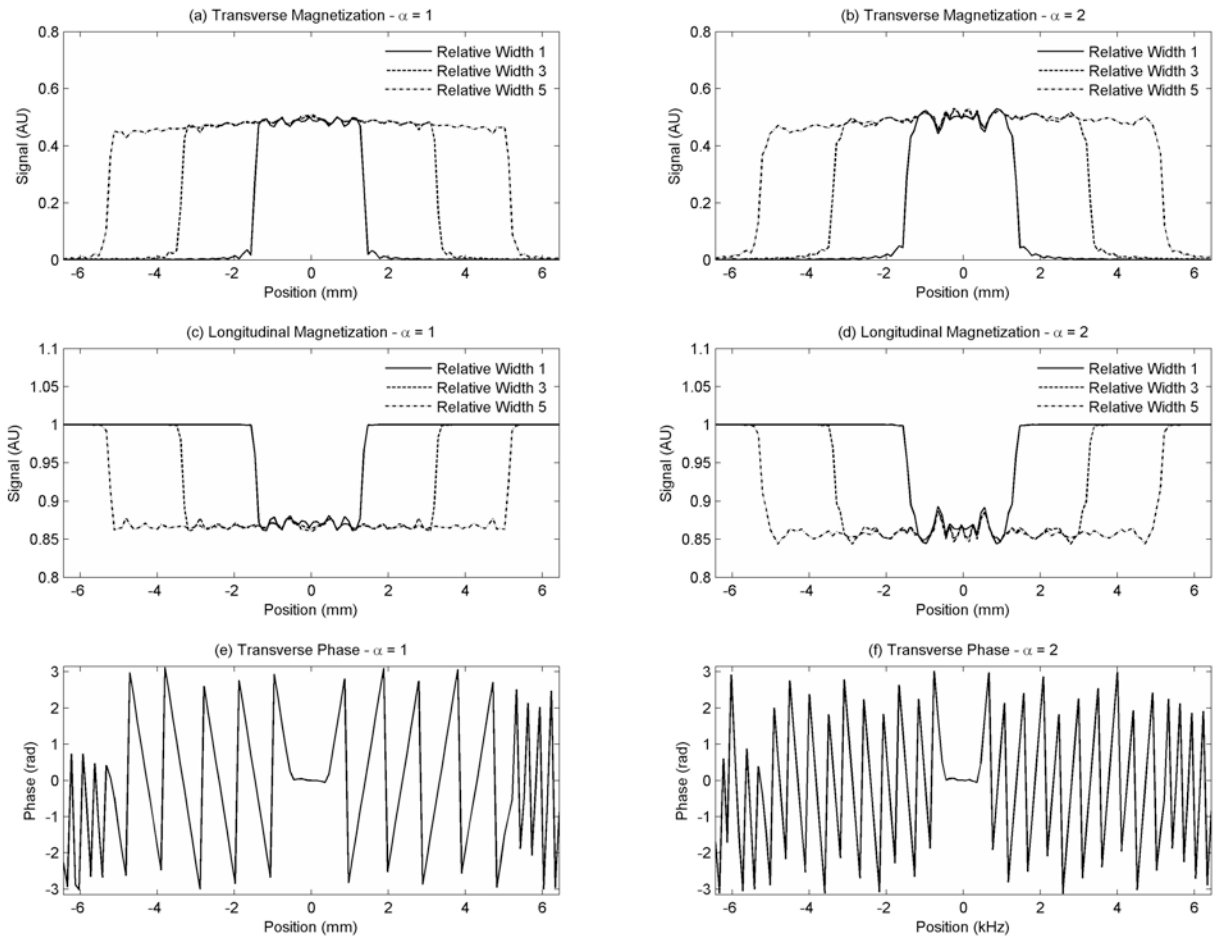
Figure 3-5 Simulated slice profiles from the symmetric pulses.

The magnitude of the slice profiles is comparable to those produced by the asymmetric pulses, although close examination shows that the profiles are slightly less bowed. The phase gradient changes direction on each side of the coherent region, due to one side being over-refocused by the rephasing gradient.

3.4 Calculated signals

3.4.1 Methods

The use of this RF pulse relies upon the assumption that widening the saturation region does not change the net signal produced by the pulse. To test the stability of the signal as the sideband width was increased, theoretical calculations were performed using the previously tabulated slice profiles. To calculate the net signal, the signal at each point along the slice profile was weighted according to the flip angle at that point in space according to the equation for a steady state spoiled gradient echo sequence for four scenarios:

1) Full T_1 relaxation

2) TR of 40, T_1 of 700 ms

3) TR of 40, T_1 of 1800 ms

4) TR of 40, T_1 of 3500 ms

The fixed value of TR was chosen to match the TR used in the institutional small-animal DCE-MRI protocol, which would be used as the basis for the VIF measurements in the final aim. These weighted profiles were integrated to provide the simulated signal that would be measured using a sinc pulse (*i.e.*, $\omega_2 = 0$) and flow suppressive pulses with $\omega_2 / \omega_1 = 1$ to 5 and α = 1 and 2. The simulated parameters are nominal parameters for *in vivo* measurement of blood, blood with 0.2 mM of contrast agent, and water at 4.7 T. The flip angle of the profiles was 30º.

3.4.2 Results

The expected signal produced by the RF pulses, shown in Figure 3-6 demonstrates interesting features of the signal behavior of the slice profiles and shows differences between both the symmetric and the asymmetric pulses, as well as between the different levels of

spoiling. First, a drop in signal is seen for composite pulses. The origin of this

difference is shown in the slice signal profile from the sinc pulse (Figure 3-7). The profile

contains a non-trivial region with flip angles below the nominal flip angle. In a short TR, T_1-

weighted sequence, these components can provide a large fraction of the signal within the slice

(30). Effects become more prominent as T_1 increases. However, in the composite pulse the

transition regions have a large phase gradient and their contribution is substantially reduced,

producing a smaller overall signal.
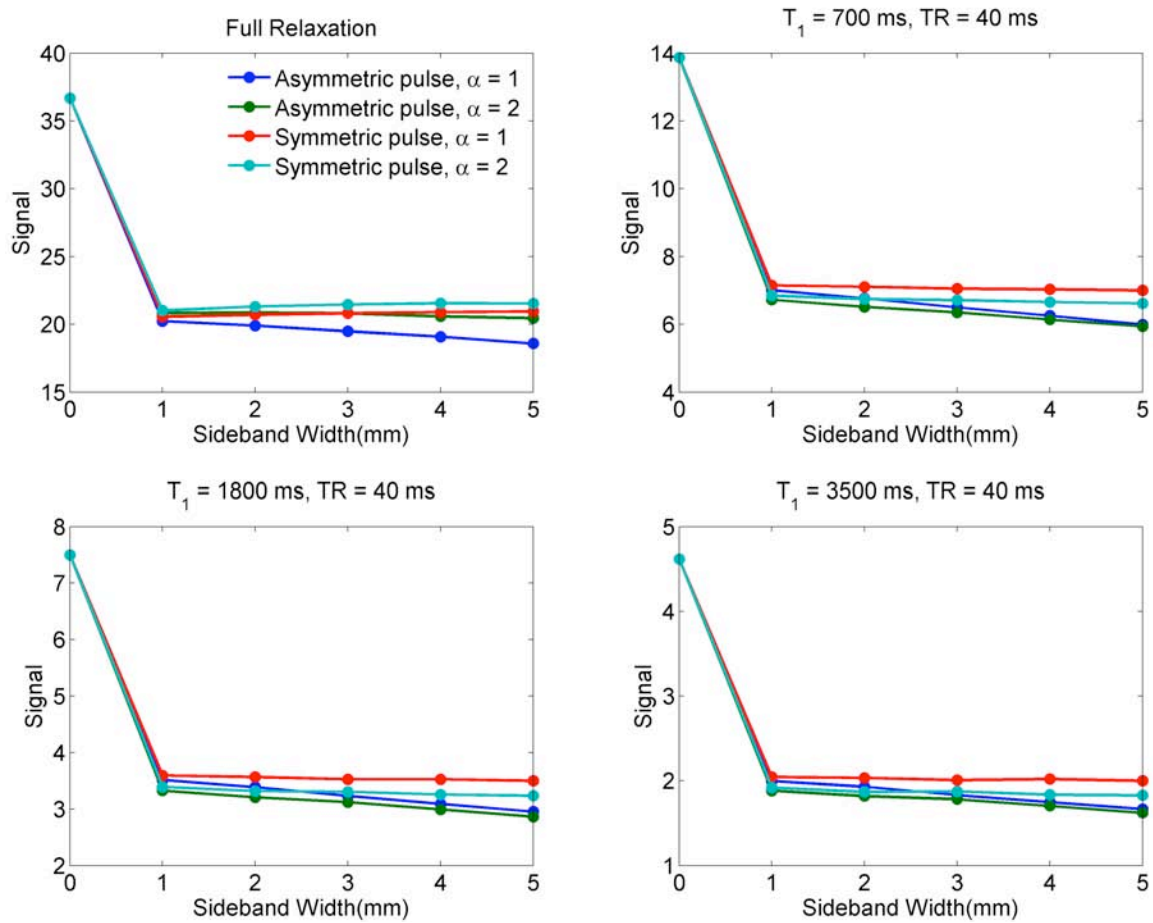
Figure 3-6 Theoretical signal as a function of sideband width.

For all of the pulses, a gradual increase of the signal level is found with increasing

sideband width due to imperfect spoiling of the signal. The profiles produced by the

symmetric pulses are considerably more stable with changes in the sideband

width than those produced by the asymmetric.

When varying the width of the composite pulses, there is an approximately linear drift in the signal with the width of the saturation bands. The signal change over the entire width is given in Table 3-1, calculated as the difference of maximum and minimum of signal values for each pulse, normalized to the signal produced with $\omega_2/\omega_1 = 3$. The symmetric pulses demonstrated greater stability with changes in width than the asymmetric pulses, drifting in signal by much less over the range of widths considered, indicating that they will likely provide better spoiling of out-of-slice signals and that it is more suitable for *in vivo* imaging. These figures assume a homogenous phantom and do not account for differences in spoiling of inhomogeneous structures out of the slice.

	Full Relaxation	Short T_1	Medium T_1	Long T_1
Asymmetric $\alpha = 1$	8%	15%	17%	18%
Asymmetric $\alpha = 2$	2%	12%	15%	15%
Symmetric $\alpha = 1$	2%	2%	3%	2%
Symmetric $\alpha = 2$	2%	3%	4%	4%

Table 3-1 Range of signals generated by the RF pulse over the sideband widths

considered.

Values are the difference in the maximum and minimum signal, normalized to the median

signal
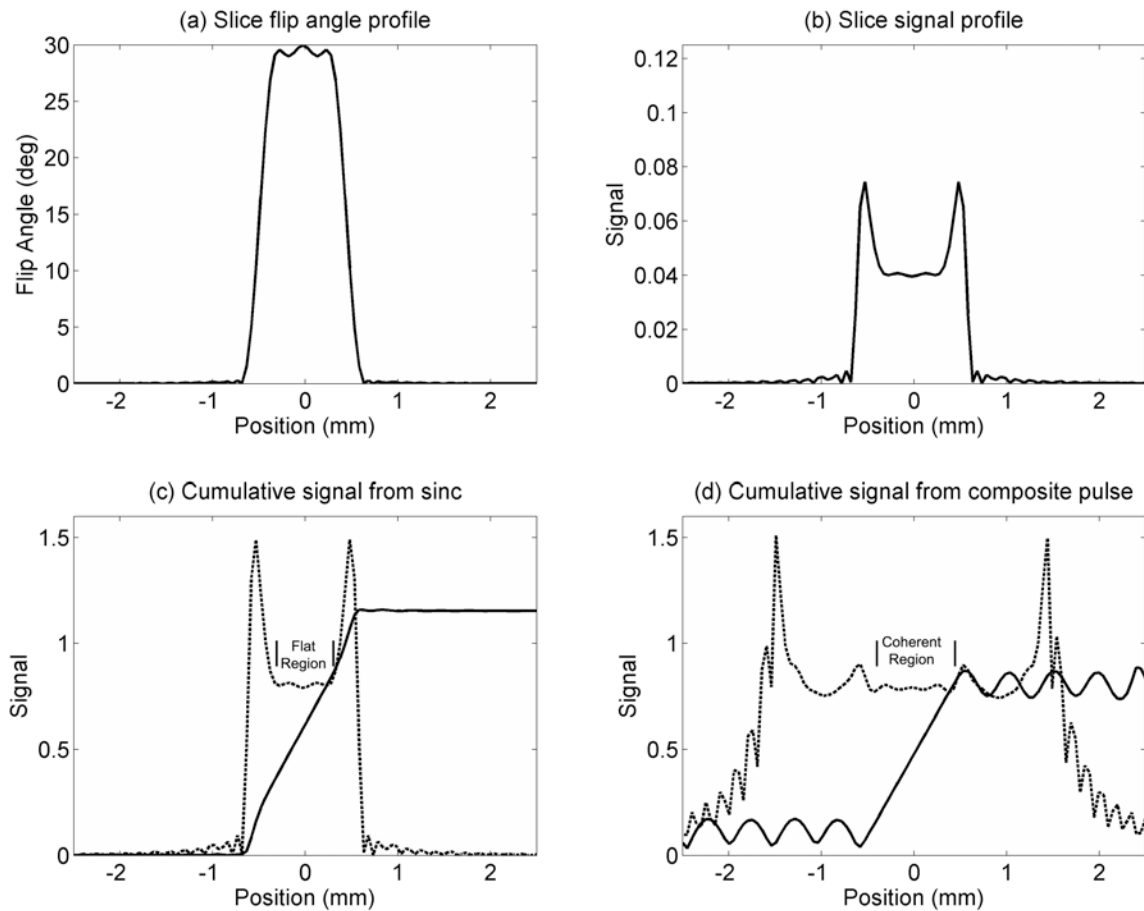
Figure 3-7 Slice profile of a sinc pulse.

(a) shows the flip angle slice profile generated by a sinc pulse, while (b) shows the signal generated by each point along the slice. The horns are due to the low flip angle components of the slice profile. As the specified flip angle is above the Ernst angle for the simulation parameters, the region with greatest signal contribution is outside of the central region of the slice. (c) shows the cumulative integral of the signal produced by the sinc pulse. (d) shows the cumulative signal produced by the pulse width a saturation width of 2 mm and $\alpha = 2$. With the composite pulse, signal from the periphery is spoiled and has a relatively small contribution. For the sinc pulse, the transition region contributes a large fraction of the total signal.

3.5 Measured slice profiles

3.5.1 Methods

All data in this and later sections were acquired on a Biospec 4.7T small animal MR scanner (Bruker Biospin MRI, Billerica, MA) using the Paravision 4.0 operating system. The pulses that had been simulated were implemented on the scanner and slice profiles were measured to confirm the slice profile simulations experimentally. Excitation was performed with the RF pulse being tested, followed by nonselective 90° and 180° pulses, providing a measurement of the residual longitudinal magnetization. Acquisition parameters were: TE = 12.4 ms, TR = 4000 ms, matrix size = 256, FOV = 3 cm, receiver bandwidth = 85 kHz, flip angle = 30°. The pulse duration was 1 ms, yielding bandwidths of 6210 Hz for coherent band, corresponding to a coherent region width of 2.2 mm and sideband widths from 2.2 mm to 11 mm were used. Measurements were performed in a 6 cm long, 4.7 mm inner diameter (ID) water phantom doped with 0.5 mM gadopentetate dimeglumine (nominal T_1 = 400 ms). Measurements were made using S116 gradients and a 72 mm ID birdcage coil (Bruker BioSpin, Billerica, MA) to minimize effects of RF coil inhomogeneity on the acquisition. The ripple in the slice profile was calculated as before.

The transverse magnetization was measured by excitation, followed by a hard 180° refocusing pulse. Only the phase was plotted; the measurement of the amplitude was unreliable because, unlike the simulations, physical measurements are necessarily an integral over a finite spatial region, which would lead to signal dephasing. Acquisition parameters were the same in the longitudinal and transverse magnetization measurements. The same phantom and hardware were used as in the measurement of saturation profiles.

3.5.2 Results

The measured slice profiles demonstrate good reproduction of the RF pulse. Magnitude profiles with sideband-to-center ratios of 1, 3, and 5 are shown in Figure 3-8 and Figure 3-9, while the phases are shown in Figure 3-10 and Figure 3-11. As with the simulations, some artifacts are visible at the transition between the coherent and the incoherent regions of the slice profile, however the shape of the slice profiles matches well with the calculated values. As before, the artifact at the transition is larger for the profile with the greater phase gradient. The standard deviation of the flip angle in the saturation region remained under 1 degree, which includes variations from noise. The mean flip angle produced by the asymmetric pulse with a width of 5 mm and a phase gradient of 2π/mm was 28.1º and 29.0º for the 4π/mm pulse. The symmetric pulse produced slightly more accurate flip angles of 29.0º and 29.6º, respectively. These measurements indicate that the pulse is produced as desired by the scanner and that the desired phase behavior is present.
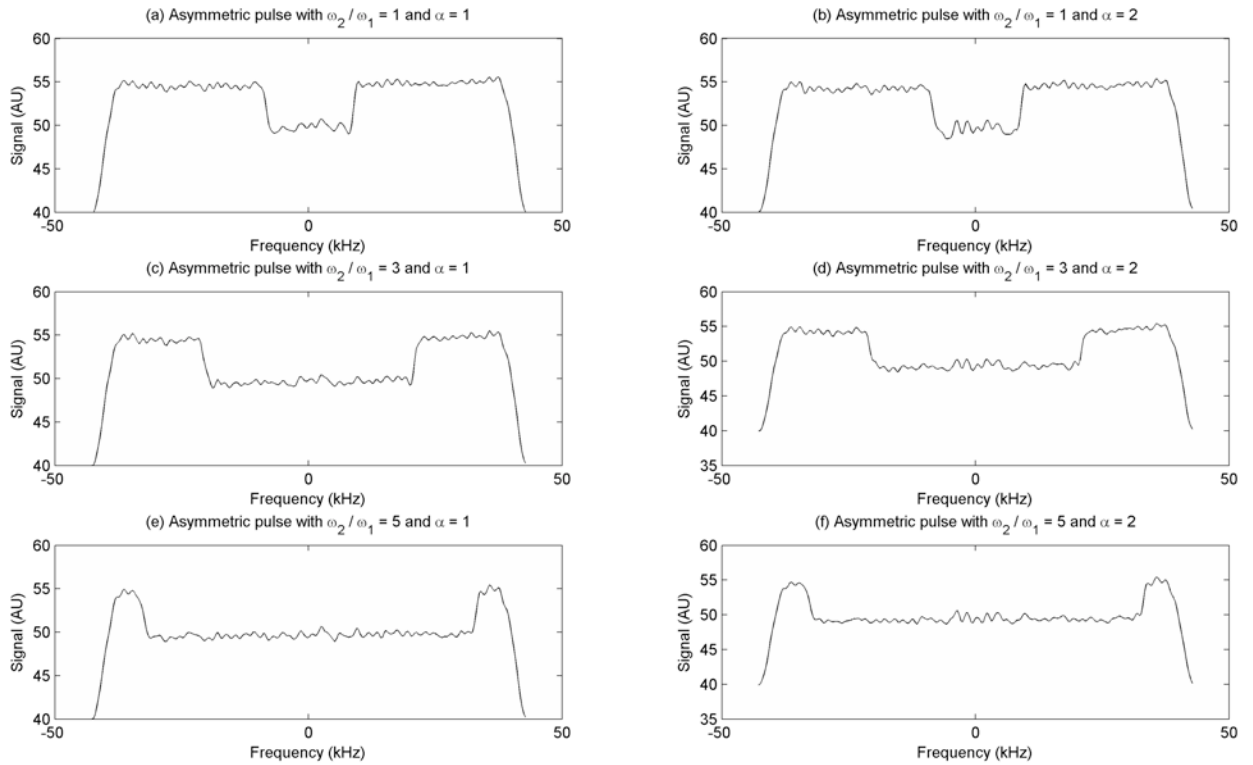
Figure 3-8 Measured saturation profiles from the asymmetric pulses.

The profiles all display flat saturation regions, although the more heavily spoiled profiles

show the same Gibbs artifact which appeared in the simulations.
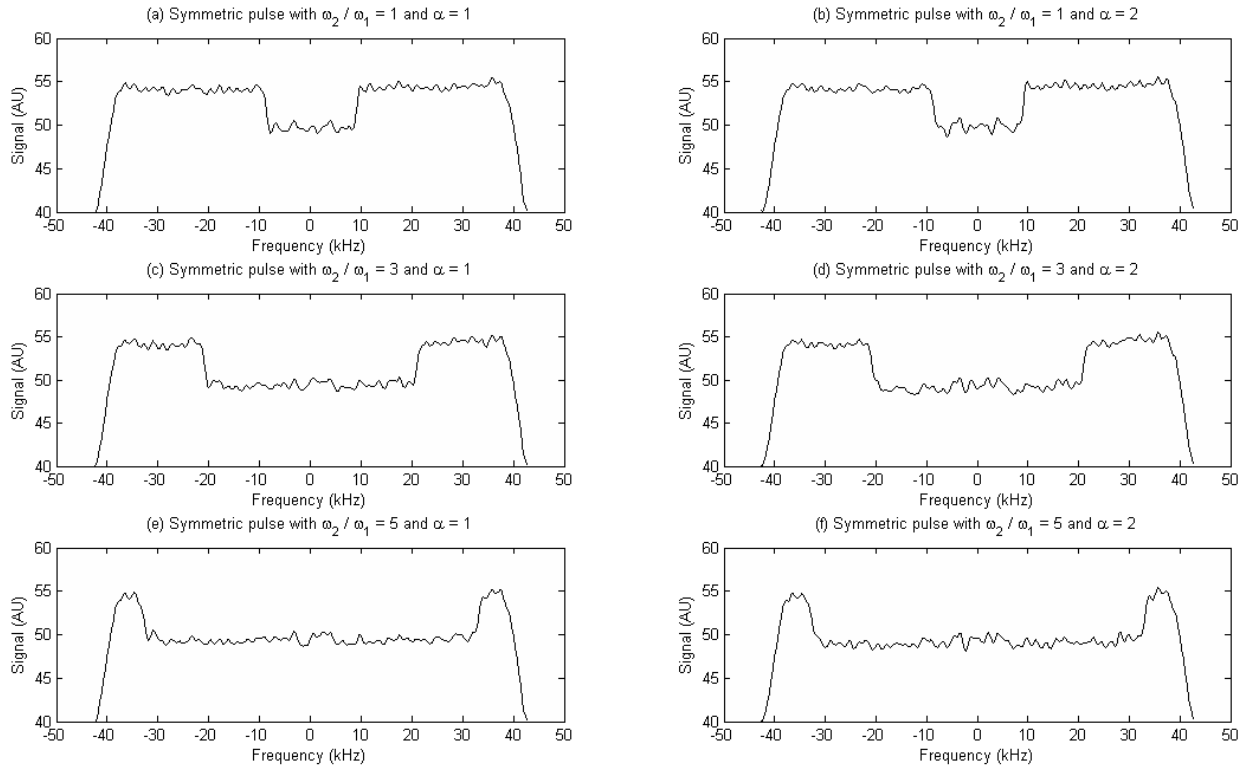
Figure 3-9 Measured saturation profiles from the symmetric pulses.

The profiles produced by the symmetric pulses show similar behavior to those generated by the asymmetric pulses. The width of the saturation region increases as desired, and is the same for pulses with both degrees of spoiling.
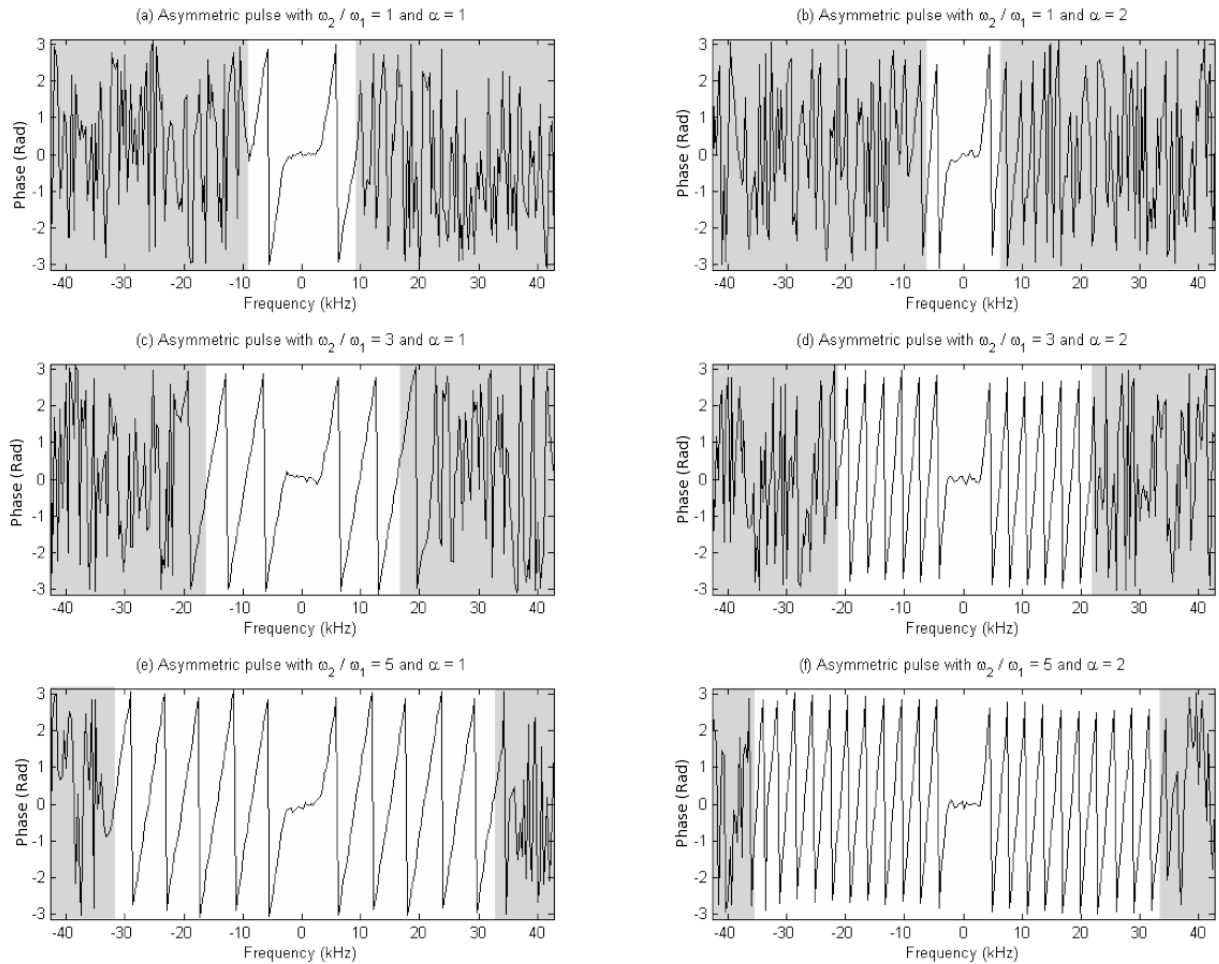
Figure 3-10 Measured transverse profile phases from the asymmetric pulses.

The phase profiles from the asymmetric pulses display the desired combination of coherent and spoiled regions. The linear phase gradient continues past the desired excited width due to the sidelobes of the RF pulses that have a meaningful phase but low amplitude. Slightly more ripple is noticed in the phase profile of the more heavily spoiled profiles, resulting from the greater Gibbs ringing artifact. Shaded regions indicate boundaries of the primary excited regions.
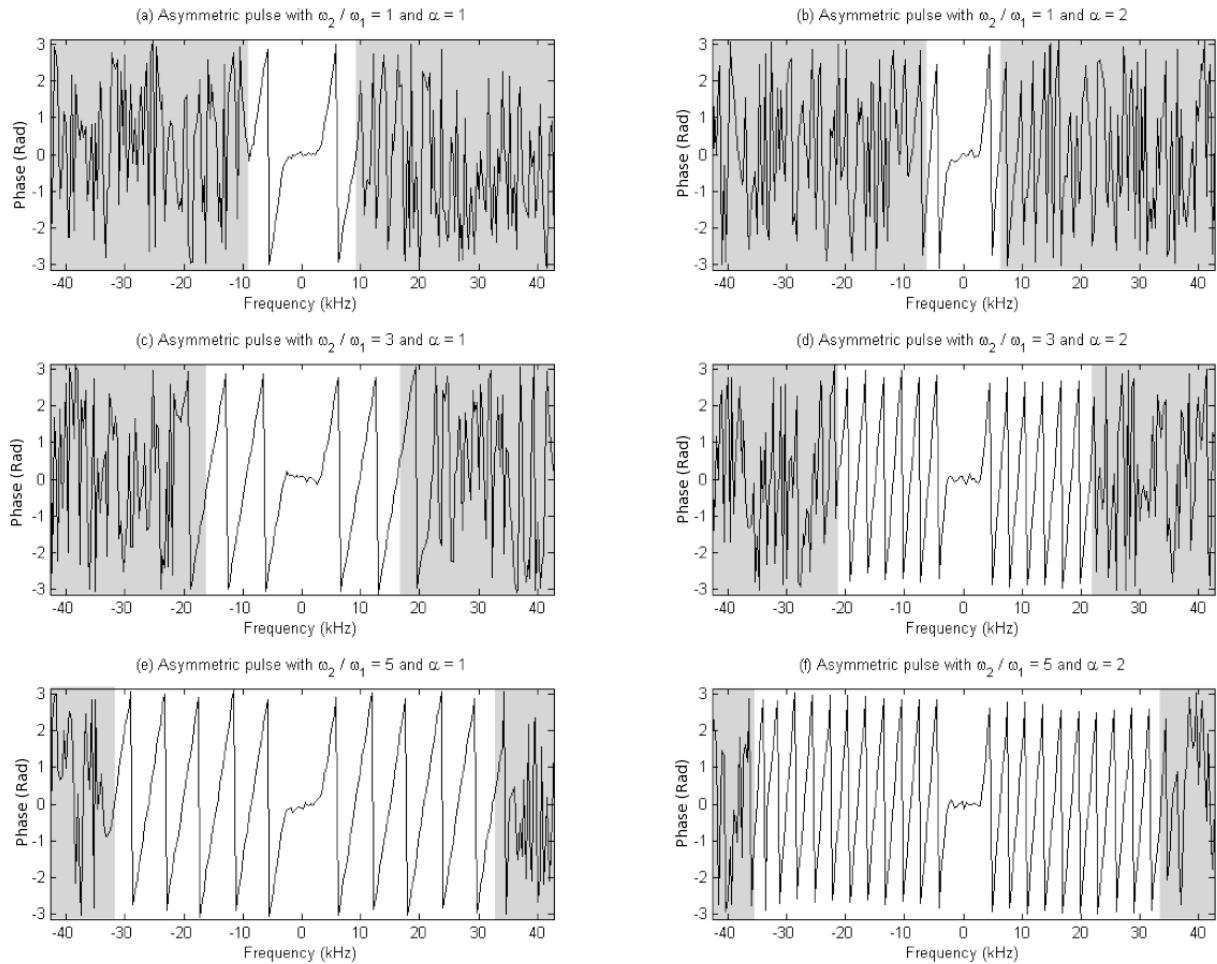
Figure 3-11 Measured transverse profile phases from the symmetric pulses.

As with the asymmetric pulses, the symmetric pulses produce the desired phase behavior.

3.6 Numerical simulations of flow

3.6.1 Methods

Simulations were also performed to investigate the approach of flowing spins to steady state when excited with the proposed RF pulse. A set of discrete spins were used, which moved linearly through the excitation region with time. A train of RF pulses that affected the moving spins was simulated via the Bloch equations, and the signal produced by the spins at each spatial point was calculated over the entire excitation region. The transverse

magnetization after each RF pulse was used to construct the signal profile across the slice. Simulation parameters were: TR = 40 ms, flip angle = 30º, T_1 = 1800 ms, gradient strength = 140 kHz. Flow rates from 1 mm/s to 20 mm/s were tested and a pulse with α = 2 and ω_2/ω_1 = 9 that produced a slice thickness of 1 mm was used.

3.6.2 Results

The numerical simulations of flow produced signal profiles along the slice direction, shown in Figure 3-12. The profiles demonstrate that the magnetization reaches its steady state value before arriving at the coherent portion of the slice for velocities of up to 10 mm/s, with the combination of flip angle and TR that were tested. This velocity is somewhat less than average velocities of 23 cm/s which have been reported in the aortas of mice (87), however, it must be considered that linear velocity in the heart will be slower because the ventricle is larger than the aorta and that the width of the saturation region is amplified by tortuous path blood must travel before entering the ventricle. More rapid flows may prevent spins from reaching steady state before reaching the coherent center, resulting in incomplete suppression. A cumulative signal profile for the same three velocities is shown in Figure 3-13. Simulations indicate that the use of this pulse is able to improve the sensitivity of flow-affected measurements, but testing in realistic applications is warranted.
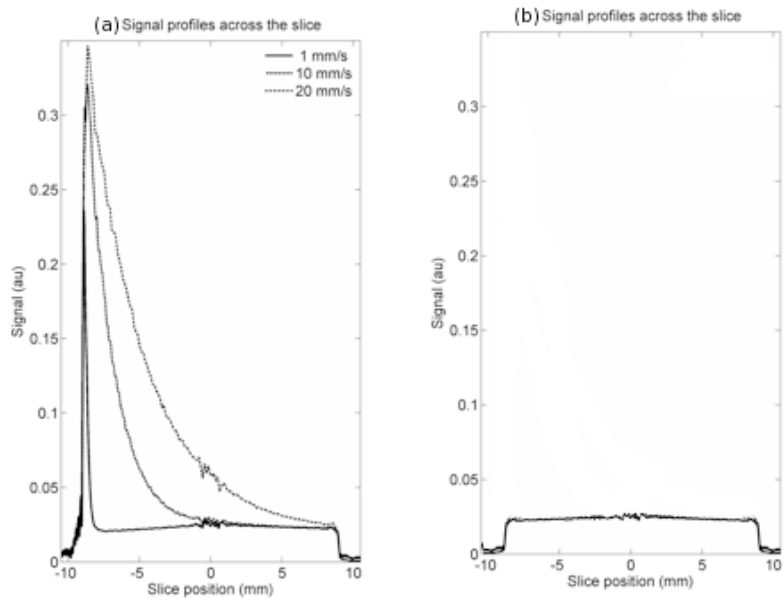
Figure 3-12 Signal profile in the presence of flow.

(a) The signal profile along the slice is shown for a spatial presaturation pulse at several velocities. Flows below 10 mm/s are fully in steady state by the time they reach the center of the slice for this protocol. More rapid flows are not in steady state and will have a reduced sensitivity to contrast related signal changes. (b) The signal profile in the absence of flow is shown.
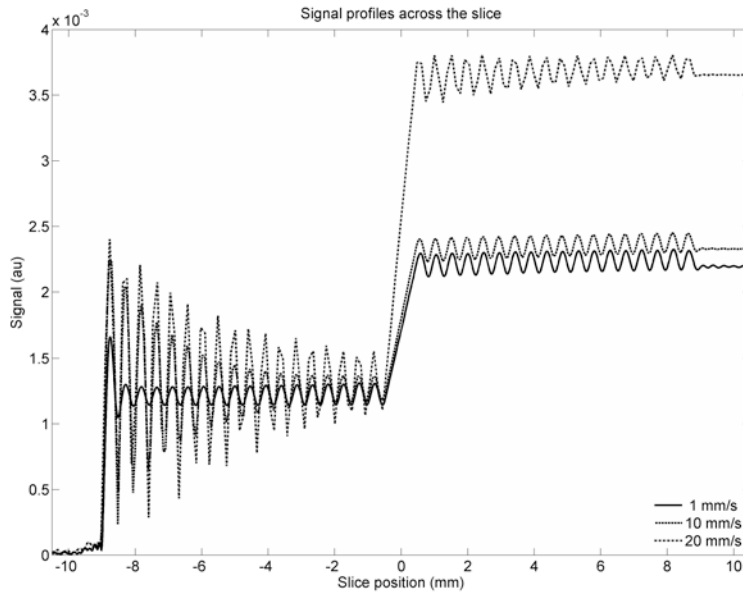
Figure 3-13 Cumulative signal of the profile generated by RF pulse in the presence of flow.

The signal from the flow-related peak, although large in magnitude, is attenuated by the incoherence of the sidebands. The most rapid flow, where spins have not reached steady state prior to entering the coherent portion of the slice, displays considerably flow-related hyperintensity. Some residual signal, constituting up to 30% of the total signal, remains when flow travels in a linear path. A greater degree of signal spoiling would reduce this effect. No amount of increase in the width of the saturation bands will remove this spoiling because it represents the signal requiring a distance to reach steady state which is long compared to the spoiling, but not necessary the saturation width.

3.7 Phantom measurements of flow

3.7.1 Methods

The ability of the RF pulse to suppress enhancement due to linear flow was tested in phantom. A silicone catheter was embedded within a bovine gel phantom (nominal T_1 of gel

was 700 ms, nominal T_1 of the water in the catheter was 3000 ms). Flow was

introduced in the catheter using a power injector (Harvard Apparatus, Boston, MA) at several

rates. Composite RF pulses with α = 1 and 2 and ω_2/ω_1 = 1 to 5 were used for both symmetric

and asymmetric pulses. For RF pulse, spoiled gradient echo images were acquired of the

phantom with flow for 1 minute, followed by 30 seconds without flow. No dummy scans were

acquired, but the initial frame after the injector was started was not included in signal averaging

to account for transitory signal states. Acquisition parameters were: TE = 2.75 ms, TR = 20

ms, flip angle = 25°, matrix size = 256x192, FOV = 4.1 x 3.1cm, receiver bandwidth = 80 kHz,

pulse width = 1 ms, slice thickness = 1 mm. Flow rates ranged from 0.05 mL/min (average

linear velocity of 0.6 mm/s) to 1 mL/min (12 mm/s). The signal for each pulse with and

without flow was measured in an ROI drawn around the interior of the catheter. The flow

related enhancement was calculated as the percent increase in the signal amplitude due to flow.

Additionally, a region of interest was drawn in the gelatin at the center of the phantom and the

mean signal within that ROI calculated for all pulses used. Measurements were made with

BG6 gradients and a 35 mm ID birdcage coil. The choice of the smallest available birdcage

was to maximize the SNR available.

3.7.2 Results

The RF pulse effectively suppressed flow enhancement in phantom. A 5 mm saturation

width reduced the signal of flowing spins to slightly less than that of stationary spins for all but

the flow of 1 mL/min, as illustrated in Figure 3-14, indicating effective flow suppression.

Increasing the phase gradient of the spoiled region from 2π/mm (Figure 3-15ac) to 4π/mm

(Figure 3-15bd) provided slightly greater reduction in flow enhancement for most velocities,

due to better suppression of the signal at the edges of the slice, although exceptions are noted.

The symmetric pulse was comparable to the asymmetric pulse in the effectiveness of reducing

inflow enhancement, although the stability of the signal in the gel and of the baseline signal was considerably better with the symmetric pulse than with the asymmetric pulse. The CV of the signal in the gel (Figure 3-16) with the asymmetric pulses were 41% and 23% for $\alpha = 1$ and $\alpha = 2$, respectively, while the symmetric pulses each had a CV of 4%. The fluctuations in the baseline signal of the tap water were similarly superior with the symmetric pulse: 8% and 7% vs. 18% and 13%. The signal change with sideband width is not the generally linear behavior observed in the simulations, although the stability advantages of the symmetric pulse are still present. Deviations from linear behavior may be the result of imperfections in the phantom, or in the differences between the pulse as idealized and as actually produced. We observe the decrease in signal relative to the sinc pulse of 40%, which is comparable to the signal decreases of 45-55% that were found in simulations.

(b) 2π/mm antisymmetric pulse with sideband widths from 1 to 5 mm

(c) 4π/mm antisymmetric pulse with sideband widths from 1 to 5 mm

(a) sinc

(d) 2π/mm symmetric pulse with sideband widths from 1 to 5 mm

(e) 4π/mm symmetric pulse with sideband widths from 1 to 5 mm
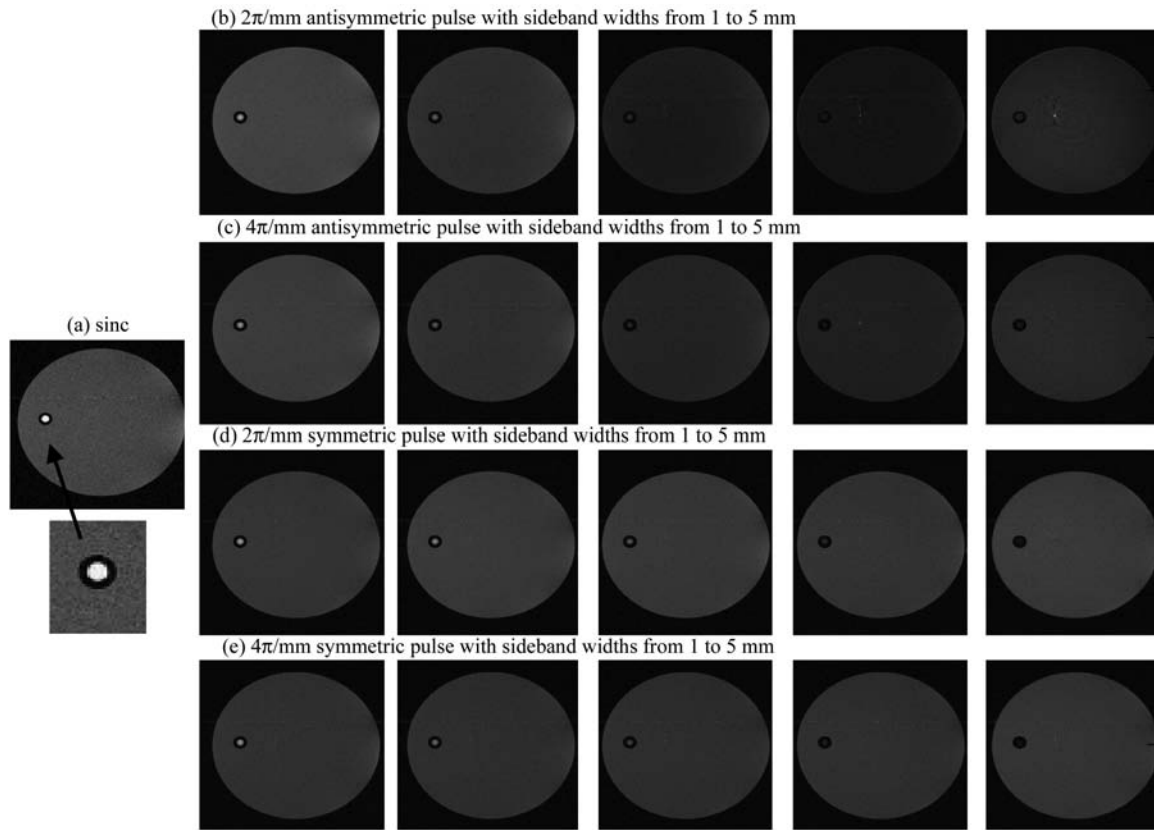
Figure 3-14 Images of the flow phantom acquired during 1 mL/min flow.

The signal of the flowing water inside the catheter fades away as the width of the sideband increases and the signal enhancement artifact is reduced in strength. The inset shows a magnified view of the catheter; signal was measured on the interior of the catheter and contained only water. Instability with sideband width in the signal from the asymmetric pulse is observable in the surrounding gels.
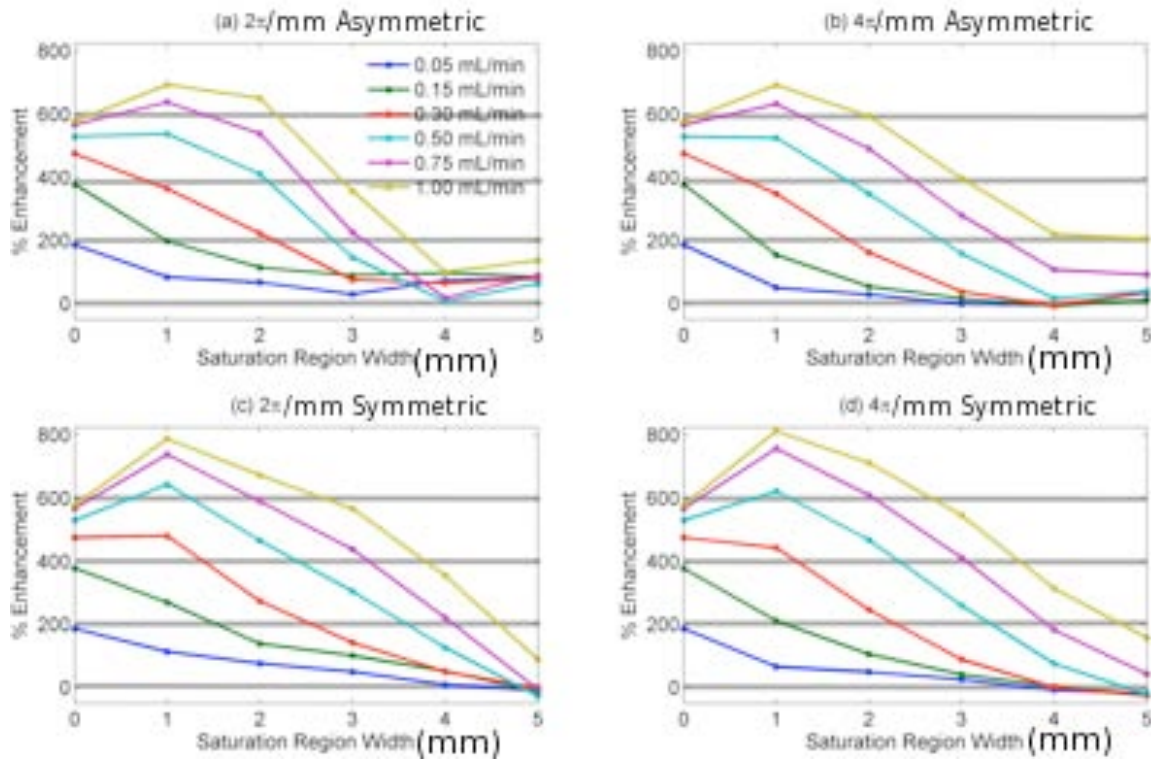
Figure 3-15 Plot of the signals in the catheter during flow.

The percent signal increase in the presence of different rates of flow, relative to the baseline signal, is shown for two different choices of the sideband phase gradient (a vs. b and c vs. d), as well as for asymmetric vs. symmetric profiles (a and b vs. c and d). The composite RF pulse provides effective flow suppression across a wide range of flows. Volumetric flows are specified to avoid inconsistencies associated with non-plug flows. The presence of non-plug flow in measured data makes direct comparison to simulations difficult to perform meaningfully.
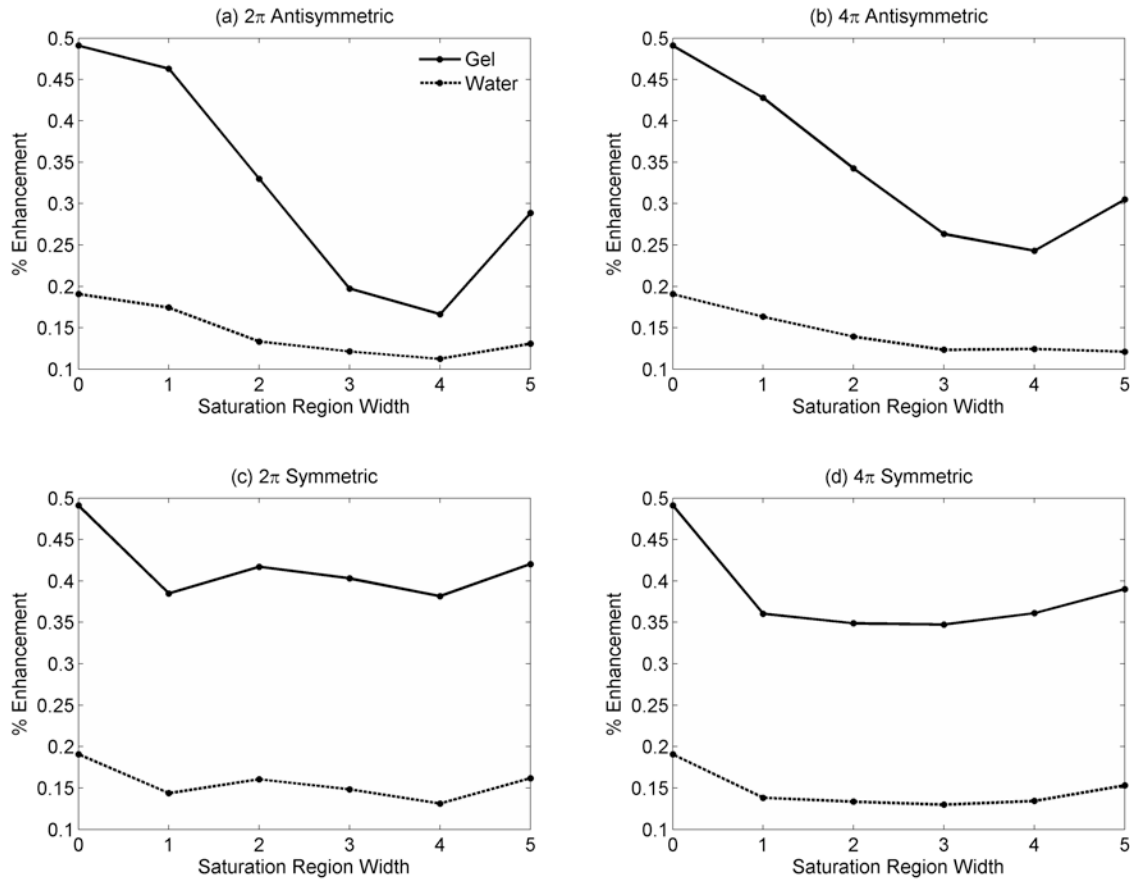
Figure 3-16 Signal of stationary structures in the phantom.

The stability of the signal of stationary structures in the phantom is shown is shown for two different choices of the sideband phase gradient (a vs. b and c vs. d), as well as for asymmetric vs. symmetric profiles (a and b vs. c and d). More stable behavior is observed with the use of the symmetric pulse, as well as the signal decrease relative to a sinc pulse, as was found in simulations.

3.8 *In vivo* measurements

All experiments and procedures, in this and later sections, were approved by our Institutional Animal Care and Use Committee, which is accredited by the Association for the Assessment and Accreditation of Laboratory Animal Care International. Respiratory monitoring of subjects was performed (Model 1025 Monitoring & Gating System, Small

Animal Intruments, Inc., Stony Brook, NY) and animals were kept at respiratory rates of 20-30 breaths per minute. Constant temperature was maintained with a water-heating and recirculation system.

3.8.1 Methods

3.8.1.1 Heart and vessel images

To test the ability of the pulse to perform flow suppression *in vivo*, short axis images of the heart were acquired using with a spoiled gradient echo sequence. Cardiac motion artifacts were suppressed by averaging. Acquisition parameters were: TE = 1.7 ms, TR = 40 ms, matrix size = 128x128, FOV = 3x3 cm, receiver bandwidth = 80 kHz, number of averages = 20, flip angle = 35°, pulse duration = 1 ms, slice thickness = 1 mm. Symmetric and asymmetric composite RF pulses with $\alpha = 1$ and 2 and $\omega_2/\omega_1 = 1$ to 5 were used, as well as a sinc pulse. ROIs were drawn on the interior of the left ventricle and on the fat in the shoulder to measure the signal change with the width of the saturation region.

Additional *in vivo* measurements were performed using the symmetric pulse with $\alpha = 2$ for wider saturation bandwidths and at two anatomic locations. Comparisons were made between structures with linear and tortuous flow to investigate the possibility of signal bias due to incomplete spoiling of the initial signal peak. Separately acquired short axis images of the heart and an abdomen, in which the inferior vena cava (IVC) was visible, were acquired using a spoiled gradient echo sequence in separate acquisitions. Acquisition parameters were: TE = 1.7 ms, TR = 40 ms, matrix size = 128x128, FOV = 3x3 cm, receiver bandwidth = 80 kHz, number of averages = 20, flip angle = 30°, pulse duration = 1 ms, slice thickness = 1 mm. Composite RF pulses with $\alpha = 2$ and $\omega_2/\omega_1 = 1$ to 7 were used, as was a sinc pulse. The signal

in each image was normalized to the signal of muscle from each slice. Average

signal intensities of the blood within the left ventricle and the IVC were measured.

3.8.1.2 VIF measurement

The change in sensitivity to the presence of contrast agent with and without the

presaturation was demonstrated by interleaving VIF acquisition in the heart with a flow

suppressed pulse with measurements made with a sinc pulse in the same anatomy. Baseline T_1

measurements were performed using a variable flip angle protocol with a spoiled gradient echo

sequence. Acquisition parameters common to all images were: TE = 1.7ms, TR = 40 ms,

matrix size = 128x96, FOV = 3x3 cm, slice thickness = 1 mm, receive bandwidth = 80 kHz,

number of averages = 10. For the composite RF pulse, which was symmetric, the saturation

width was 5 mm and α = 2. The flip angles used for the T_1 measurement were 10º, 20º, 30º,

and 40º. The T_1 was calculated by fitting the measured signal to the signal equation with a

nonlinear least-squares fit (31). After T_1 measurement, a 300 µL bolus of 83 mmol contrast

agent (gadopentetate dimeglumine) was injected through a tail vein catheter. Acquisition

parameters were the same as the variable flip angle measurement, but only a flip angle of 30º

was used. Dynamic images were acquired beginning approximately 30 seconds after injection.

Image acquisition with each pulse was interleaved.

3.8.2 Results

3.8.2.1 Heart and vessel images

In the first set of anatomic images where symmetric and asymmetric pulses were

compared, as the width of the sideband increases, the signal of the blood in the ventricle

decreases to be similar to that of the surrounding myocardium, again indicating that the flow

enhancement effect is being suppressed, as shown in the progression of images in Figure 3-17.

Images with the 2π/mm show considerable banding artifacts that are not visible in the

images with the larger phase gradient. This appears to be due to better spoiling of changes in

the out-of-slice signal with the larger phase gradient. It was not clear if the signal in the left

ventricle had stabilized, so supplementary measurements were performed with wider saturation

regions, and are presented at the end of this section.
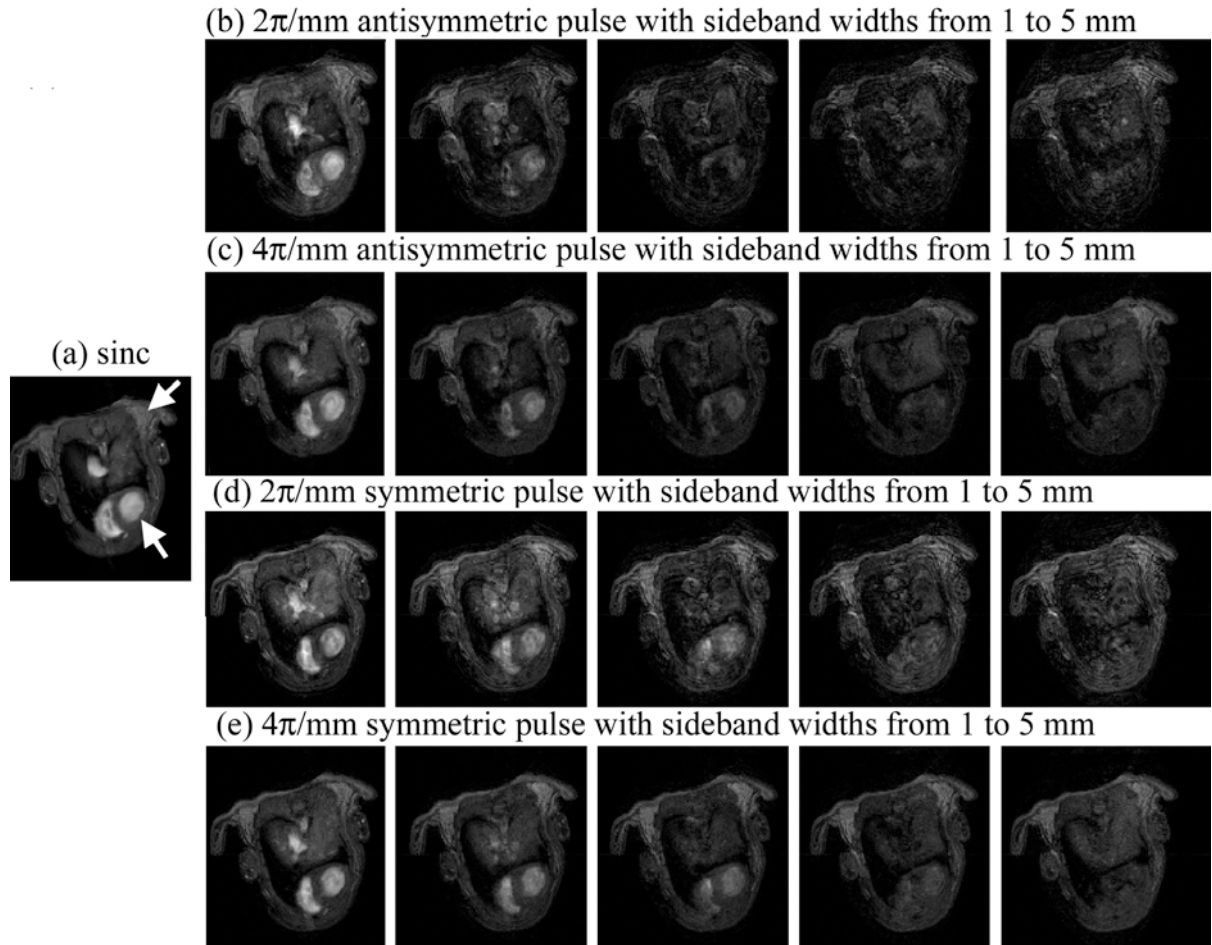
Figure 3-17 Anatomical images acquired with the flow suppressive pulse.

Signal in the blood is, like signal in the catheter, shown to decrease with the increasing

width of the sideband. Signal fluctuations are again visible with the asymmetric pulse,

but not with the symmetric pulse, which effectively suppresses flow without artifacts.

Arrows indicate where signal was measured.

The symmetric pulse produces images with a considerable improvement in the stability of the normal tissue signal as compared to the asymmetric pulse (Figure 3-18). For the 2π/mm asymmetric pulse, the coefficient of variation of the ROI in normal tissue over the width of the sideband is 21.7%, while for the 4π/mm asymmetric pulse it is 15.0%. The coefficients of variation for the 2π and 4π symmetric pulses the coefficients of variation are 5.7% and 3.5%, respectively. This is again consistent with the simulations and the phantom data.
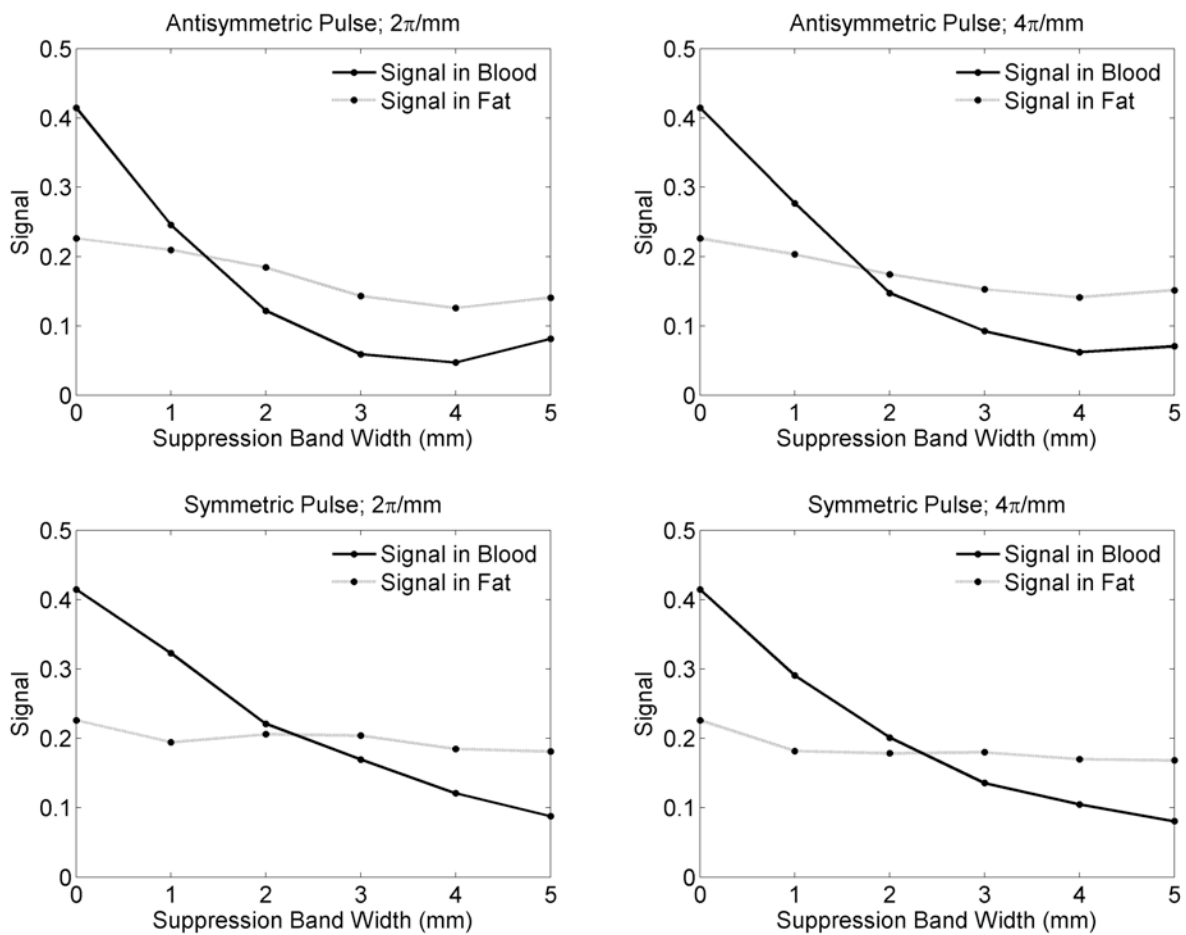
Figure 3-18 Plots of *in vivo* signal in the left ventricle and in solid tissue as the width of the presaturation region is increased.

For all pulses, use of the flow suppressive pulse reduces the amount of flow enhancement. Consistent with previous observations, the symmetric pulses produce more stable signal levels in the stationary tissue.

Because it was inconclusive if the 5 mm width was sufficient to minimize flow enhancement, another set of images were acquired using only the symmetric pulse with $\alpha = 2$. In this set of images, the signal of the blood in the ventricle and IVC again decreases with the sideband width *in vivo*, shown in Figure 3-19, indicating a decrease in flow-related enhancement. The signal from fat was stable as the width was varied (4% CV) while the structures with flowing blood converged to a stable signal after 5 mm of presaturation. The ultimate stability of the signal is a strong indicator that spins are in steady state by the time they reach the coherent region. The bias suggested in simulations with high flow velocity may also be manifest in inferior vena cava and the other veins in the cardiac slice. These vessels remain hyperintense even when the blood in the heart has reached a highly saturated state, which is possible evidence for residual flow enhancement.
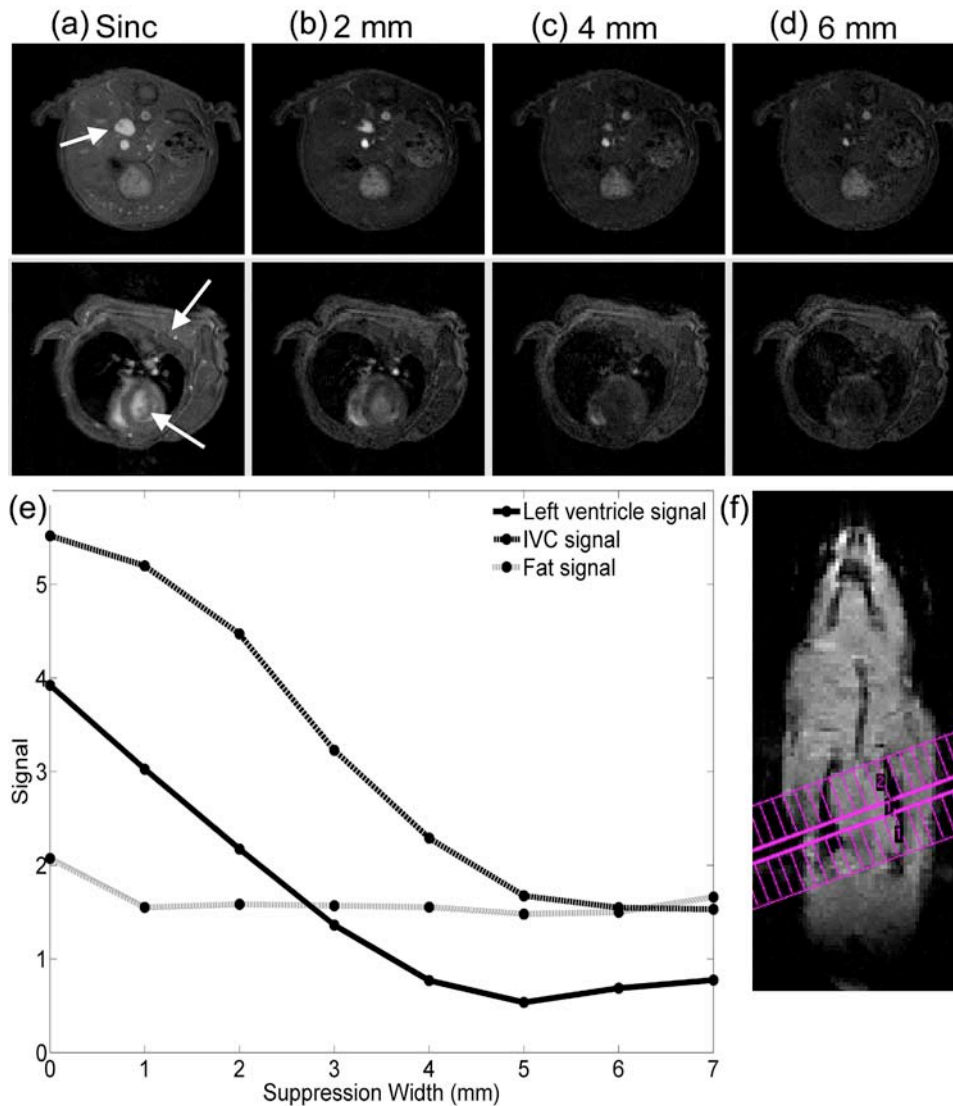
Figure 3-19 Comparison of images acquired at the IVC with the heart.

Images show the IVC and heart of a mouse acquired with a sinc pulse (a) and the flow

suppressive pulse over multiple sideband widths (b-d). Flow suppression is visible even at

narrow bandwidths and a 5mm suppression band is sufficient to suppress inflow

enhancement even within the heart at a TR of 40 ms. The signal from fat is stable as the

sidebands are changed, indicating that the signal from those regions is effectively

suppressed, as shown in part (e). The geometry of the cardiac slice, shown in (f), shows

that the saturation region covers the majority of the lungs and heart, indicating that the

pulse may be particularly suited to flow suppression in the heart, due to the extended period of time blood stays within the saturation region in this case.

3.8.2.2 VIF measurement

The measured T_1 values of flowing blood differed substantially between the conventional sinc pulse and the flow suppressive pulse (Figure 3-20). The former gave 196 ms, while the later gave a measurement of 1739 ms. The value measured with flow suppression is consistent with the values reported by Pickup, *et al*. of 1780±60 ms for mouse blood at 4.7T (10), another indication that the applied suppression sufficiently eliminates inflow enhancement *in vivo*.
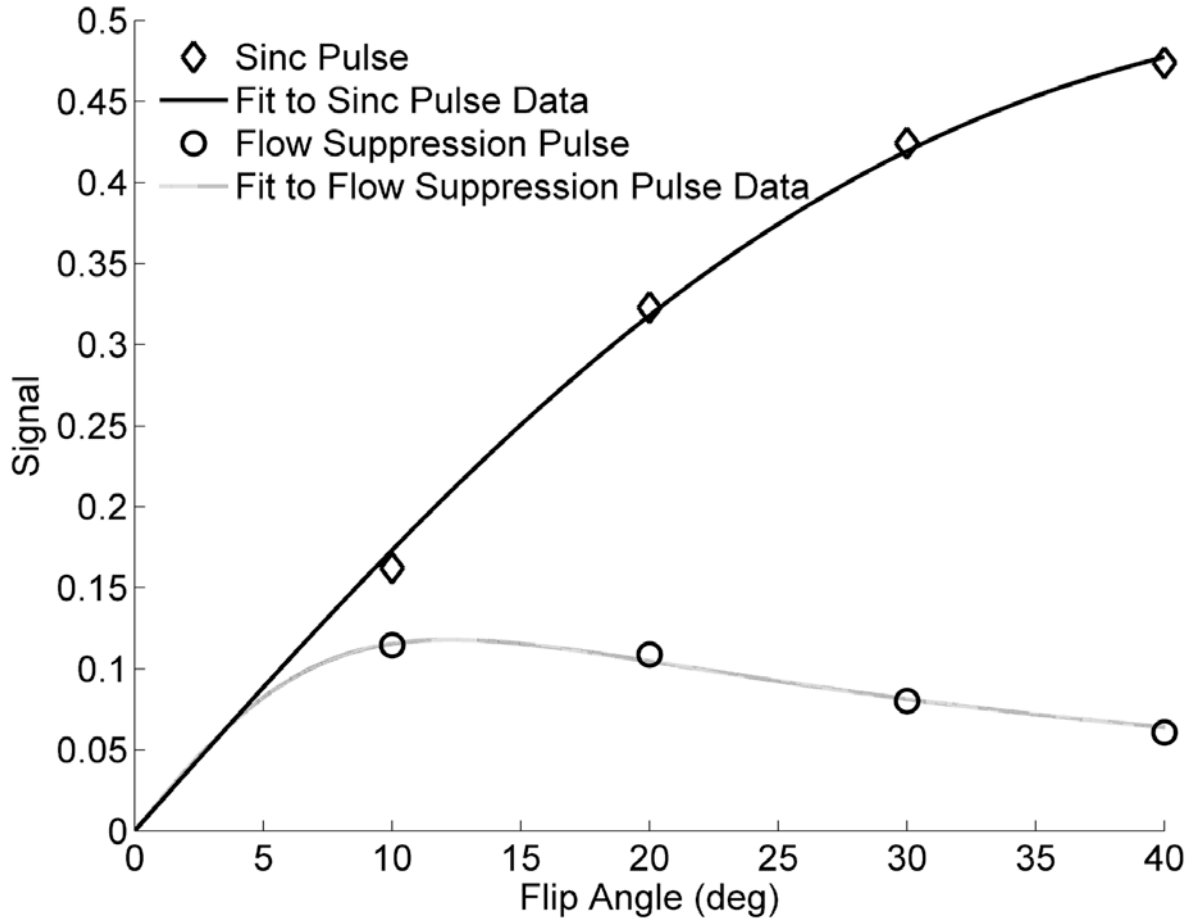
Figure 3-20 T$_1$ mapping signal curves.

The signal measured with the non-flow suppressive sinc pulse continues to increase with flip angle even to a fairly large angle, characteristic of a short T$_1$ tissue. This is not the case of the signal measured with the flow suppressive pulse.
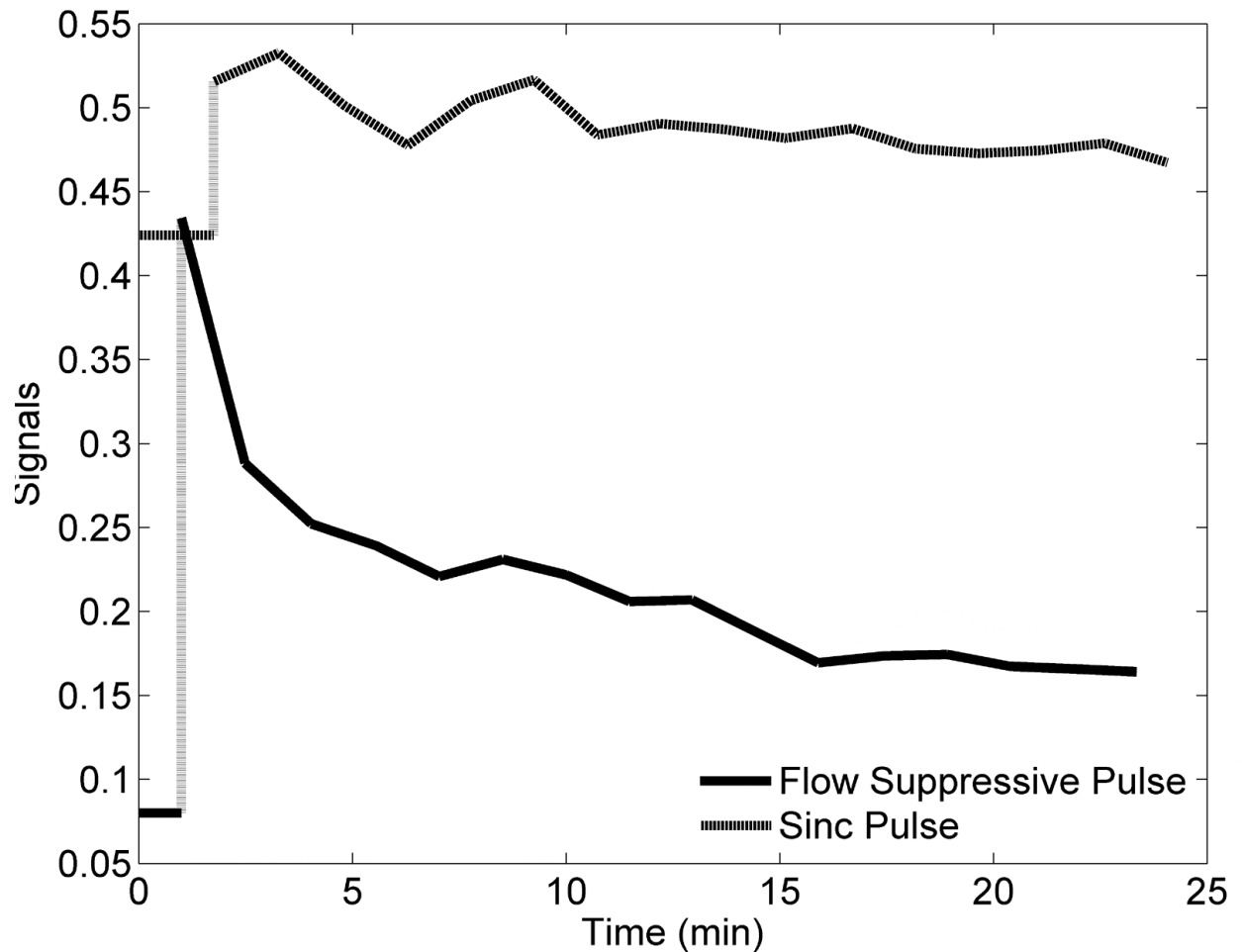
Figure 3-21 Signal time courses measured in the heart with conventional and flow suppressive excitation.

The baseline (pre-injection) signals are shown as horizontal lines. The baseline signal for the sinc pulse is considerably larger than that of the flow suppressive pulse, due to the short apparent T_1 without flow suppression. Because of this, the same amount of contrast agent causes a much smaller signal increase when using the conventional RF pulse.

Comparison of the post-injection signal time courses of the two pulses demonstrates that the loss of sensitivity caused by inflow enhancement (Figure 3-21) with conventional excitation is mitigated by the composite RF pulse. Although the sinc pulse produces a larger baseline signal due to the flow enhancement, the introduction of contrast agent produces only a

25% increase in the signal, while that same contrast agent concentration showed a 450% increase in signal with flow suppression.

3.9 Discussion

Flow suppression is a key component of the planned VIF measurement in the heart. This is well demonstrated by comparing the two VIFs measured in the heart, where much of the structure of the VIF is lost without flow suppression. However, the RF pulse developed here allows for effective flow suppression without requiring additional time in the pulse sequence.

The coherent region at the profile center is the source of the signal, and maximum sensitivity to contrast agent is achieved when spins are at steady state there. Imperfect spoiling may result if the applied phase gradient in the saturation regions is insufficiently sharp, causing residual flow enhancement for linear flow. Residual signal will be maximized if the flow travels in a straight line perpendicular to the slice. This effect was prominent when comparing signal in the IVC, a structure with linear blood flow, to the left ventricle, where blood must pass through the lungs and other three cardiac chambers before entering. The tortuous path blood takes through the saturation region near the heart may make the pulse particularly suitable for use in this region. The signal from the IVC was consistently higher than the signal measured in the left ventricle, with both signals were normalized to muscle. The veins in the thoracic slice containing the heart remained hyperintense even with relatively wide saturation regions.

Two types of waveforms were studied: both symmetric and asymmetric. They differ in that they produce slice profiles with different spatial dependence of the phase in the slice profiles. The symmetric pulse has a peak power requirement which is half that of the asymmetric pulse and produces apparently more effective spoiling *in vivo*, as well as providing a more stable signal. For this reason, the symmetric pulse was preferred for VIF measurement.

Two levels of spoiling were also tested. Greater degrees of spoiling were not tested due to a desire to match the pulse duration to that achieved with a conventional sinc pulse used for imaging. Increasing the phase gradient further would require extending the duration of the RF pulse. Increasing the phase gradient without lengthening the RF pulse would cause the main lobe of the suppression component to be truncated, resulting in severe slice profile artifacts. However, the stability of the signal in normal tissue indicates that image quality can be maintained with the timings used.

The pulses used in this experiment all had a fixed duration of one millisecond and a coherent slice thickness of one millimeter. With these parameters fixed, the design of the RF pulse was limited in two respects. As previously mentioned, the amount of phase change is limited by the shifting of the centers of the component pulses. The maximum width of the sidebands which can be generated is limited by the available RF power of the system because the narrower RF component pulses that generate wider suppression bands require greater amplitude to produce the same tip angle. These constraints were able to be satisfied on the available system, however, different systems have somewhat different limitations, and some modification of the duration of the RF pulse may be required.

With the development of this pulse, we have provided an efficient way for bringing blood into the appropriate steady state magnetization prior to its arrival in the left ventricle. However, while this addresses one limitation of VIF measurement, the temporal resolution which could be attained for the measurement is still limited by the need to acquire k-space for the measurement. This difficulty will be addressed in the next section.

4 Specific Aim 2 – Constrained reconstruction analysis for rapid VIF sampling

4.1 Introduction

High temporal resolution is desired for VIF sampling to achieve accurate or reproducible measurements of pharmacokinetic parameters. A frequently cited target sampling rate is taken from a simulation study by Henderson, which found that a sampling rate of at least once per second is required, in humans, to obtain uncertainty bounds of 10% on all three of the parameters in the extended Toft's model for parameter values typical of breast cancer (39), and other researchers have also found similarly demanding requirements (68). No corresponding estimate of the required temporal resolution for small animal DCE-MRI has been published. It is expected to be higher due to the faster VIF dynamics which occur in mice, although the necessary temporal resolution is not obvious because tissue permeability does not increase proportionally in mice. Additionally, sampling in a short time frame reduces motion-related inconsistencies and prevents the potentially large errors which can occur due to mismatches between the k-space acquisition pattern and the bolus arrival (70).

However, achieving a temporal resolution of even one second with sufficient slice or volume coverage is challenging with conventional acquisition techniques. As will be discussed in the next section, most constrained reconstruction techniques are able to produce acceleration factors of about eight. Reconstruction of a full image with a full complement of anatomical detail from highly undersampled data is a difficult problem. However, simplification is possible when the spatial details are not of interest and the objective is simply the mean signal in an ROI. We have proposed an algorithm, called cardiac anatomy constrained, temporally

unrestricted sampling, or CACTUS, to perform highly constrained reconstruction

which is capable of extracting the desired information from as little as a single projection.

4.2 Techniques for acquisition acceleration

Achieving high temporal resolution can be difficult in MRI, and numerous methods

have been proposed to exploit redundancies and correlations in MR data in order to reduce the

data required for image reconstruction. Many types of constraints and assumptions have been

exploited, ranging from strategic undersampling of dynamic data (88-90), or sparsity

assumptions (91-97), to modeling the image as generalized series (98-103). Parallel

imaging (104) which relies upon using multiple receive coils to introduce additional encoding

may also be used to accelerated image acquisition.

Generalized series type approaches, such as reduced-encoding imaging with

generalized-series reconstruction (RIGR), were originally put forth by Liang (99), although

many other investigators have applied the basic approach in which a dynamically acquired,

undersampled, portion of k-space is extrapolated to be most consistent with a reference image

(105). Some variations also use multiple reference images, such as ones acquired before and

after administration of contrast, which leads to more accurate quantification and more reliable

results (106). This approach, called two-reference RIGR (TRIGR), has been tested for DCE-

MRI purposes. Good results were obtained with 64 and 32 phase encode lines, but at an

acceleration factor of 16 or greater pharmacokinetic parameter maps were rendered

unusable (28). In qualitative imaging situations, such as investigating the motion of the tongue

during speech (105), reasonable results have been achieved with only 8 phase encode lines.

Parallel imaging uses multiple coils with different sensitivity profiles to achieve

acceleration (104). While useful in many applications, the achievable acceleration is limited by

the number of coils used, and dedication of coils to sampling the heart with high acceleration

consumes receive channels that could be used to improve tissue sampling. While potentially a viable tradeoff, it is also a costly one because improvements in sampling the VIF would come at the cost of sampling the tissues of interest.

Highly constrained backprojection (HYPR) was originally designed for magnetic resonance angiography (MRA) and creates a composite image from a set of undersampled data and then retrospectively interpolates a high temporal resolution set of images (95). It has the ability to produce extremely high acceleration factors (~100) for the reconstruction of 3D sparse data sets. In the presence of enhancing background tissue, as would be encountered in a DCE-MRI experiment, a modified approach must be used, such as iterative HYPR (I-HYPR) (96). This modified technique has demonstrated lower acceleration factors, requiring as many as 32 projections per time frame to reconstruct an image (96).

Compressive sensing is a relatively new technique that achieves high acceleration factors by using pseudo-random acquisition strategies to effectively transform aliasing artifacts into noise, which is then eliminated by a non-linear reconstruction (91,93). It relies on the assumption that there is a sparse representation of the image being reconstructed in some parameter space; a frequent choice is a wavelet basis. Maximum acceleration is determined by the level of detail and structure in the image. Specifically, compressive sensing techniques require 2-5 times as many samples as there are non-zero coefficients in its sparse representation; even at its extreme limit compressive sensing cannot reconstruct a reasonable image from fewer than about a dozen k-space lines (93).

Very large acceleration factors have also been achieved with a technique called SLIM (spectral localization by imaging) (107). It used a reference image to provide a basis for anatomic segmentation, although the reference was not directly used in the reconstruction. This allows sifting different spectra from distinct spatial regions. This technique forsakes any

knowledge of the structure within the regions, but requires minimal data (as few as two phase encode lines) to sample the structures of interest.

We follow in the approach of SLIM by achieving highly accelerated sampling by using anatomical constraints. Like HYPR, we are able to retrospectively interpolate high temporal resolution data from individual projections that compose a complete, low-temporal resolution acquisition. SLIM processes spectroscopic data, and thus in order to achieve spatial separation at least two acquisitions with different phase encoding are acquired. We are not interested in spectroscopic data and in principle only require a single projection. However, preliminary simulations (§4.5) indicate improved robustness with the use of multiple projections.

4.3 Theory

4.3.1 Derivation

This structure-oriented reconstruction is developed in the context of a radial data acquisition scheme. Through the projection-slice theorem, a spoke in *k*-space is related to the full image by

$$S_{k,t}(r_k, \theta) = FP_t(r, \theta) \tag{Eq. 4.1}$$

$$P_t(r, \theta) = \Re S_t(x, y) \tag{Eq. 4.2}$$

where $S_{k,t}$ is the spoke in k-space at angle θ at time t, F is the one-dimensional Fourier transform along the spatial dimension, P_t is the projection at angle θ, and the position along the projection is given by r, $\Re$ is the Radon transform, and $S_t(x,y)$ is the signal intensity distribution in the spatial domain. Solving this system of equations for a full set of projections reconstructs the image and is the approach used in a conventional algebraic reconstruction technique, where the image reconstruction equation is expressed as a matrix whose coefficients are determined by ray-tracing through a grid (108).

To simplify the system of equations, reducing the number of unknowns and decreasing the number of projections required, we partition the image into N ROIs, defining the indicator function for the ith ROI as:

$$\chi_i(x,y) = \begin{cases} 1, (x,y) \in \text{ROI}_i \\ 0, (x,y) \notin \text{ROI}_i \end{cases} \qquad \text{(Eq. 4.3)}$$

We assume that the ROIs enhance smoothly, in the sense that, for a voxel at position x,y located within the ith partition:

$$I_t(x, y) = w_i(x,y,t)I_0(x, y) \qquad \text{(Eq. 4.4)}$$

where I_0 is a reference image of the anatomy and $w_i(x,y,t)$ is a smooth contrast modulation function for the partition that relates the dynamic images to the reference. We can expand this function as a Taylor series in the spatial dimensions:

$$w_i(x,y,t) = w_i(x_i,y_i,t) + x \frac{\partial w_i}{\partial x}(x_i,y_i,t) + y \frac{\partial w_i}{\partial y}(x_i,y_i,t) + \cdots \qquad \text{(Eq. 4.5)}$$

where x_i and y_i denote the point around which the Taylor series is evaluated.

Truncating this series reduces the number of coefficients required to describe the dynamic coefficients. This can be considered a form of modeling the image as a set of partially separable functions (109). For our purposes, it suffices to keep only the spatially constant term of the Taylor series

$$\begin{aligned} w_i(x,y,t) &\approx w_i(x_i,y_i,t) \\ &\equiv w_i(t) \end{aligned} \qquad \text{(Eq. 4.6)}$$

This physically corresponds to assuming homogeneous enhancement within the ROI. Spatial details are not needed for VIF measurement, only the mean signal within the blood in the left ventricle. Combining the above equations leads to

$$P_t(r,\theta) = \Re\left[\sum_i \chi_i(x,y)I_t(x,y)\right]$$

$$= \sum_i \Re\left[w_i(x,y,t)\chi_i(x,y)I_0(x,y)\right]$$

$$\approx \sum_i \Re\left[w_i(t)\chi_i(x,y)I_0(x,y)\right]$$

$$= \sum_i w_i(t)\Re\left[\chi_i(x,y)I_0(x,y)\right]$$

(Eq 4.7)

The linearity of the Radon transform allows bringing the spatially constant, temporally varying value of w_i outside of the transformation. This produces a set of linear equations in a number of unknowns equal only to the number of partitions.

To solve the system of equations, we express the equations as a matrix

$$P_t(r,\theta) = \left(\Re_\theta\left[\chi_i(x,y)I_0(x,y)\right] \quad \Re_\theta\left[\chi_2(x,y)I_0(x,y)\right] \quad \cdots \quad \Re_\theta\left[\chi_N(x,y)I_0(x,y)\right]\right)\begin{pmatrix} w_1 \\ w_2 \\ \vdots \\ w_N \end{pmatrix}$$

(Eq. 4.8)

assuming N segments and recognizing that the signal and Radon transform terms are vectors with a length equal to the number of readout points. Modifying the algorithm to include projections at multiple angles is straightforward:

$$\underbrace{\begin{pmatrix} P_t(r,\theta_1) \\ \hline P_t(r,\theta_2) \\ \hline \vdots \\ \hline P_t(r,\theta_M) \end{pmatrix}}_{P} = \underbrace{\begin{pmatrix} \Re_{\theta_1}\left[\chi_1(x,y)I_0(x,y)\right] & \Re_{\theta_1}\left[\chi_2(x,y)I_0(x,y)\right] & \cdots & \Re_{\theta_1}\left[\chi_N(x,y)I_0(x,y)\right] \\ \hline \Re_{\theta_2}\left[\chi_1(x,y)I_0(x,y)\right] & \Re_{\theta_2}\left[\chi_2(x,y)I_0(x,y)\right] & \cdots & \Re_{\theta_2}\left[\chi_N(x,y)I_0(x,y)\right] \\ \hline \vdots & \vdots & \ddots & \vdots \\ \hline \Re_{\theta_M}\left[\chi_1(x,y)I_0(x,y)\right] & \Re_{\theta_M}\left[\chi_2(x,y)I_0(x,y)\right] & \cdots & \Re_{\theta_M}\left[\chi_N(x,y)I_0(x,y)\right] \end{pmatrix}}_{A} \underbrace{\begin{pmatrix} w_1 \\ w_2 \\ \vdots \\ w_N \end{pmatrix}}_{w}$$

(Eq. 4.9)

where a horizontal line implies concatenation and assuming M projection angles. Denoting the matrix containing the reference data as A, the measured signal vector as P, and the weighting coefficient vector was w, we have

$$P = Aw$$

$$\text{(Eq. 4.10)}$$

Because there is one equation for each point along the readout direction, the set of equations will be overdetermined. The system of equations may be solved in the least-squares sense (110) to produce coefficients describing the dynamic behavior of the image. Specifically, denoting the pseudoinverse of A as A^+, we may solve for w:

$$w = A^+ P$$

$$\text{(Eq 4.11)}$$

An illustration of the relationship between the segmentation, the derived basis functions, and an an unknown image is shown in Figure 4-1.

It must be noted that the use of this algorithm does not lead to the reconstruction of an image, but rather to mean signals in an ROI. For our application, we are only concerned with the mean signal, and the restriction is appropriate.

After the weighting coefficients for the regions of interest have been determined from a given projection, the signal in that ROI can be estimated

$$\begin{aligned} S_i(t) &= \overline{\chi_i(x,y) I_t(x,y)} \\ &\approx \overline{w_i(t) I_0(x,y)} \\ &= w_i(t) \overline{I_0(x,y)} \end{aligned}$$

$$\text{(Eq. 4.12)}$$

where the bar represents spatial averaging.
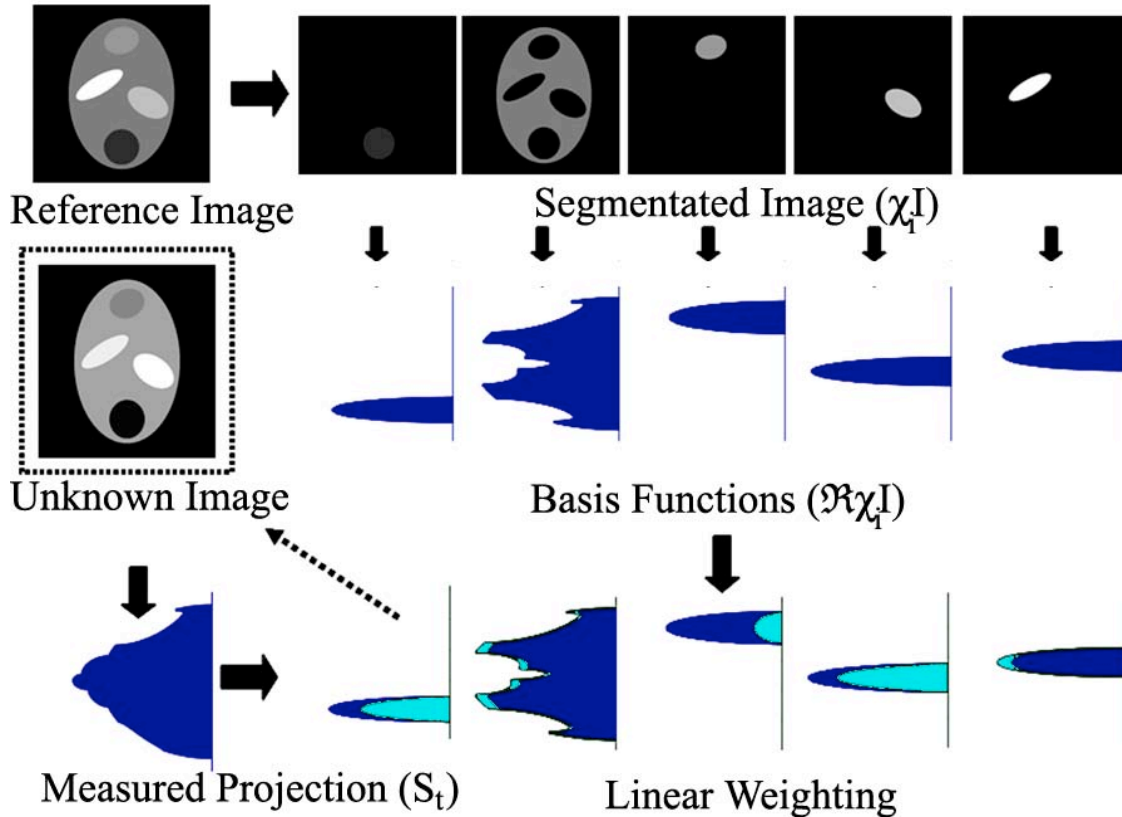
Figure 4-1 Schematic representation of the CACTUS algorithm.

An example application of the constrained reconstruction algorithm is diagrammed in the

figure. A reference image is segmented into several distinct structures; these components

of the image can be transformed into basis vectors by numerically calculating the Radon

transform of the image. Then, a single projection can be acquired of the same anatomy

with different contrast (*i.e.*, after the introduction of contrast agent). A least squares fit of

the shapes from the reference image, as described by the basis functions, to the measured

projection, allows for the reconstruction of the unknown images.

4.3.2 Comparison to other techniques

The technique described here shares many common themes with other approaches for

reconstruction from undersampled data, most notably SLIM. Both CACTUS and SLIM use an

anatomical segmentation to guide interpretation of a very sparse set of phase encode lines. However, CACTUS has several features which make it more suitable to application in dynamic imaging.

The original SLIM algorithm used Cartesian phase encoding to spatially separate signals from different regions, while in this work the Radon transform was used. This difference does not affect the derivation shown; the equations are valid for any linear transformation of the data. However, with the Radon transform the projection angle used can be varied while still obtaining the center of k-space. This allows for the acquisition of fully encoded images that may be used as references and allows the measurement of a low-temporal resolution VIF to serve as a reality check on the constrained reconstruction. While it would be possible to vary the phase encode line used with the Fourier transformation, exclusion of the central region of k-space from measured projections would potentially compromise the SNR of the signal curves produced.

A more substantial difference is that CACTUS uses a true reference image to generate basis functions, unlike SLIM, which uses a uniform image. In the notation used here, this is the same as assuming that $I_0(x, y, t) = 1$. Using a measured reference image has two effects. One is that it causes w to be defined relative to the signal in the reference image. A value of 1 corresponds to the same signal as in the reference image, a value of 2 corresponds to the signal doubling, *etc*. Changing the reference image redefines w. This is of practical importance if the reference image is updated during data acquisition.

The second consequence is that, because w describes the voxel-by-voxel scaling of the image being reconstructed with respect to the reference image, it implicitly accounts for some forms of variation in the image. Spatially varying, temporally constant multiplicative factors, such as the background phase of the image, are inherently included in the reference image. For

example, if two voxels have a background phase that varies by 90°, then signals of 1 and i will become 2 and 2i; which are different absolute changes but the same relative changes. This approach is expected to provide more resistance to background phase variations than the assumption of fully homogenous signal that was used in SLIM because susceptibility-related phase variations across the image can lead to signal fluctuations in tissue when the projection angle changes. A comparison of reconstruction using both the CACTUS approach to reference images and the SLIM approach will be performed in §4.13 .

Ideally, uncertainty due to reconstruction errors should be less than the background noise of the image. Image SNR levels cited for DCE-MRI protocols are on the order of 8 (31) to 10 (111); this implies that noise and motion-related fluctuations should be no more than 10% of the signal, and preferably less. We will generally desire 5% uncertainty in this work for signal estimates to keep reconstruction-related artifacts below the noise level of the image.

4.4 Numerical phantom simulations

4.4.1 Methods

Dynamic enhancement was simulated in a numerical phantom to demonstrate the proof-of-principle that the CACTUS algorithm can produce accurate signal measurements even in the presence of imperfectly homogenously enhancing tissue. The feasibility of the CACTUS algorithm was tested in a dynamic numerical phantom, shown in Figure 4-2a, containing a small region that rapidly changes to model the vasculature and several large slowly enhancing regions that represent normal tissue. Each voxel of the phantom was assigned an independent T_1, K^{Trans}, and v_e chosen from a Gaussian distribution with a standard deviation of 25% of the mean of that parameter for that tissue type. Enhancement was simulated by assuming the two-parameter Tofts model and a biexponential AIF:

$$C_p(t) = 0.15e^{-3t} + 0.1e^{-0.1t}$$

<div align="right">(Eq. 4.13)</div>

with t in minutes and C_p in mmol. Values are taken from Padhani, *et al.*(112), modified to give greater differences between tissues (Table 4-1). A radial acquisition was simulated with TR = 40 ms, flip angle = 30°, number of spokes = 384, matrix size = 512 x 512 over a time of 250 s. Fully encoded images were acquired at a rate of 15.4 s per image; this is not a reasonable sampling rate for VIF measurement but serves to highlight the temporal resolution achieved by the constrained reconstruction algorithm. Both filtered backprojection (FBP) and the constrained reconstruction algorithm were used to measure the mean signal within each ROI. The reference image used in constrained reconstruction technique was a fully encoded pre-contrast image and reconstruction was performed on each individual projection. Signals from both techniques were compared to the true value.

	T_1	K^{Trans}	v_e
Blood	1800 ms	-	-
Myocardium	2100 ms	0.25 min^{-1}	0.2
Muscle	1600 ms	0.125 min^{-1}	0.5
Fat	400 ms	0.05 min^{-1}	0.4

Table 4-1 Parameter values used in the simulation

4.4.2 Results

The numerical simulations of dynamic uptake showed very close agreement between the true signal means and those calculated through CACTUS; the difference between the true and the constrained reconstruction signal for any ROI and any time point was 0.8%. The standard deviation of signal in the ROIs ranged from 14% to 25% of the mean. Measurement

of signals from fully encoded filtered backprojection images, while suitable for the
slower enhancing tissues, was not able to accurately measure the peak of the simulated VIF and
significantly altered the initial rise of the signal and caused a loss of the peak signal, as shown
in Figure 4-2b. Even though the heterogeneity in signal across each ROI was substantial, the
constrained reconstruction approach provided an accurate measurement of the signal mean.

The presence of T_1 heterogeneities prevents the spatially averaged signal from being a
representation of the true concentration level. For this reason, calculations were not undertaken
to test whether mean values would lead to mean estimates of the original pharmacokinetic
parameters. Because blood is a fluid that is continually mixed *in vivo*, heterogeneous T_1
behavior is not anticipated to present a problem for VIF measurement within the left ventricle.
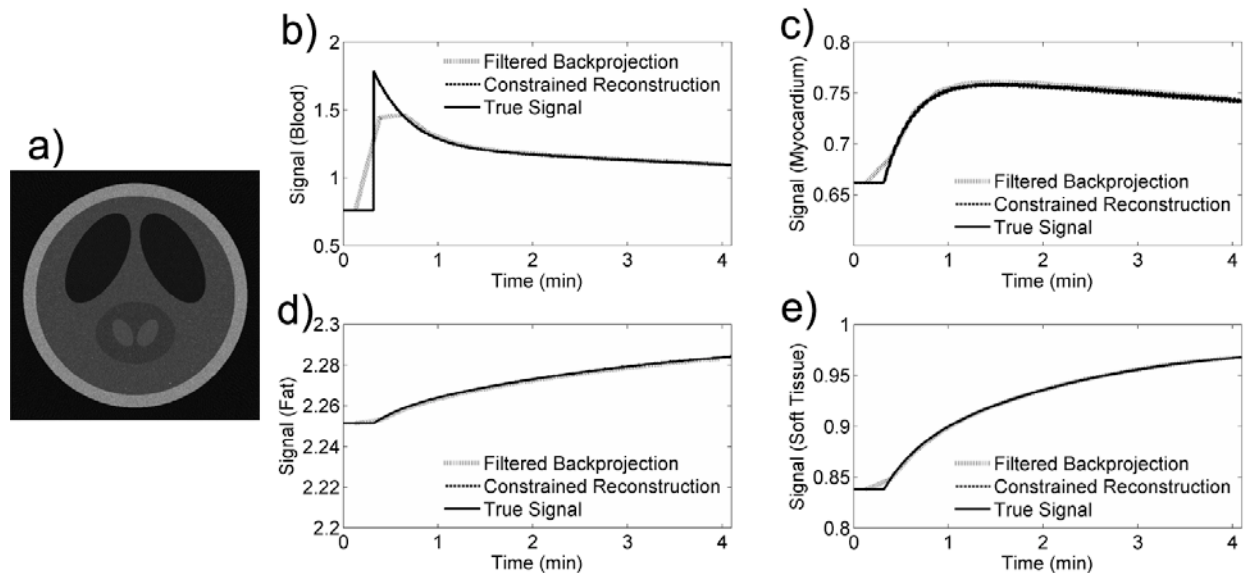
Figure 4-2 Numerical simulation of dynamic uptake.
**The simulated enhancement time courses in the four tissues are plotted. In all cases, there
is excellent agreement between the constrained reconstruction and the true value of the
signal; the true signal and constrained reconstruction are visually instinguishable. The
VIF (b) shows distortion of the initial peak as a result of the prolonged sampling required,
although it is able to characterize the signal of the solid tissues well.**

4.5 Simulation of segmentation errors

CACTUS relies upon an anatomic segmentation. However, segmentation based on anatomical features may not produce an accurate functional representation of the image. Therefore, the impact of segmentation errors on measurements produced by the algorithm was investigated via simulation. Although a theoretical description of all possible segmentation errors is beyond the scope of this work, it is possible to consider example cases which illustrate the effects of errors and provide guidance as to their effects.

The effects of segmentation errors can be quantified by assuming that there is a true segmentation that describes the image dynamics. In this case, there is a true segmentation χ. A second segmentation that contains some error is given by $\tilde{\chi}$. Both segmentations can be used to produce a system matrix from a reference image I_0:

$$\chi, I_0 \rightarrow A$$
$$\tilde{\chi}, I_0 \rightarrow \tilde{A}$$

The true segmentation accurately describes the changes to the image. As a result, given contrast weighting terms, the measured projection can be constructed:

$$p = Aw \qquad\qquad\qquad \text{(Eq. 4.14)}$$

For the flawed segmentation, this does not hold. However, it is still possible is to construct an imperfect estimate of the weighting functions given a projection:

$$\tilde{w} = \tilde{A}^+ p \qquad\qquad\qquad \text{(Eq. 4.15)}$$

Combining these two matrices allows describing errors in segmentation in terms of errors in contrast change:

$$\tilde{w} = \tilde{A}^+ Aw \qquad\qquad\qquad \text{(Eq. 4.16)}$$

This same relationships holds when multiple projections are used in the reconstruction, with the final expression being identical (although the form of A and $\tilde{A}^+$ differ).

Although the most natural example of a segmentation error is a gross failure to identify anatomy, the concept is more general. Other possible errors would include large regions of soft tissue fed by different branches of the vasculature; different regions would show different dynamics, even if grouped as one tissue in the segmentation.

4.5.1 Numerical phantom

4.5.1.1 Methods

We first consider a three-region simulation with a simple geometry. A numerical phantom, shown in Figure 4-3, was created with a large (120 pixel radius) circular "body" ROI, in which were embedded two smaller ROIs. One of the two represented an identified "target" ROI (radius of 24 pixels), while the other represented an occult ROI (variable radius) that is not segmented out of the body. The occult ROI represents some feature which has not been correctly identified. In these simulations we investigate the effects that such a segmentation error has on the signal measured in the other regions.
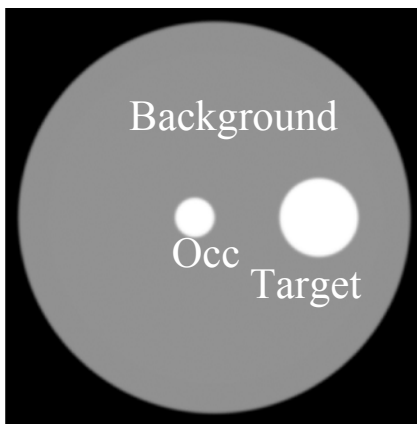
Figure 4-3 Numerical phantom from the occult heterogeneity simulations. The three structures in the simulation are shown, consisting of a background region, a known structure, and an occult structure.

Acquisition and reconstruction from two projections was modeled by taking

the Radon transform of the phantom, and the matrix $\tilde{A}^{+}A$ was calculated for all possible pairs of

projection angles (sampled in 1° steps). The equations produced had the form:

$$\hat{w}_{Body} = w_{Body} + k_{Body}\left(w_{Body} - w_{Occ}\right)$$
$$\hat{w}_{Target} = w_{Target} - k_{Target}\left(w_{Body} - w_{Occ}\right)$$

(Eq. 4.17)

where $\hat{w}_{Body}$ and $\hat{w}_{Heart}$ are the contaminated weighting coefficients of the body and target ROIs,

w_{Body}, w_{Target}, and w_{Occ} are the true scaling coefficients of the three ROIs, and k_{Body} and

k_{Target} are geometry dependent coefficients which describe the leakage of the signal from the

occult ROI into the others. These parameters are dimensionless measures of a partial volume-

like effect that causes the signal between different ROIs to mix. Understanding how k_{Body} and

k_{Target} change with the acquisition geometry allows choosing a geometry that minimizes the

impact of segmentation errors on measurements made using the constrained reconstruction

algorithm.

Three scenarios were considered for the orientation of the projections with the anatomy.

In the first case, one projection was oriented to provide the maximum overlap between the

target ROI and the occult ROI, while the orientation of the other projection varied. In the

second case, one projection was fixed at the minimum overlap of the two ROIs while the other

one was varied. In the last case, the effects of the separation angle between the two projections

was investigated in terms of the maximum amplitude of k_{Body} and k_{Target} for any relative

orientation of the acquisition geometry and the phantom.

4.5.1.2 Results

The numerical simulations indicate that the effects of focal segmentation errors can be reduced, although not completely eliminated, through the use of multiple projections. Considering the case where one projection is fixed to maximally overlap the target ROI and the occult ROI (one projection fixed at 90°), a second projection can reduce the contamination artifact by a factor of ~2.7 when widely separated (Figure 4-4a), at the expense of introducing some contamination (up to 3%) into the surrounding region (Figure 4-4d). However, no choice of projection angles completely eliminates the contamination artifact. Fixing one projection at minimum overlap (0°) produces smaller overall errors, although they are not completely eliminated, except at one particular combination (Figure 4-4be).

However, this discussion relies upon knowing the location of the supposedly unknown object. More relevant to protocol design is to apply a criteria of minimizing the maximum error. Figure 4-4cf illustrates that for any possible orientation of the projections, even a modestly wide separation angle of 40º minimizes the worst case value of k_{Body} and k_{Target}, and that using a wider angle does not cause harm.

These simulations represent the effects of segmentation errors and do not model the effects of noise. Because the primary geometry being considered is the relative orientation of the target and occult ROI, the separation width and angle of the two bodies relative to the body ROI should not strongly affect the curves.

Because of the strong dependence of the partial volume contamination on the projection angle, strong oscillations occurring when the projection angle is varied is an indicator that the segmentation does not fully describe the behavior of the system. Although it may be possible to derive a method for identifying segmentation errors from the structure of the oscillations, at present it remains only a diagnostic marker.
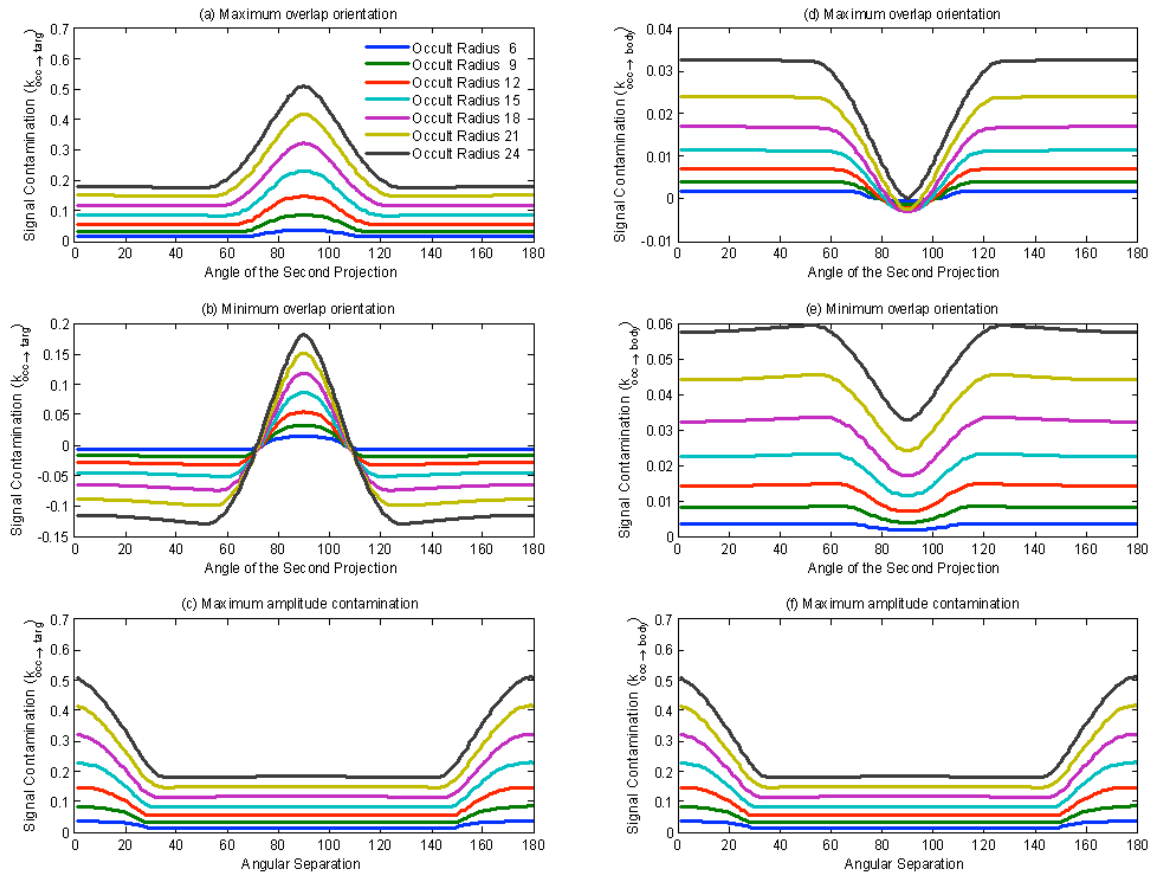
Figure 4-4 Signal contamination, simulated in the numerical phantom.

Subplot a shows the values of k_{Target} for with one projection forced to maximally overlap the target and occult ROIs. Subplot b shows the values when one projection is forced to minimally overlap the two. Analogously, d and e show values for k_{Body}. The maximum value of these parameters for any pair of orientations is given in parts c and f.

4.5.2 *In vivo* simulation

4.5.2.1 Methods

The same calculations were run in a more complicated and realistic geometry. Segmentation was performed of a short-axis view of the heart. A disc ROI was placed in the lung at the level of the heart and its radius was varied from 1 to 5 voxels representing varying

extents of segmentation error. This segmentation was used as the true segmentation,

and the original segmentation was used as the flawed segmentation. The size of the left

ventricle in this image was approximately a circle with a radius of 9 voxels. Proceeding as in

the previous section, $\tilde{A}^+ A$ was calculated for the same combinations of angles.

4.5.2.2 Results

Once again, the error propagation matrices again had a simple form:

$$\tilde{w}_i = w_i + k_i \left(w_{Lung} - w_{Occ} \right)$$
$$\tilde{w}_{Lung} = w_{Lung} - k_{Lung} \left(w_{Lung} - w_{Occ} \right)$$

(Eq. 4.18)

where w_i is the true weighting coefficient of the ith ROI, w_{Lung} is the true weighting coefficient

of the lung ROI, and w_{Occ} is the true weighting coefficient of the occult ROI. The contaminated

solutions are denoted with tildes. The symbols k_i and k_{Lung} represents geometry dependent

coefficients that describe the signal contamination. The segmentation used is shown in Figure

4-5.
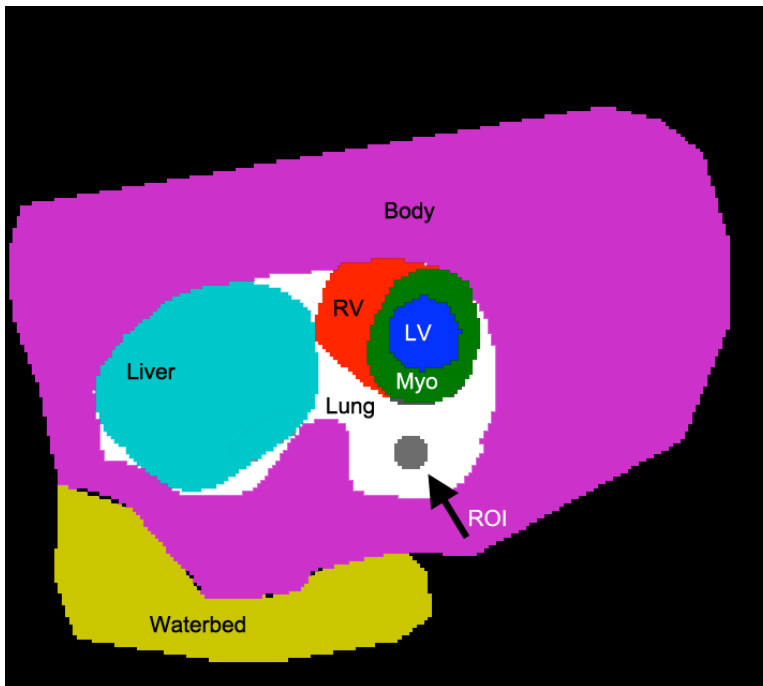
Figure 4-5 Segments generated from the *in vivo* data.

The anatomic structures identified in the segmentation are identified. RV = right

ventricle, LV = left ventricle, Myo = myocardium

The simulations that are inspired by *in vivo* anatomical structures show more
complicated behavior than the numerical phantoms (Figure 4-6). The more complicated
anatomy produces more complicated angular dependence of the segmentation artifacts.
Additional large peaks occur even when the separation of the two angles is relatively large.
However, even in this scenario, a separation angle of at least 60° gives some resistance to the
worst possible artifacts.

Based on these simulations, it was decided that a two projection reconstruction would
be used with a separation between consecutive projections of between 60° and 120°.
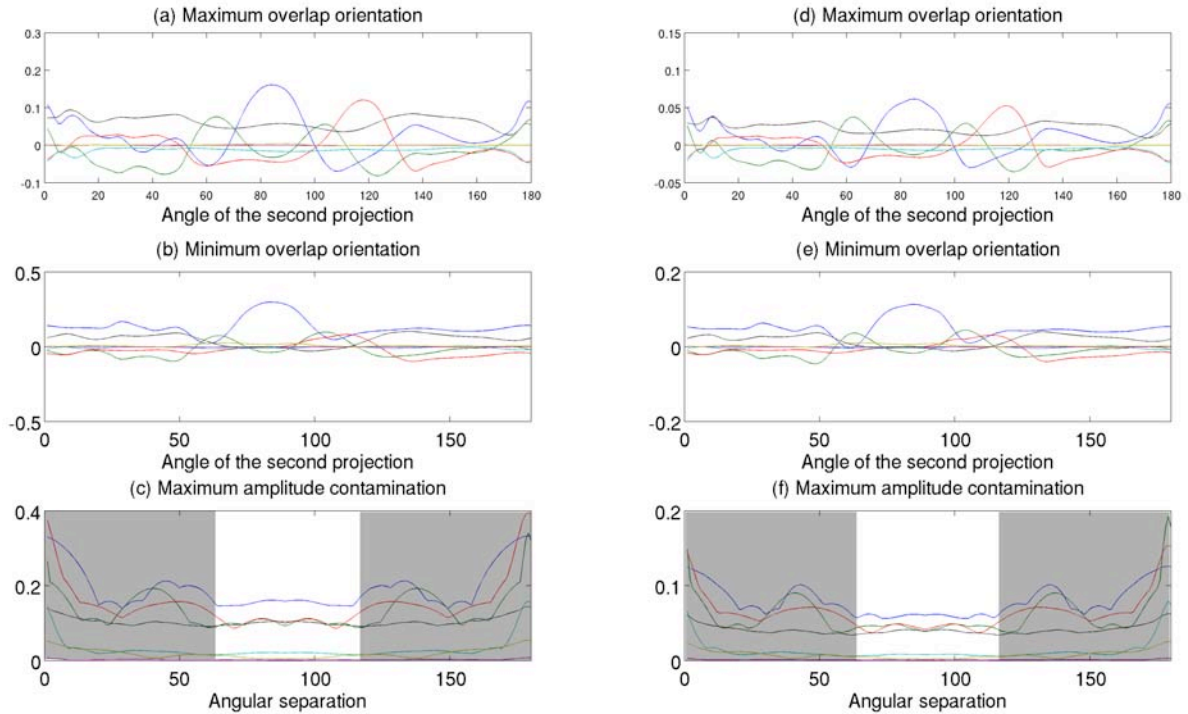
Figure 4-6 Signal contamination, simulated with the *in vivo* data.

The curves from the heterogeneity with radius 5 (abc) have the same structure as those

from the smaller artifact of radius 3 (def), but with lower amplitudes. Colors of the lines

match the ROI segmentation. Although the behavior of the curve is more complex than

those of the numerical phantom, the key point that wide separation of the projection

angles reduces artifacts remains. The unshaded areas in c and f show the region between

separations 60° and 120° where all of the curves are at or near their minima. The curves

for the other size heterogeneities show similar curves, with the magnitude of the

contamination coefficients increasing with larger ROIs.

4.6 Phantom measurements

4.6.1 Methods

The constrained reconstruction algorithm was tested using a phantom containing four samples of water doped with contrast agent (gadopentetate dimeglumine; concentrations: 0.8, 0.6, 0.3, and 0.15 mmol, intended to produce T_1 values in the range of 200 ms to 1000 ms) in a bath of tap water. The use of homogeneous samples provides a good test of the algorithm in the presence of a system which will behave as close as any system will to the homogeneity approximation. Images were acquired of a phantom at multiple repetition times using a projection acquisition strategy; acquisition parameters were: TE = 2.5 ms, flip angle = 90°, acquisition matrix = 256 points over 3.84 cm, number of spokes = 512, receiver bandwidth = 101 kHz. The TRs used were 30, 100, 250, 500, and 1200 ms. Images were reconstructed using complex filtered backprojection; these images were segmented and the mean signal in the ROIs was taken as the gold standard. For every TR, all pairs of projections were analyzed using the constrained reconstruction algorithm for pairs separated by 90°, using the fully acquired image with TR of 1200 ms as a reference image. The mean and standard deviation of the ROI signal estimates from all pairs of orthogonal projections were calculated for all ROIs and flip angles. The segmentation used and a representative FBP image are shown in Figure 4-7.

Additionally, although these measurements were performed for the sake of providing a test of the algorithm in a phantom with varying levels of contrast, it is possible to derive estimates of the phantom T_1 from this data. T_1 estimates for each ROI from both the FBP images and the estimates produced by the mean constrained reconstruction signal were calculated by using a non-linear least squares fitting algorithm in Matlab.

4.6.2 Results

The phantom measurements (given in Table 4-2 and Table 4-3) display good accuracy of the constrained reconstruction algorithm for the four samples, compared to the desired 5% criteria. The difference between the mean signal estimate from all projection pairs using the constrained reconstruction algorithm and the signal from FBP is less than 4% for the samples, except at the longest TR, where the error reached 4.6% for two of the samples. The accuracy of the signal in the water bath was slightly worse, with a mean signal difference ranging from 5.6 to 8.4%, which is still acceptable.
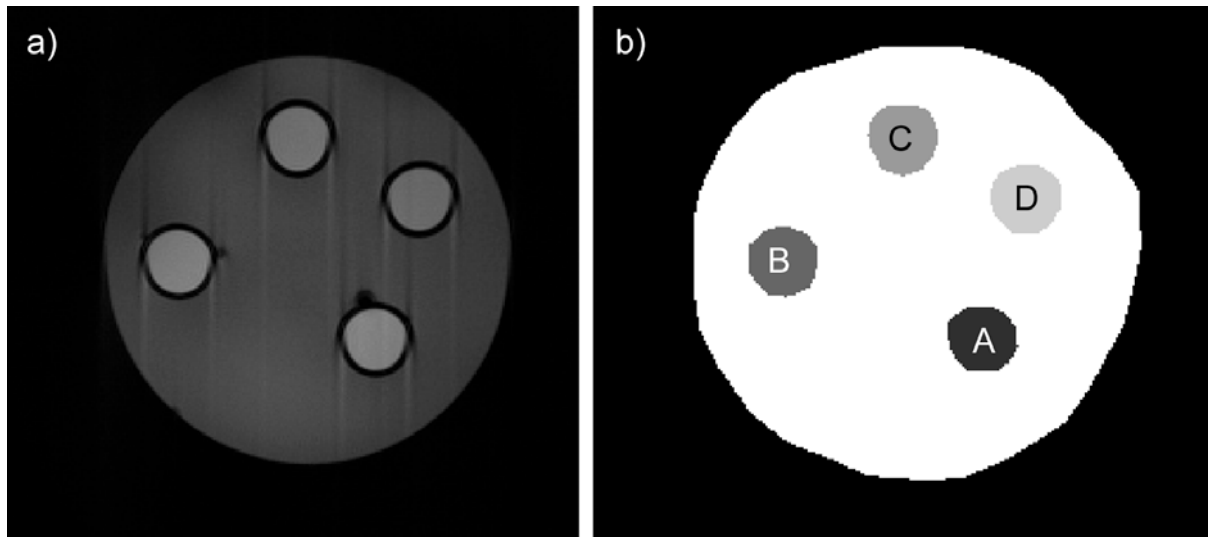
Figure 4-7 Phantom and segmentation used in testing the constrained reconstruction.
(a)   The filtered backprojection image from the image with the longest TR. Some streak artifacts are visible in the image, but they do not severely compromise the results of the constrained reconstruction algorithm. (b) The segmentation used in the reconstruction. Letters correspond to those in the tables below. The water bath was included in the segmentation.

The T_1 values (Table 4-4) between the two algorithms again showed fairly good agreement between the two techniques. The measured values are shorter than anticipated, but

the study was not designed to measure T_1 and the long TR values needed for accurate

quantification of long T_1 values were not acquired.

	30 ms	100 ms	250 ms	500 ms	1200 ms
A	1.3%	1.3%	1.2%	1.2%	1.5%
B	1.9%	2.5%	2.9%	3.7%	4.6%
C	-1.6%	-0.5%	0.6%	2.3%	4.6%
D	-2.5%	-0.8%	-0.3%	1.2%	3.4%
Water	8.4%	7.2%	6.7%	6.1%	5.6%

Table 4-2 Mean errors of the constrained reconstruction analysis for phantom data

Values are expressed as percent difference from the signal measured with filtered

backprojection

	30 ms	100 ms	250 ms	500 ms	1200 ms
A	2.0%	2.0%	2.2%	2.7%	4.5%
B	3.8%	3.9%	4.8%	5.7%	8.6%
C	3.3%	2.3%	2.2%	1.8%	2.6%
D	6.0%	4.9%	4.7%	4.4%	4.9%
Water	4.2%	0.6%	0.4%	0.4%	0.5%

Table 4-3 RMS errors of the constrained reconstruction analysis for phantom data

	A	B	C	D	Water
FBP T_1	82 ms	126 ms	250 ms	337 ms	587 ms
CACTUS T_1	84 ms	127 ms	232 ms	358 ms	599 ms

Table 4-4 T_1 values derived from the signal measurements

4.7 Static segmentation effects

4.7.1 Methods

Because *in vivo* application of the algorithm will face challenges due to mismatches between the segmentation and the anatomy due to cardiac motion, an additional simulation was performed to investigate the sensitivity of the algorithm to mismatches in segmentation due to cardiac motion. A dynamic digital phantom was created, and the structures representing the ventricle and myocardium were constricted to simulate cardiac motion at 17 cardiac phases. Four segmentation schemes were generated:

1) Segmentation representing the anatomy at end systole

2) Segmentation representing the anatomy at end diastole

3) Segmentation representing the anatomy at 50% of the cardiac cycle

4) Segmentation with a ring-shaped transition ROI between the myocardium and ventricle containing the region which has both blood and myocardium during the cardiac cycle

The four segmentations used are shown in Figure 4-8. Synthetic data was generated by taking projections of the phantom during each cardiac phase at 1° increments. Single projection CACTUS analysis was performed of each projection with each of the four segmentation schemes to generate signal curves for each structure in the phantom. No actual changes in the mean signal of each structure were introduced; signal fluctuations are purely the result of motion. The mean and standard deviation of the signal in the ventricle were calculated to compare the effects of motion on the signal measured with each of the four segmentation schemes.

4.7.2 Results

Simulations of cardiac motion show that the limitations of a static model of the anatomy do not excessively compromise the measurement and that the algorithm can produce a measurement that has a low sensitivity to cardiac motion. Time courses of the apparent signal from each segmentation are shown in Figure 4-8. Both the error in the mean and the coefficient of variation were less than 1% when using the additional ring ROI as a dynamic shim (Table 4-5). The other segmentation schemes fared slightly worse: static segmentation based off of the end systole overestimated the signal by 3%, but fairly precisely (2% coefficient of variation). The 50% segmentation was accurate, but with greater uncertainty than the shim segmentation (5% coefficient of variation). The segmentation based on the end diastole segmentation proved the worst, being both least accurate (4% underestimation) and least reliable (7% coefficient of variation). All of these uncertainties are small compared to the large signal changes of up to 400% that occur due to the presence of contrast agent.

	Ventricle	Myocardium	Body	Lung
50%	1.00±0.05	0.69±0.05	0.33±0.00	0.10±0.06
End Systole	1.03±0.02	0.75±0.10	0.32±0.01	0.18±0.10
End Diastole	0.97±0.07	0.62±0.05	0.33±0.00	0.09±0.01
Shim	1.00±0.01	0.65±0.02	0.33±0.00	0.08±0.00
True Value	1	0.67	0.33	0.08

Table 4-5 Mean and standard deviation of simulated cardiac signals measured with four different segmentation schemes.
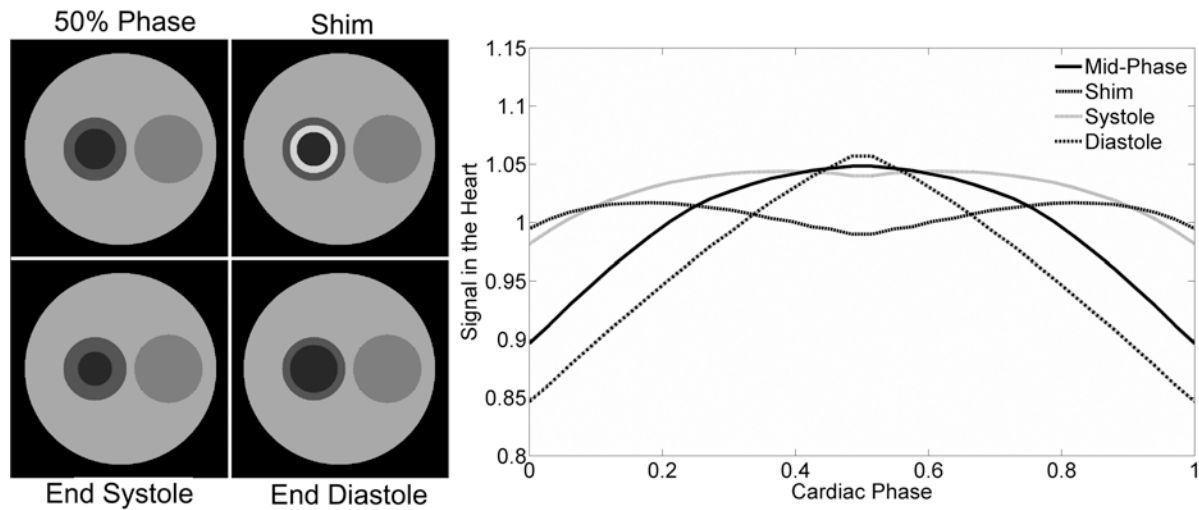
Figure 4-8 Simulated signals in heart that vary with segmentation.

The simulated constrained reconstruction waveforms for the four different segmentation schemes are shown. The segmentation that uses the additional shim ROI stays closest to the true value of 1 over almost all of the cardiac cycle, with the segmentation based off of end systole also performing well. Segmentations based on other phases of the cardiac cycle have large signal changes as a result of the mismatch between the assumed and actual geometry.

Introducing an additional ROI to allow for compensation of cardiac motion has substantial benefits in reducing the signal fluctuations due to cardiac motion. In practice, the easiest segmentation to generate is the average segmentation, because it does not require any form of gating to produce. An approximation of the shim segmentation can be generated from the average segmentation by manually segmenting the myocardium and left ventricle. A shim ROI can be created by using the boundary of the two ROI as its approximate location and dilating the ROI. Because both the systole and the shim segmentation produced accurate results, it is reasonable to expect that such an approximation to the shim ROI will also lead to acceptable results.

4.8 Filtration of the cardiac signal

4.8.1 Methods

Motion is an obvious challenge for sampling of the VIF in a beating heart. The highest level of image quality is achieved through the use of prospective or retrospective gating techniques (113), which allows for reconstruction of images using only single phases of the cardiac cycle. Self-gating approaches, which introspectively analyze the MR signal, are preferred because of distortions involving metallic ECG leads (114,115). However, with the use of the RF pulse for inflow enhancement suppression, the signal from the heart is substantially lowered and the signal change due to cardiac motion is lessened. We investigated reduction of signal fluctuations due to cardiac motion *in vivo*.

A spatially-static projection was repeatedly acquired in a cardiac slice of a mouse with acquisition parameters: TE = 1.55 ms, TR = 18 ms, matrix size = 256 points over 4 cm, flip angle = 30º, slice thickness = 1mm. This measurement was using both a sinc pulse for excitation and a flow suppressive pulse (saturation width = 5 mm). The projection was oriented to not overlap the left ventricle with the right ventricle or great vessels, which would have signal fluctuations which were out-of-phase with the signal from the left ventricle. The signal in a voxel through the largest portion of the left ventricle was measured. Fluctuations in signal would arise through cardiac and respiratory motion. We investigated three candidate schemes for reduction of signal fluctuations due to cardiac motion.

1) Identifying local signal maxima

3) A sliding window mean filter, width varied up to 1.2 s

4) A sliding window median filter, width varied up to 1.2 s

The coefficients of variation for signals measured with both pulses after the application of each filter.

4.8.2 Results

Filtering of the cardiac signal required the temporal resolution compromise of low-pass filtration to substantially reduce the fluctuations in the signal. Coefficients of variation for the maxima filter and two different widths of the sliding window filters are given in Table 4-3. Time courses for selected filters are shown in Figure 4-9. The signal variation produced by assorted widths of the mean and median filters is shown in Figure 4-10. We desire an SNR of 12-20 for comparability with the SNR expected in the images of a DCE-MRI protocol, which can be achieved through filtration. This compromises temporal resolution slightly, but serves to improve the reliability of non-linear fitting. A wide range of filter widths result in acceptable levels of signal fluctuations. The optimal trade-off between resolution and noise is not considered in this work, but two different choices of filter width will be considered in §5.6 and their effects of VIF reproducibility will be considered. A single projection was used without the application of constrained reconstruction on the basis that if a filter failed to reduce variation in the simple case with no other sources of motion or error, then it would be unlikely to provide acceptable results in the more complicated scenario with changing projections. An additional candidate approach for reducing the variation due to motion that uses the shim ROI is investigated in §4.11.

	Sinc	Flow Suppressed Data
Raw signal	**28%**	**45%**
Maxima filter	**21%**	**45%**
1 s mean filter	**3%**	**6%**
0.6 s mean filter	**4%**	**8%**
1 s median filter	**3%**	**7%**
0.6 s median filter	**4%**	**9%**

Table 4-6 Signal CVs of the signal under four filtering choices.
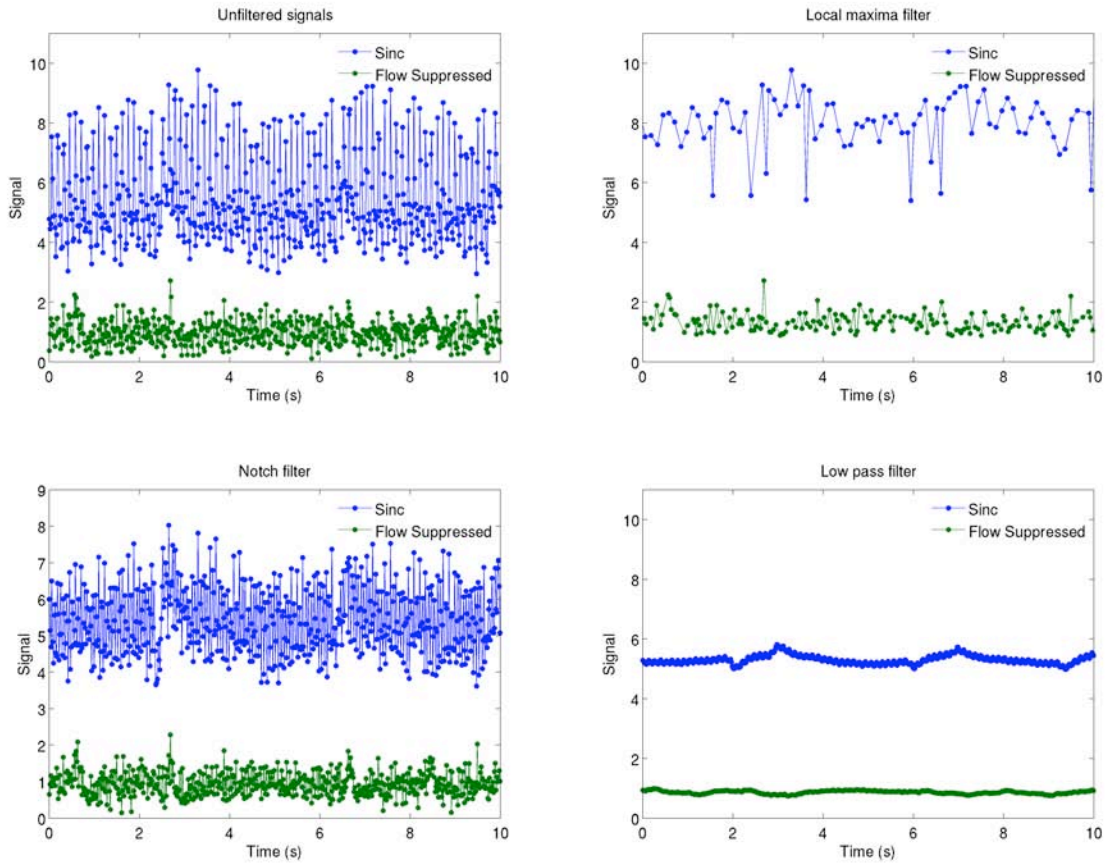
Figure 4-9 Fluctuations in signal due to cardiac motion.

Four different filtering algorithms are shown. Although not an ideal solution because of the reduction in the temporal resolution of the VIF, the low pass filter is the most effective technique for reducing signal fluctuations due to cardiac motion.
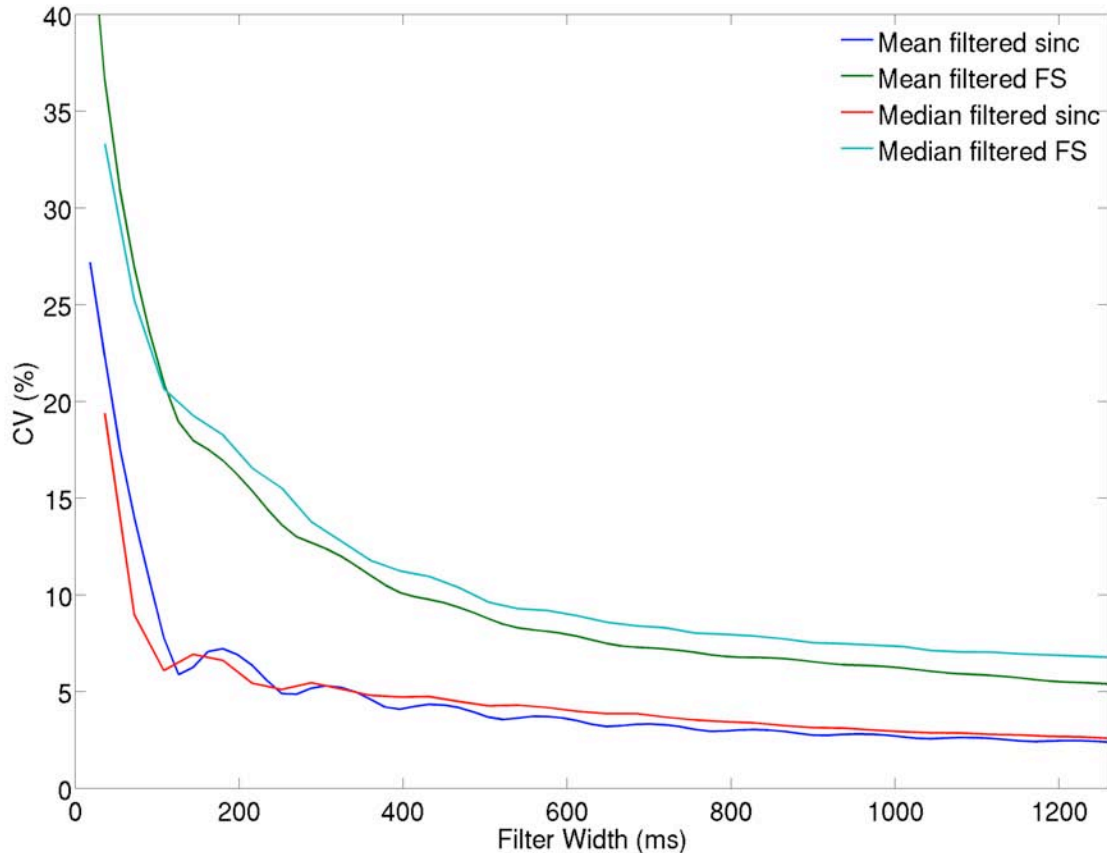
Figure 4-10 Signal CVs produced by mean and median filtration.

At narrow filter widths (<300 ms) the mean filter produces slightly noisier measurements

than the median filter, but this trend reverses itself at the longer filter widths. To obtain

signal fluctuations of the desired magnitude, filter widths of 600 ms to 1000 ms are

needed.

4.9 Retrospective respiratory gating

4.9.1 Methods

Respiratory motion occurs over a longer timescale and is of greater amplitude than cardiac motion, making it easier to identify. During respiration, the lungs expand, pushing the liver and diaphragm out of the slice, causing the signal from the liver to decrease. Because the

liver is explicitly identified during the segmentation process, it is possible to identify time points corrupted by respiratory motion during contrast agent uptake and remove them, avoiding erroneous signal fluctuations.

A radial acquisition was performed of a short axis slice traversing the heart to acquire *in vivo* data for the sake of testing an algorithm for identifying respiratory motion. Acquisition parameters were: TE = 1.5 ms, TR = 40 ms, frequency encode = 256 points over 4 cm, number of spokes = 384, receiver bandwidth = 85 kHz, number of repetitions = 8. Segmentation and reconstruction was performed using the CACTUS algorithm.

Because of the presence of contrast enhancement in the liver, a simple threshold is insufficient. To account for changes in the liver signal during acquisition, the signal in the liver from the FBP image was subtracted from the high temporal resolution liver signal. Then, for each block of high temporal resolution points corresponding to a single FBP image, the points with signal above a percentile threshold of were discarded and not included in any fitting or filtering performed on the VIF. Three threshold levels were investigated: removing the smallest 20% of points, the smallest 25%, and the smallest 30%.

4.9.2 Results

At the 20% and 25% threshold levels some respirations were not identified from the liver signal. The use of a 30% threshold for the gating signal identified all of the sharp drops in the liver signal (Figure 4-11). In the displayed interval, four time points were inadvertently identified as falsely motion-corrupted at this level, indicating that the 30% level is slightly conservative. It was preferable to omit a small number of points from the rapidly sampled VIF than include points with potentially large artifacts, so the more conservative 30% level was used.
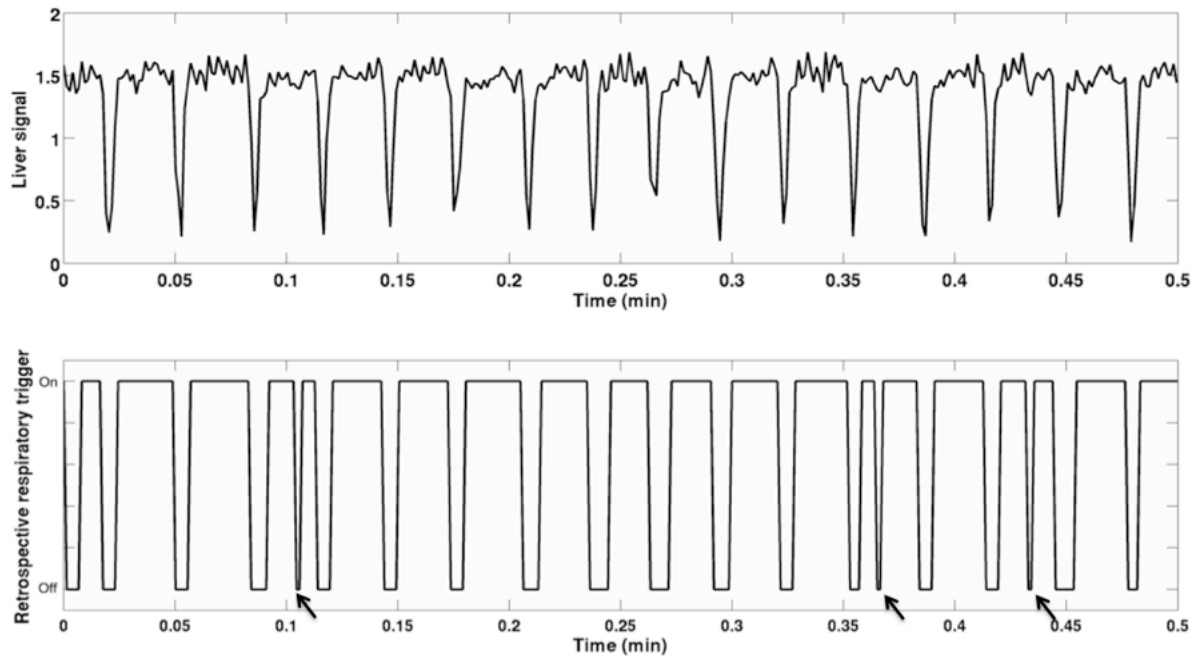
Figure 4-11 Respiratory triggering derived from the liver.

The trigger signal follows the rises and drops of the liver signal well. A few false negatives are present (arrows), although the exclusion of a small number of points out of several thousand is anticipated to be less problematic than including points with large signal decreases.

4.10 Software implementation

To measure VIFs using CACTUS, values are needed for S_t, I_0, and χ_i. The former two quantities can be obtained from MR data; the latter is obtained through manual segmentation of fully encoded images. This is achieved through a guided segmentation script that is run prior to CACTUS analysis. First, postprocessing software performed filtered backprojection on the dynamically acquired projections to produce images with normal temporal resolution. From those images, the operator is prompted to segment structures found in the cardiac slice: left

ventricle, myocardium, right ventricle, lungs, great vessels, liver/diaphragm, portal vein, chest cavity, soft tissue, and the fat around the skin. A two-voxel ring is automatically generated at the boundary of the ventricle and the myocardium to approximate the shim ROI used in the previous simulation. The segmentations are used in the constrained reconstruction algorithm: consecutively acquired pairs of projections are used to produce weighting coefficients, which are used to scale the signal in the reference image, from which the highly accelerated signal could be obtained. The FBP image reconstructed from the temporally closest set of full projection data is used as the reference image. For the protocols used in this work, this led to VIF updates every 81 ms. Respiratory gating was performed by monitoring the signal of the liver ROI, which has a substantial drop in its measured signal during respiration. A 1 s sliding window mean filter was applied to the signal from the left ventricle signal curve to reduce the effects of cardiac motion and noise.

4.11 Variable flip angle measurements *in vivo*

We desire precise measurements of the signal in the left ventricle of the heart. Several components of this aim have focused on techniques to reduce the effects of motion on the signal measured in the left ventricle. The combination of correction techniques which produces the least uncertain measurement of the signal will lead to the most reliable measurements with the constrained reconstruction analysis.

4.11.1 Methods

To test the accuracy of the CACTUS algorithm and assess its sensitivity to cardiac motion, *in vivo* measurements in a mouse heart were performed. Multiple flip angles were used to test the algorithm at different contrasts between blood and tissue. The absence of dynamic changes due to contrast agent allowed for direct comparison of the constrained reconstruction

signal in the left ventricle with that from the filtered backprojection images. Radial acquisitions were performed of a short-axis slice with acquisition parameters: TE = 1.5 ms, TR = 41 ms, flip angle = 10°, 20°, 30°, and 40°, frequency resolution = 256, frequency FOV = 4 cm, number of spokes = 384, angular increment = 120.5°, receiver bandwidth = 85 kHz, number of repetitions = 8. The reconstruction algorithm was performed with and without retrospective respiratory gating and with and without the use of the shim ROI, using the matching FBP image as the reference. For each reconstruction, the temporal coefficient of variation of the left ventricular signal from CACTUS was calculated. In addition, a linear least squares fit was made of the filtered back projection signal to the constrained reconstruction signal values to assess of the accuracy of the constrained reconstruction algorithm.

In addition to these measurements, an approach for decreasing motion-related signal fluctuations exists that could not be performed with the previous single-projection study. The signal in the shim ROI from the constrained analysis will vary with the cardiac cycle. In an attempt to use this for retrospective gating of the cardiac signal, the signal in the left ventricle at time points corresponding to local maxima of the signal in the shim ROI was also considered as a candidate signal. Respiratory gating was used for this measurement. The same analysis was performed on the resulting left ventricular signal as was performed on the filtered waveforms.

4.11.2 Results

The *in vivo* cardiac measurements made with the variable flip angle protocol show that motion-related signal fluctuations can be reduced when both a shim-ROI and respiratory gating are used, which is consistent with the previous simulations. With both respiratory gating and a shim ROI, the line of best fit relating the FBP signal to the CACTUS signal had a slope of 1.012, an intercept of -0.002, and an r^2 of 0.995, indicating a very strong agreement between the two (Figure 4-12a). Additionally, the coefficient of variation of the signal, which includes

variations due to both the cardiac cycle and to changes in the acquisition geometry with projection angle, was low at all flip angles compared to typically SNR values for DCE-MRI studies of 10-12 (111). Measurements made without the corrections for motion showed increases in the signal variation by up to a factor of 3, indicating that the use of the retrospective gating and a shim ROI does provide an improvement in resistance to motion.

Retrospective gating with a shim ROI did not produce an acceptable level of signal fluctuations. The coefficients of variation of the signal ranged from 17% to 50%, which is well in excess of the desired 5% level of uncertainty. For this reason, the low-pass filter approach continued to be used in this work.
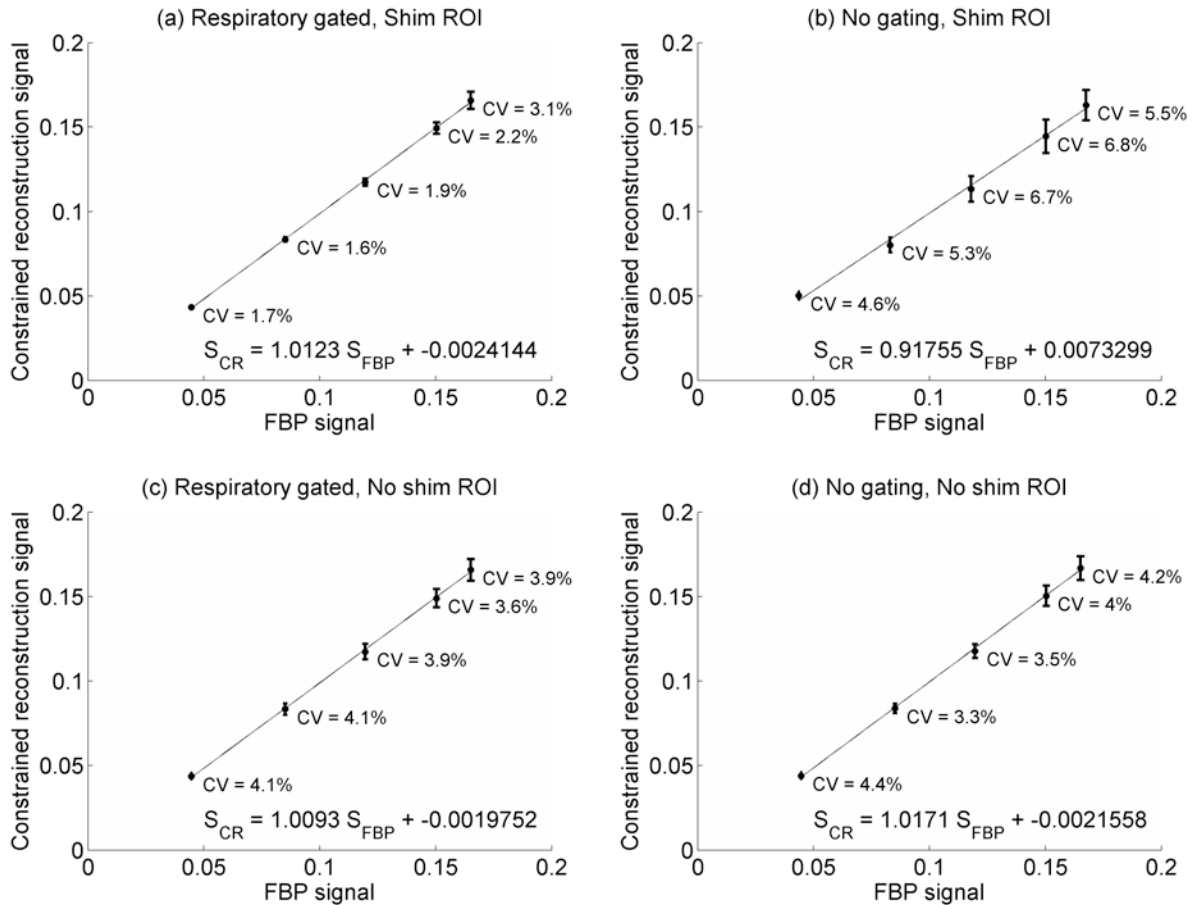
Figure 4-12 Stability of the left ventricle signal with and without respiratory gating and with and without a shim segment.

The measured relationship between the constrained reconstruction signal and the filtered backprojection signal is shown. Across a wide range of signal levels, the constrained reconstruction algorithm matches well to the signal from filtered backprojection. The use of corrective strategies for retrospective gating and the use of a shim ROI together reduce the fluctuations in the signal level significantly.
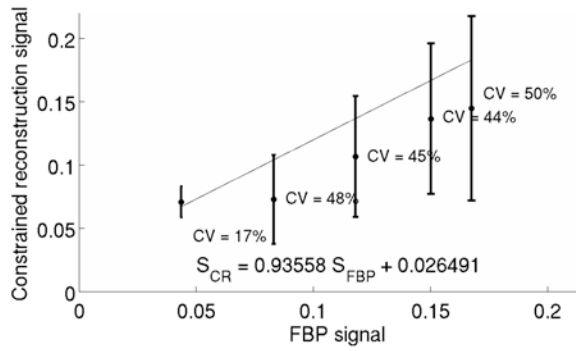
Figure 4-13 Stability of the signal in the left ventricle when performing retrospective cardiac gating through the shim ROI.

Signal fluctuations are considerably higher when using this approach than with the low-pass filtered signals. For this reason, the signal from the shim ROI was not used as a technique for gating.

4.12 VIF accuracy compared to filtered backprojection

4.12.1 Methods

Comparison of the VIF from the left ventricle measured with CACTUS and the ventricular VIF from FBP was performed to assess the soundness of the constrained reconstruction approach. A healthy nice mouse was anesthetized using 0.5%-2% isoflurane in oxygen and placed head-first and supine on an imaging sled. A catheter was inserted into the tail vein. A radial acquisition was performed of a short axis slice traversing the heart. Acquisition parameters were: TE = 1.5 ms, TR = 40 ms, frequency encode = 256 points over 4 cm, number of spokes = 384, receiver bandwidth = 85 kHz, number of repetitions = 30. A bolus of 10 μL of 0.25 M gadopentetate dimeglumine was injected 45 s into the acquisition. Manual segmentation was performed of the dynamically acquired images.

For each FBP image, the constrained reconstruction algorithm produces 192 corresponding high-temporal resolution samples of the signal in the left ventricle from pairs of projections. These groups of 192 projections were binned together, and the mean signal of each bin was calculated and compared to the signal in the FBP image. The RMS difference between the mean constrained reconstruction signal and the FBP signal was calculated. To highlight the difference in temporal resolution between the two approaches, the FBP signal was linearly interpolated in time to match the time points the constrained reconstruction signal was sampled at and the resulting curve subtracted from the CACTUS signal time course.

4.12.2 Results

The left ventricle VIF measurements show visibly close agreement between the filtered backprojection signal and that from the constrained reconstruction approach, shown in Figure 4-14ab. Averaging the signal to decrease the temporal resolution effectively recovers the original FBP signal (Figure 4-14d), with the RMS difference of the two curves shown was only 4.0%, normalized to the mean of the FBP signal. Comparing the constrained reconstruction against the interpolated signal (Figure 4-14c) reveals generally small differences between the two curves except at the initial rise of the curve, indicating both good agreement in slowly changing regions of the curve and improved temporal resolution with the constrained reconstruction approach. These results, although qualitative, suggest that measurement with CACTUS will produce reasonable VIFs with high temporal resolution.
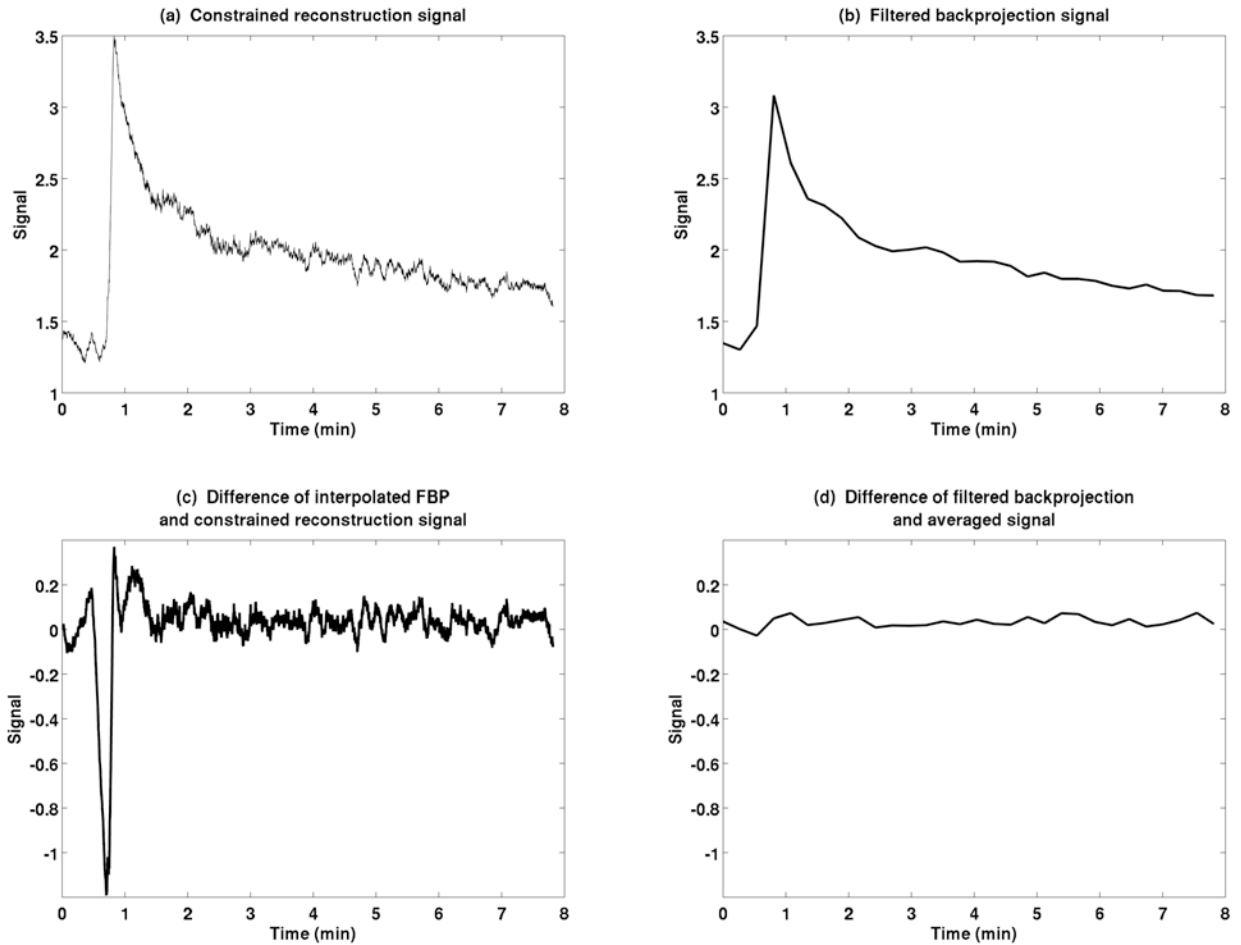
Figure 4-14 Comparison of constrained reconstruction with filtered backprojection. The high temporal resolution signal and the conventionally sampled signal from the filtered backprojection images match well, although as expected the peak of the constrained reconstruction VIF is higher and the rise steeper than for conventional sampling.

4.13 Comparison to SLIM

4.13.1 Methods

As previously mentioned, a key advantage of CACTUS over SLIM is that it uses a measured reference image, allowing for more accurate reconstruction of the dynamic time

course than when a homogenous reference is used. This assumption was tested by reconstructing the previous VIF again, this time with the uniform reference (that is, $I_0(x, y, t) = 1$). Because the uniform reference does not account for variations in the image such as the background phase, orientation-dependant signal fluctuations may occur. The same filtering and post-processing was applied to both curves.

4.13.2 Results

CACTUS produced a VIF with fewer oscillations and artifacts than SLIM for this measurement. Large oscillations are found in the VIF from SLIM, which are very reminiscent of the effects of segmentation errors found earlier. As discussed, these fluctuations occur from changes in the mismatch between the measured signal and the reference image that occurs when the projection angle changes. Additionally, the CACTUS technique lies much closer to the FBP signal in the slowly varying regions, indicating a more accurate reconstruction of the signal.
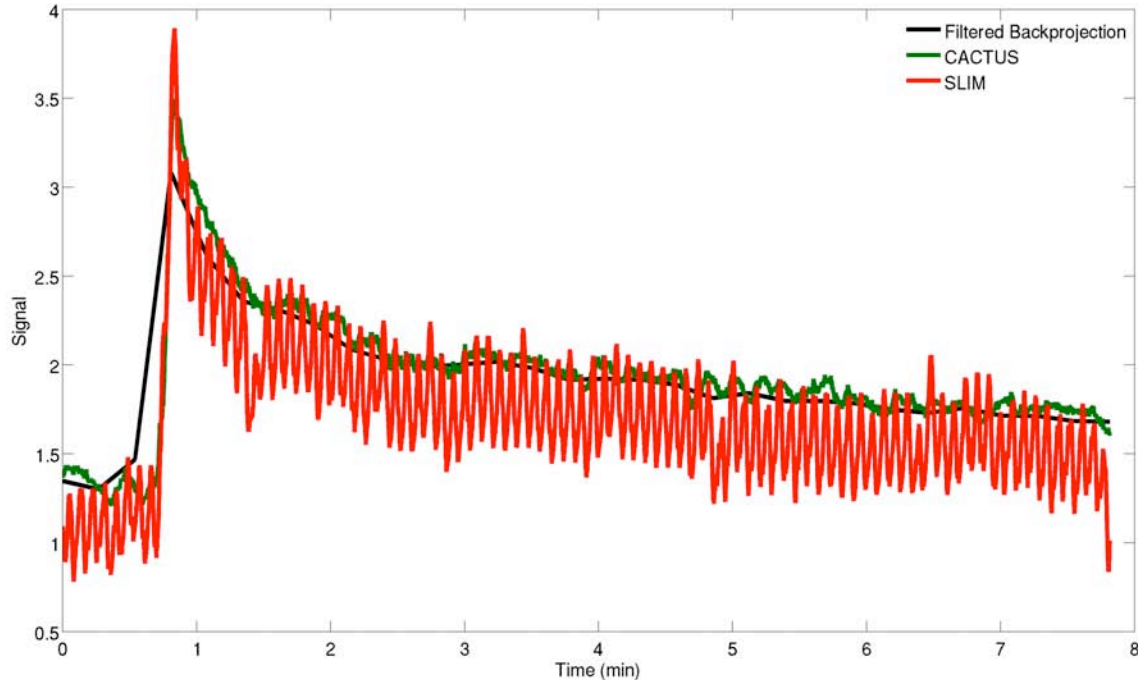
Figure 4-15 VIF reconstruction with both CACTUS and SLIM.

Measurements made with both constrained reconstruction approaches, as well as the FBP

signal, are shown. CACTUS produces a measurement that is more stable with projection

angle (and thus, time) than SLIM. In addition, the CACTUS signal time course more

closely matches the FBP signal in the slowly varying portion of the VIF.

4.14 Discussion

We have developed a strategy for reduced artifact acquisition of the VIF that relies upon

measurement in the heart, which provides resistance to partial volume effects and an improved

signal to noise ratio due to its large size, and by using a constrained reconstruction approach,

which provides high temporal resolution measurement of the VIF.

The constrained reconstruction algorithm developed and used here relies upon a simple

approximation that allows very large imaging acceleration factors. The homogeneity

assumption, while not necessarily applicable to tumor tissue, or other heterogeneous areas, is

reasonable for the slowly enhancing soft tissues and muscle found in the chest. This does not compromise the interpretation of the measurements; the figure of ultimate interest is the mean signal in the left ventricle. *In vivo* application of the algorithm demonstrates that it provides a high temporal resolution measurement of the VIF that is sufficient to capture the first pass of the contrast agent through the vasculature. Because tumors often display greater enhancement heterogeneity than normal tissue, care may be needed when disease is present near the heart. If the tumor does not enhance homogenously, then it may be necessary to segment the tumor into multiple structures with different dynamics, or to include higher-order terms of the Taylor series in the reconstruction.

Because all tissue has some level of small-scale structure, such as vasculature, that would be tedious to manually identify and segment, the segmentation used will necessarily be an imperfect representation of the dynamic changes in the image. Small structures are likely to vanish within the image noise and the limited image resolution. Larger structures could be identified and included in the segmentation.

The numerical simulations indicate that the algorithm can accurately reconstruct highly undersampled data, even in the presence of spatially incoherent fluctuations. Mismatches between the segmentation and the actual dynamics of the image present larger challenges, but these may be minimized through the use of a shim ROI and low pass filtration. Numerical simulations indicate that the use of a second projection reduces errors associated with imperfect segmentation. Phantom data shows agreement of the CACTUS measurement with a full acquisition to within a few percent. This is also found by comparing the CACTUS measurements to those from FBP, which demonstrates that the constrained approach produces a measurement which is consistent with the slowly changing component of the VIF, yet which produces a sharper and more realistic rise of the contrast agent. The temporal resolution

achieved is faster than the cardiac cycle of a mouse, to the point where it is

reasonable to sacrifice temporal resolution for the sake of motion and noise suppression.

5 Specific Aim 3 – *In vivo* study of VIF repeatability

5.1 Introduction

With methods for both flow suppression and high temporal resolution sampling in place, whether their combination results in a superior approach for measurement of the vascular input function in mice can now by tested. The intra-subject and inter-subject variances in VIF measurement using these techniques in a population of mice were evaluated. The hypothesis of this work is that intra-subject coefficients of variation will be reduced, but we also anticipate that a decrease in the inter-subject variation will be achieved.

5.2 Inflow enhancement of cerebral blood vessels

The reproducibility study compared interleaved acquisitions of slices through the heart and the head and neck region. To fairly compare VIFs measured at each location, inflow enhancement must be suppressed in the local vessels as well as the heart. However, performing a full saturation recovery protocol for the head and neck region was infeasible because it would compromise the temporal resolution of the cardiac slice. The effects of the cardiac slice itself on the inflow enhancement in the head and neck region was investigated.

5.2.1 Methods

Since the VIFs are to be simultaneously measured in two different slices, it is possible that the RF pulses that excite the heart, specifically designed to mitigate inflow enhancement, will introduce some presaturation into the local vessel measurement if the travel time is shorter than the T_1 of the blood. This will reduce the inflow enhancement artifacts found in the local

blood vessels. We evaluate the signal found in the internal carotid artery and a cerebral vein in response to the presence of the applied presaturation in the heart.

A 2D gradient echo acquisition was performed of slices through the head and neck of a healthy nude mouse with the following acquisition parameters: TE = 1.55 ms, TR = 41 ms, flip angle = 30°, matrix size = 256 x 256, FOV = 4 cm x 4 cm, slice thickness = 1 mm, slice spacing = 0.5 mm, number of slices = 7, number of averages = 5. In addition, flow suppression was applied with the following schemes:

1) No flow suppression

2) Varying widths of a flow-suppressive excitation pulse applied in the heart (12 mm offset from the head and neck slices), from 1 to 11 mm, which corresponds to the geometry intended for typical VIF measurement (i.e., 11 mm corresponds to 1 mm slice and a pair of 5 mm presaturation regions on each side)

3) A narrower gap (7 mm) between the neck and the flow suppressed area

4) A wider gap (15 mm) between the neck and the flow suppressed area

5) Minimal gap between the neck slices and the suppression region, corresponding to the use of an additional RF pulse at a 30° flip angle to provide optimal flow suppression for the local tissues. Widths of flow suppression of up to 22.5 mm

Signal was measured in the internal carotid artery (ICA) and in a vein outside the skull and normalized to the signal level of that same vessel with the 22.5 mm of flow presaturation. To account for motion during the course of the examination, the baseline signal measurement (geometry 1) was repeated before each of geometries 2, 3, 4, and 5.

5.2.2 Results

The signal was found to decrease substantially in the ICA (Figure 5-1a), for which the presence of an 11 mm presaturation region at the heart produces a 40% drop in signal,

compared to a 41% signal drop from a 22.5 mm presaturation region applied

adjacent to the slices. Suppression in the veins is less effective with both techniques (Figure

5-1b). The same 11 mm of presaturation decreases venous signal by 8%, which is the same as

the comparable amount using the adjacent presaturation region. With 22.5 mm of presaturation

adjacent to the head and neck slices, the venous signal decreases somewhat more at the full

width to 16%. Suppression is more effective in an artery than in a vein, indicating that the

fairest vessels to choose from comparison are arteries. These results suggest that local vessel

VIF measurement with an 11 mm excitation region in the paired experiment in the heart is a

good approximation of what could be achieved with a dedicated presaturation component of the

pulse sequence.
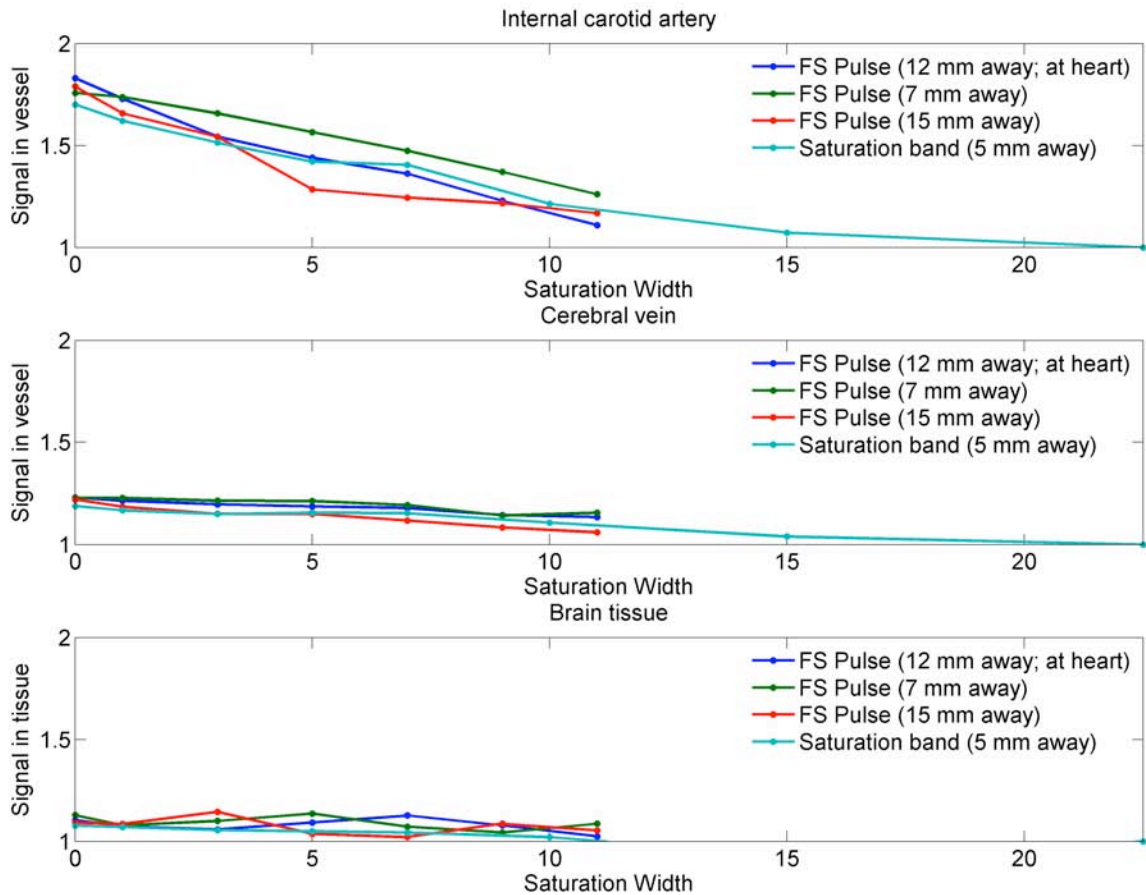
Figure 5-1 Indirect flow enhancement suppression of cerebral vessels.

Arterial signal is significantly attenuated by the presence of a dedicated saturation band, as it is with the indirect suppression applied at the heart. Zero on the width-axis corresponds to no suppression. The saturation regions applied caudal to the head are relatively less effective at decreasing venous signal. Signal in brain tissue is stable with the saturation width applied.

5.3 Animal preparation

Reproducibility studies were performed in healthy nude mice. A total of five animals were placed under isoflurane anesthesia and given tail vein catheters, which were loaded with 40 μL of heparinized saline followed by 110 μL of 0.25 M gadopentetate dimeglumine. Animals were kept under anesthesia during the entire acquisition.

The VIFs were measured in five mice, three of whom were imaged twice to produce a total of eight reproducibility measurements. Previous comparisons of the variability between mice and the variability between injections have found that the variability of the same mice on different days is the same as the variability across mice (63), which means that the reusing mice does not compromise the independence of the measurements on different days.

5.4 Data acquisition

5.4.1 Methods

After positioning the mouse in the scanner, three-plane localizers were acquired using a FLASH protocol to permit visualization of the heart. Acquisition parameters were: $TE = 1.6$ ms, $TR = 30$ ms, flip angle $= 5°$, matrix size $= 128\text{x}128$, FOV $= 6.4$ cm x 6.4 cm, slice thickness $= 1$ mm, number of averages $= 10$. Averaging allowed visualization of the heart without interference from motion artifacts. These images were used to position the cardiac and anatomic slices.

Before contrast injection, short axis images were acquired in the heart using a radial RF-spoiled gradient echo sequence. Acquisition parameters were: $TE = 1.55$ ms (fat and water in phase), $TR = 41$ ms, flip angle $= 30°$, slice thickness $= 1$ mm. The acquisition matrix was 256 points over 4 cm with 384 spokes and an angular increment of $120.5°$. This angle was used to disperse projections containing respiratory motion more evenly throughout the acquired angles than incrementing by $90°$. The resulting images were used to verify good visualization of the heart in the slice.

To account for variations in the preparation of the catheter, low volume (5-10 μL) injections were performed to clear the saline from the catheter, followed by the acquisition of another cardiac image. This was repeated until contrast enhancement was observed.

Afterwards, images were acquired at 15 minute intervals until the signal in the heart had returned to its baseline value. This guaranteed that the measurement of future injections would not be influenced by residual contrast agent.

Acquisition of the VIFs in the mice was performed using a spoiled gradient echo sequence. Acquisition parameters were: TE = 1.55 ms, TR = 41 ms, flip angle = 30º, slice thickness = 1 mm. One trans-cardiac slice was acquired using a radial acquisition scheme while seven slices were acquired with Cartesian encoding of the head and neck region. The acquisition matrix for the Cartesian encoded head and neck slices was 256x96 over a 4 cm x 3.84 cm FOV, providing one sample every 3.9 s. The acquisition matrix for the radial encoded cardiac slice was 256 points over 4 cm with 384 spokes and an angular increment of 120.5º. Duration was of the dynamic sequence was 30 repetitions of the radial protocol, corresponding to 120 repetitions of the Cartesian sequence. A 5 mm presaturation band was applied on each side of the trans-cardiac slice to suppress inflow enhancement during excitation using the RF pulse described in Chapter 3. A 10 μL injection of contrast agent was performed with an injection rate of 0.5 mL/min approximately 75 seconds after the start of the acquisition using a computer controlled injection system (Harvard Apparatus, Holliston, MA). After the dynamic acquisition was complete, images were acquired at 15 minute intervals to monitor the clearance of contrast agent. Once the signal in the left ventricle of the heart had returned to within 5% of its baseline value, indicating that the contrast agent had cleared from the blood, the dynamic protocol and injection were repeated. The injection protocol was performed three times per imaging session.

After data acquisition, VIFs were measured in the heart using the CACTUS analysis technique. Filtered backprojection was performed to generate anatomic images, from which manual anatomic segmentation was performed. This segmentation was used to produce a high

temporal resolution VIF measurement from the left ventricular signal. Further

details on the processing were provided in §4.11. In addition, VIFs were measured in the

conventionally encoded head and neck slices. The same vessel was used for measurements in

all three injections whenever possible. Voxels were manually selected that displayed

prominent signal enhancement and with minimal motion artifacts. All signal measurements

were converted into concentration as described in §2.2using assuming a baseline T_1 of 1800 ms

for blood and a contrast agent relaxivity of 4.8 $s^{-1}mM^{-1}$ for gadopentetate dimeglumine.

5.4.2 Results

Comparison of the VIFs measured with the proposed strategy to those from local blood

vessels reveals that the overall amplitude of the cardiac VIFs is greater. Five of the CACTUS

VIFs display periodic oscillatory artifacts; others display varying levels of noise. The

oscillations are possibly the result of segmentation errors, as suggested in §4.5, although this is

not possible to confirm. Relatively larger fluctuations are visible in the local vessel VIFs,

which result from motion artifacts and noise. Formal reproducibility analysis is presented in

§5.5.

5.5 Curve fitting and statistical analysis

5.5.1 Methods

To allow comparison of the reproducibility of the VIFs measured in the heart to a

conventional local vessel measurement, signal measurements were converted into

concentration(31), and the resulting concentration curves were fit to a biexponential model

$$C(t) = C_0 \left(\alpha e^{-k_{fast}t} + e^{-k_{slow}t} \right) \qquad \text{(Eq. 5.1)}$$

where C_0 is the amplitude of the slow component of the VIF, α is the relative

amplitude of the fast component, and k_{slow} and k_{fast} are the decay constants of the two VIF

components. Because partial volume and inflow effects tend to affect the entire input function

(58), they affect the amplitude of both terms in the model, as well variations in the injection

amplitude. To partially segregate these artifacts from differences in temporal resolution, the

amplitude of the fast component was defined in a relative manner. With this formulation, the

overall amplitude is most affected by partial volume and flow artifacts, and the relative fast

amplitude is most affected by the temporal resolution. This segregation is imperfect because

partial volume effects cause some distortion of the VIF (66). The model was fit to the decaying

portion of the model after the initial rise of the contrast agent using a Levenberg-Marquardt

algorithm (116) in Matlab. To minimize the difficulties associated with the sensitivity of

biexponential fits to initial parameter values in fitting, a stripping algorithm was used (117). In

this approach, the slow component is first estimate solely from the last half of the data, which

should be approximately monoexponential due to decay of the fast component. This term is

then subtracted from the data to produce a set of data which should only include the fast

component, which can also be calculated. These parameters are then used as initial values for

the non-linear fit to the entire model and the entire set of data.

For each mouse, the coefficient of variation of each parameter was calculated for VIF

measurements. The mean coefficients of variation for the biexponential parameters were

compared using the paired Hotelling T^2 test, which is the multivariate analogue of the paired t-

test (118). As additional figures of interest, the CV of the parameters means across subjects

was calculated from the mean parameter values from each mouse.

5.5.2 Results

The raw values for the biexponential model parameters for each technique are given in Table 5-1 and Table 5-2, and are plotted in graphical format in Figure 5-2.

		k_{fast} (1/min)	α	k_{slow} (1/min)	C (μmol)
Mouse 1	Injection 1	2.96	1.13	0.169	67
	Injection 2	4.50	0.77	0.138	52
	Injection 3	3.22	1.21	0.00	48
Mouse 2	Injection 1	2.93	1.62	0.090	65
	Injection 2	1.61	2.31	0.000	29
	Injection 3	1.35	1.13	0.079	49
Mouse 3	Injection 1	3.11	1.66	0.145	105
	Injection 2	2.42	1.82	0.076	96
	Injection 3	2.53	1.82	0.118	55
Mouse 4	Injection 1	2.49	2.32	0.162	52
	Injection 2	2.22	1.44	0.055	130
Mouse 5	Injection 1	0.66	2.04	0.013	116
	Injection 2	1.03	1.98	0.029	79
Mouse 6	Injection 1	0.93	3.54	0.000	61
	Injection 2	1.10	1.92	0.183	64
	Injection 3	0.53	1.34	0.139	53
Mouse 7	Injection 1	0.71	1.64	0.065	77
	Injection 2	0.49	1.28	0.083	79
Mouse 8	Injection 1	2.37	2.94	0.059	355
	Injection 2	2.60	2.03	0.225	38
	Injection 3	5.24	2.28	0.049	26

Table 5-1 VIF descriptive parameters from the heart using constrained reconstruction analysis.

		k_{fast} (1/min)	α	k_{slow} (1/min)	C (µmol)
Mouse 1	Injection 1	0.83	1.1864	0.154	21
	Injection 2	14.05	0.4236	0.291	25
	Injection 3	15.57	0.7590	0.010	32
Mouse 2	Injection 1	1.44	0.4616	0.056	50
	Injection 2	1.16	0.7590	0.018	18
	Injection 3	22.29	0.0000	0.169	33
Mouse 3	Injection 1	2.81	0.9659	0.146	53
	Injection 2	1.48	0.6980	0.068	45
	Injection 3	3.96	0.6717	0.075	31
Mouse 4	Injection 1	2.55	1.3365	0.130	53
	Injection 2	2.43	0.9201	0.043	72
Mouse 5	Injection 1	0.36	0.3240	0.049	99
	Injection 2	0.15	0.0929	0.153	36
Mouse 6	Injection 1	0.22	0.4868	0.216	80
	Injection 2	1.36	0.2295	0.161	71
	Injection 3	3.54	0.0000	0.085	42
Mouse 7	Injection 1	1.05	0.8379	0.047	34
	Injection 2	44.50	0.4067	0.72	39
Mouse 8	Injection 1	0.99	0.3410	0.022	329
	Injection 2	4.76	1.3436	0.120	33
	Injection 3	0.11	0.4439	1.429	14

Table 5-2 Measured VIF descriptive parameters from the cerebral vessels with conventional encoding.
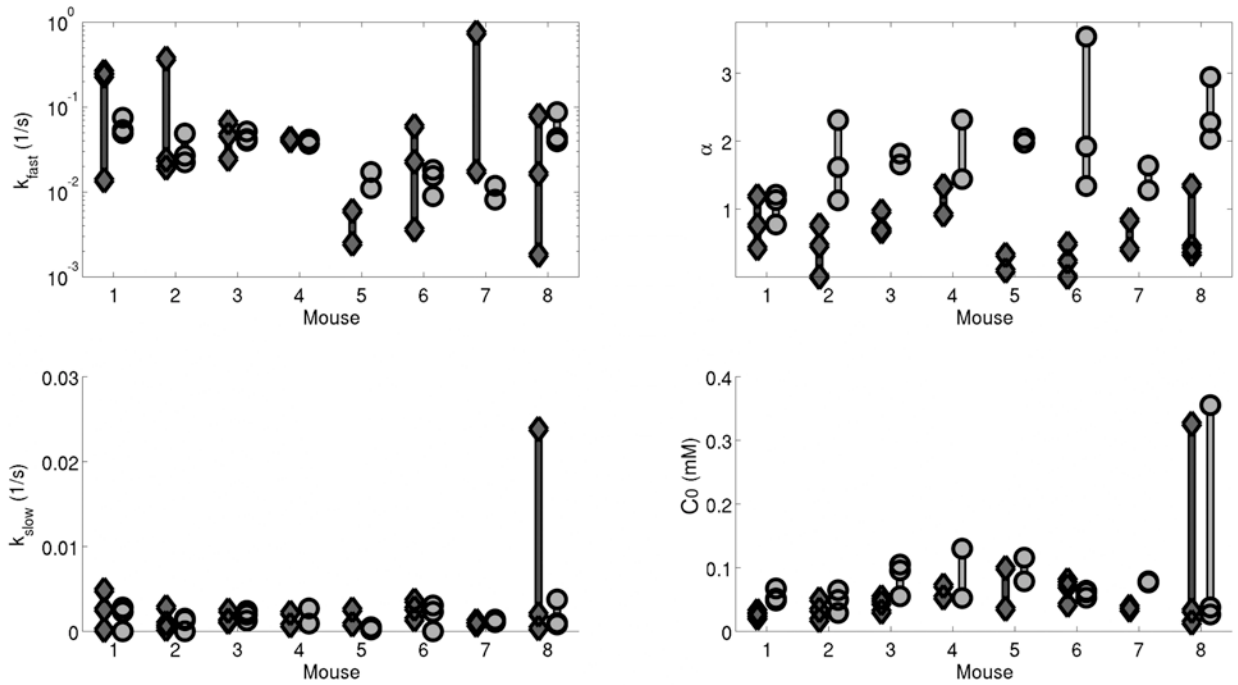
Figure 5-2 Measured VIF parameters for all mice and injections.

Tighter clustering is found in the estimates from constrained reconstruction in the heart (circles) than those made in local blood vessels using conventional encoding (diamonds), demonstrating the superior reproducibility of the cardiac sampling. These differences are most pronounced in comparisons of the fast component, which showed the most improvement in reproducibility of the four parameters.

	k_{fast}	α	k_{slow}	C_0
Mouse 1	23%	22%	88%	18%
Mouse 2	43%	35%	87%	38%
Mouse 3	14%	5%	31%	31%
Mouse 4	8%	33%	70%	60%
Mouse 5	31%	2%	52%	27%
Mouse 6	34%	50%	89%	10%
Mouse 7	26%	18%	17%	2%
Mouse 8	47%	20%	89%	133%

Table 5-3 Coefficients of variation of the parameters for the biexponential fits measured in the heart using CACTUS acquisition and analysis.

	k_{fast}	α	k_{slow}	C_0
Mouse 1	80%	48%	93%	20%
Mouse 2	146%	94%	97%	47%
Mouse 3	45%	21%	45%	26%
Mouse 4	4%	26%	71%	21%
Mouse 5	59%	78%	73%	67%
Mouse 6	99%	102%	43%	31%
Mouse 7	135%	49%	29%	9%
Mouse 8	127%	78%	151%	141%

Table 5-4 Coefficients of variation of the parameters for the biexponential fits measured in the cerebral vessels using conventional Fourier-encoded acquisition and processing.

	Mean Value (Local Vessel)	Mean Value (Heart)	Intrasubject CV (Local Vessel)	Intrasubject CV (Heart)	Intersubject CV (Local Vessel)	Intersubject CV (Heart)
k_{fast} min^{-1}	6.01	2.14	86%	28%	120%	58%
α	0.6042	1.82	62%	23%	51%	24%
k_{slow} min^{-1}	0.17	0.09	75%	65%	97%	38%
C_0 μmol	57	81	45%	40%	55%	36%

Table 5-5 Interanimal comparisons of the pharmacokinetic parameters.

The parameter values of the biexponential fits reveal a greater reproducibility, both within and between animals, of the VIFs measured in the heart using CACTUS compared to those measured in local vessels with conventional sampling. The biexponential parameters for all mice are shown graphically in Figure 5-2. The measured VIFs, and the fits, are shown in Figure 5-3 through Figure 5-10. The within-mouse reproducibility of injections was considerably improved ($p < 0.05$), with the CV of k_{fast} and α decreasing the most, from 86% to 28% and 62% to 23% in constrained and local vessels, respectively, while the changes in both k_{slow} and C_0 were a more modest 10% and 5%, respectively. The inter-subject variation was also decreased for the four parameters, again most prominently in the fast time constant, although the number of mice imaged was not sufficient to permit usable statistical comparisons.

Coefficients of variation for each mouse and each technique are given in Table 5-3

for cardiac sampling and Table 5-4 for left ventricular measurements, and overall results are

summarized in Table 5-6. These figures include both errors due to measurements and also true

changes in the blood dynamics due to variation in the injections and drift in the physiological

state of the mouse, however, a reduction in the variance may be attributed to a reduction in

measurement error because of the paired nature of the measurements and physiological drift

will be common to both techniques.

Quantitative differences in the VIFs measured with the two techniques were observed,

indicated by the mean biexponential parameters differing between conventional vessel

sampling and cardiac sampling with constrained analysis ($p < 0.05$). The mean concentration

measured in the heart was larger, which is consistent with a decrease in the presence of partial

volume and flow artifacts. The mean relative amplitude of the fast component was larger when

measured using constrained reconstruction in the heart, which is consistent with better

sampling of the peak, as was seen in both the proof-of-principle simulations and in the

comparison of FBP with the CR algorithm.
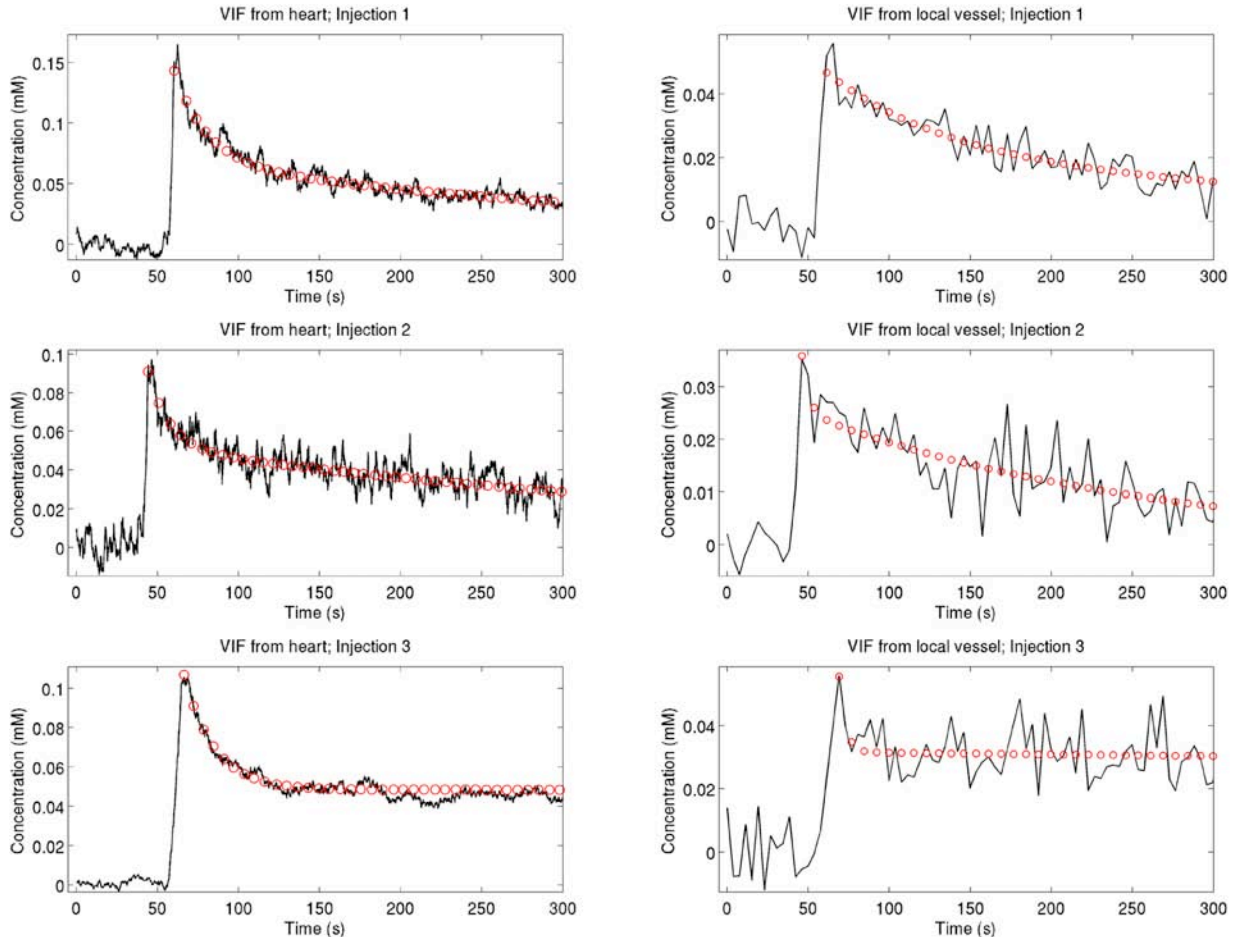
Figure 5-3 VIFs measured in mouse 1.

In these VIFs, the curves from the constrained cardiac measurement present considerably smaller signal fluctuations due to noise and motion. In the fits to the third local vessel VIF, the fit of the fast component is noticeably brief, consisting of only a single point, as evidenced by the very large decay constant for the curves.
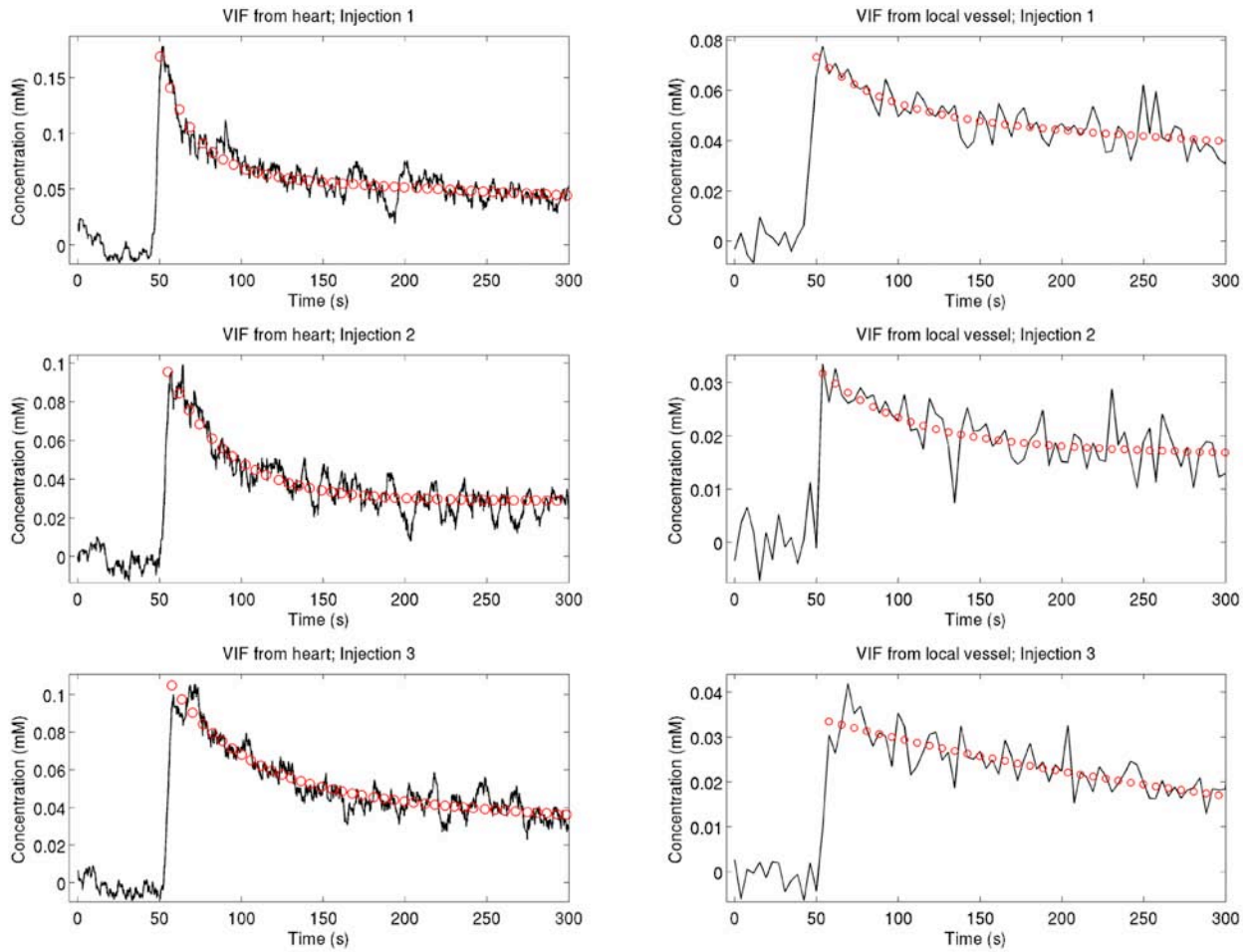
Figure 5-4 VIFs measured in mouse 2.

Motion is less problematic in the local vessel measurements in this mouse than in the previous, although a few large signal jumps are visible. For the first two injections, the initial peak of the VIF is noticeably more prominent in the cardiac measurements than in the vascular ones.
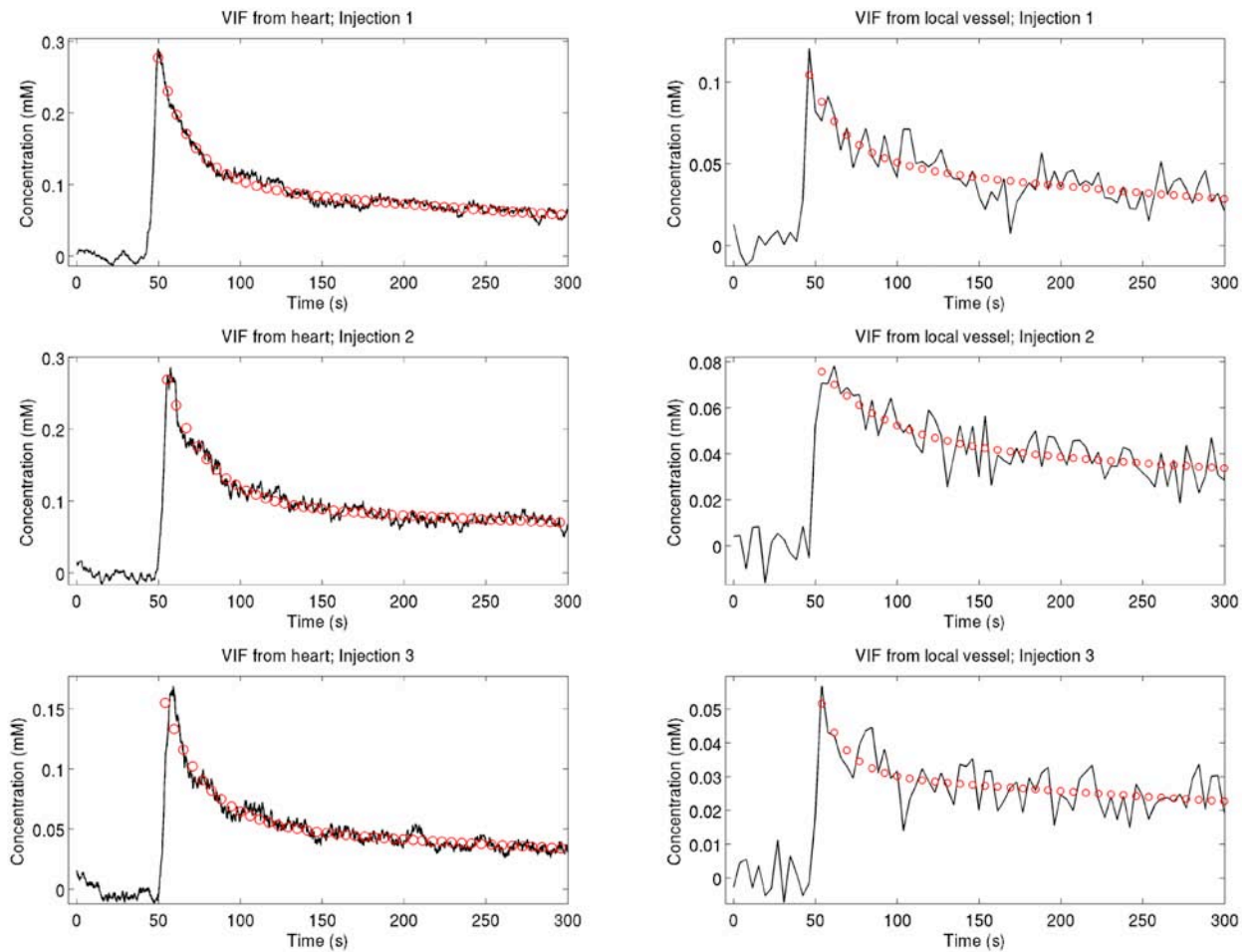
Figure 5-5 VIFs measured in mouse 3.

Many of the same comments that apply to the first mice apply to these curves. Of particular note is the second pair of measurements, where an initial peak of the contrast agent that is clearly seen in the cardiac measurement is not resolved in the vessel measurement. The second and third curves have secondary bumps which are consistent with recirculation, although they are less distinct than in the first mouse.
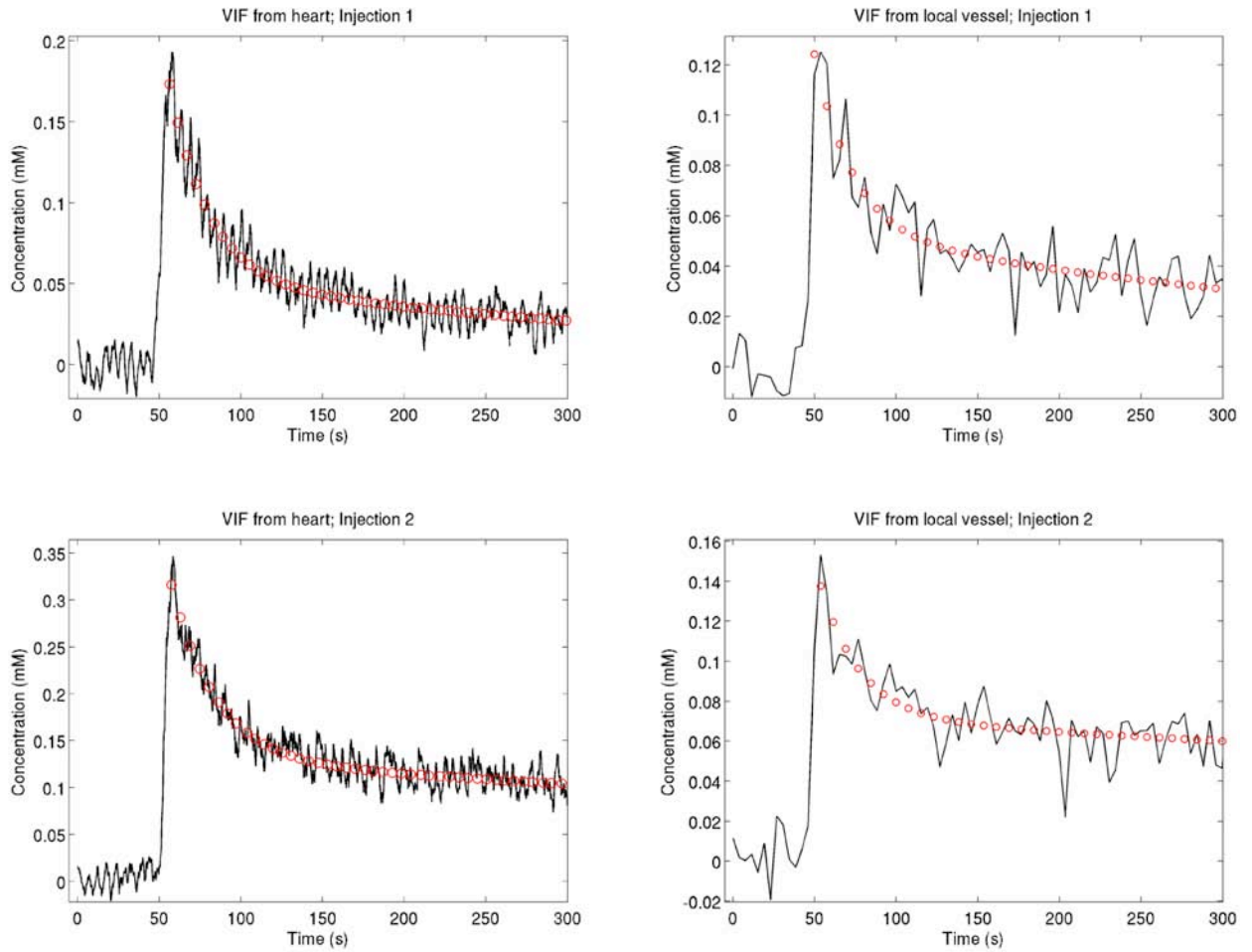
Figure 5-6 VIFs measured in mouse 4.

Only two measurements were performed in this mouse due to substantial motion during the third injection. Relatively large oscillations are found in the cardiac measurements, although the relative magnitude of these is less than the artifacts found in the local vessel measurements.
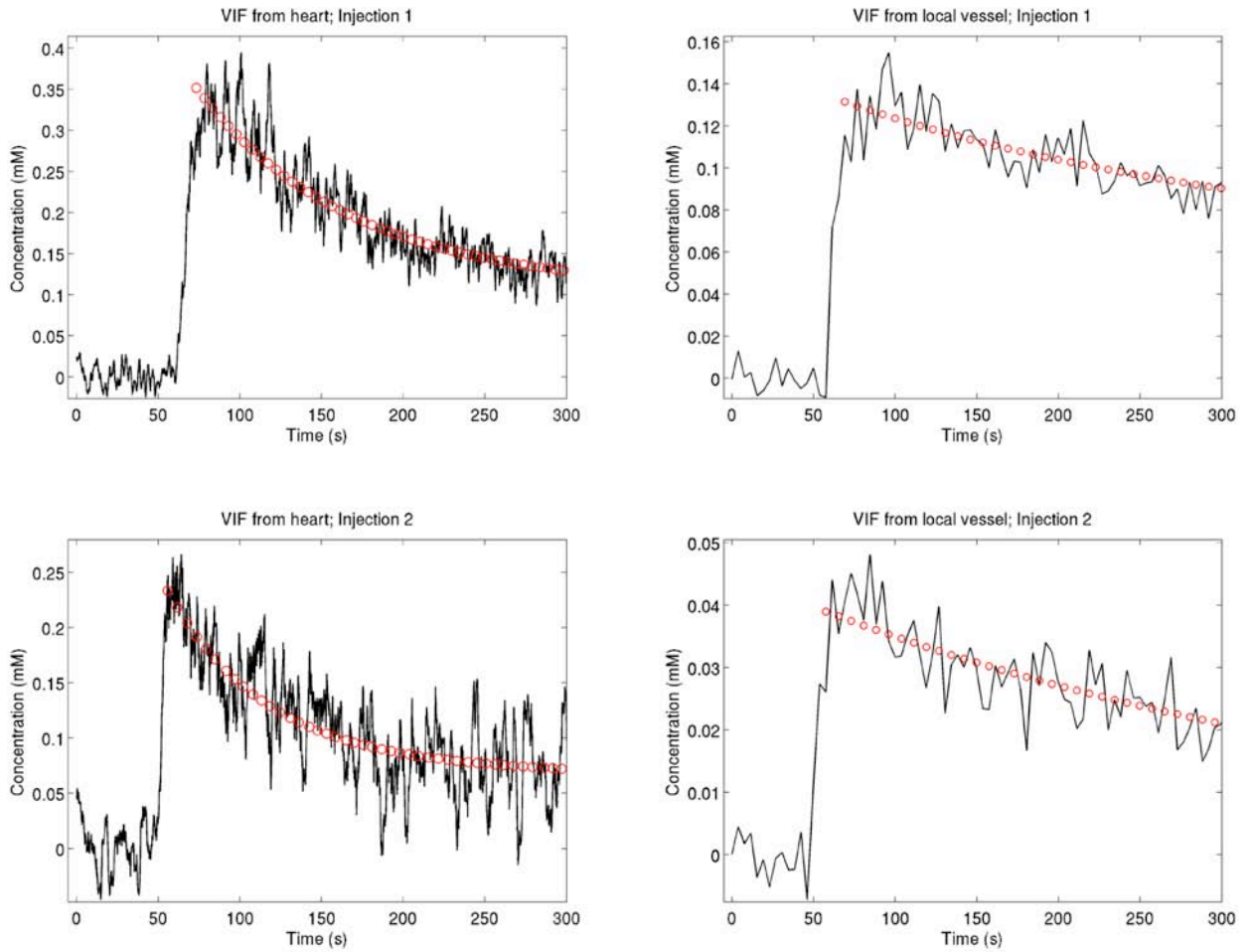
Figure 5-7 VIFs measured in mouse 5.

These VIFs demonstrate relatively large fluctuations and are fairly low in amplitude.

Neither technique provided extremely high quality measurements in this mouse.
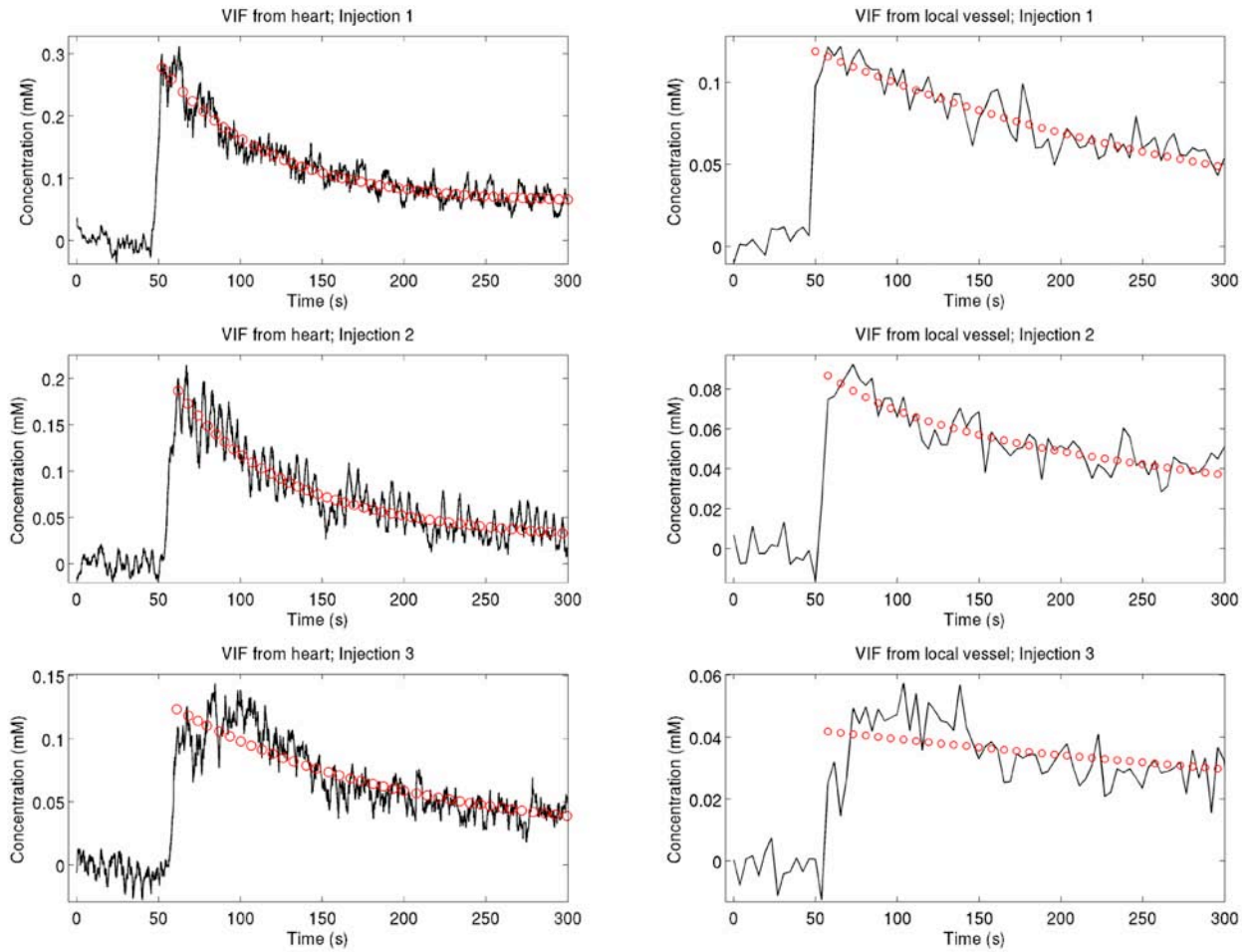
Figure 5-8 VIFs measured in mouse 6.

The VIFs measured with both techniques display unusually broad initial regions, which seems to widen with time. This may be due to drift in the physiology or some motion in the catheter placement. The overall slow dynamics of these uptake curves render the higher temporal resolution of the cardiac measurement less evident.
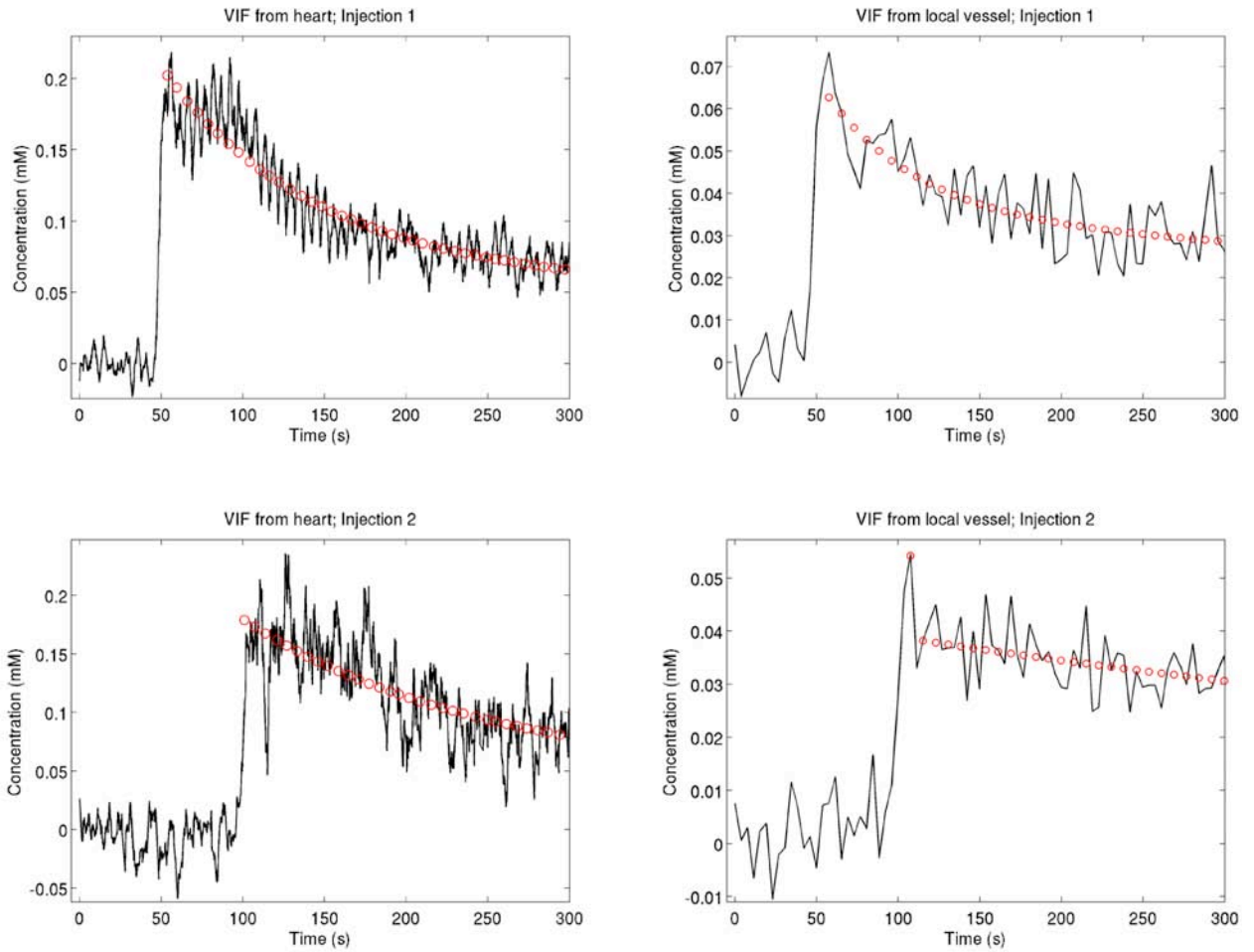
Figure 5-9 VIFs measured in mouse 7.

The cardiac measurement proved more reproducible in this mouse, despite fairly noisy

measured VIFs. In particular, in this mouse the fast decay constant shows the largest

improvement with the cardiac measurement of any mouse.
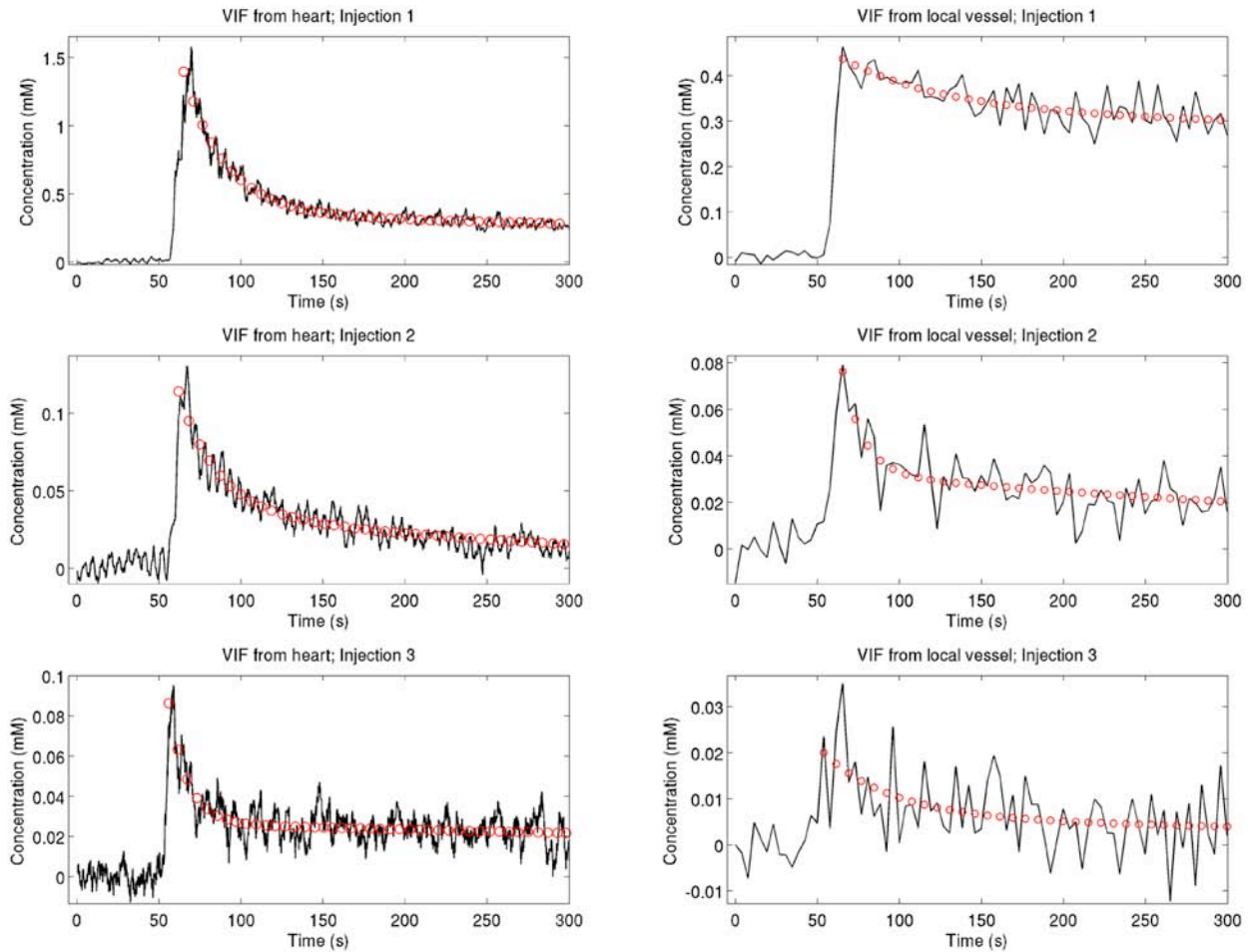
Figure 5-10 VIFs measured in mouse 8.

These uptake curves display unusually low relative amplitude slow phases. In the third injection, the oscillations in the local vessel curve are often larger than the concentration level itself, artifacts which are not found in the cardiac measurement. For both curves, the first injection is of larger amplitude than the last two. This appears to be a legitimate difference in the amount of contrast delivered due to substantial backwash of blood into the catheter after the first injection.

5.6 Comparison of different levels of low-pass filtering

5.6.1 Methods

Although the temporal resolution needed for VIF measurement in mice has not been established, the raw output of the constrained reconstruction is certainly sampled sufficiently rapidly to potentially satisfy any temporal resolution criteria for small animal DCE-MRI. However, model fitting is sensitive to problems with local minima that result from noise (119). Biexponential models, as will be used in this work, are known to be highly sensitive to this effect, with unreliable results reported even for SNR levels of 70 (120), although those results featured closer values of the two decay constants. To more reliably perform fits of *in vivo* data to models, filtration was performed as described in §4.11. However, the range of reasonable filtration choices is wide. Therefore, we performed a comparison of the reproducibility VIFs in one mouse with both a 1 s filter and a 0.6 s filter. The biexponential fitting and CV calculation was performed for the data from a single mouse.

5.6.2 Results

The two VIF signal curves agree closely (Figure 5-11), although the curve processed with greater filtration is smoother and shows a lower noise level. Except for the fast decay constant of the third injection, all parameter values agree to within 3%, and the coefficients of variation derived from these parameters are nearly identical. These results indicate that the measurement reproducibility in these mice does not depend strongly on the choice of the filter used. Parameter values and corresponding variations are given in Table 5-6.
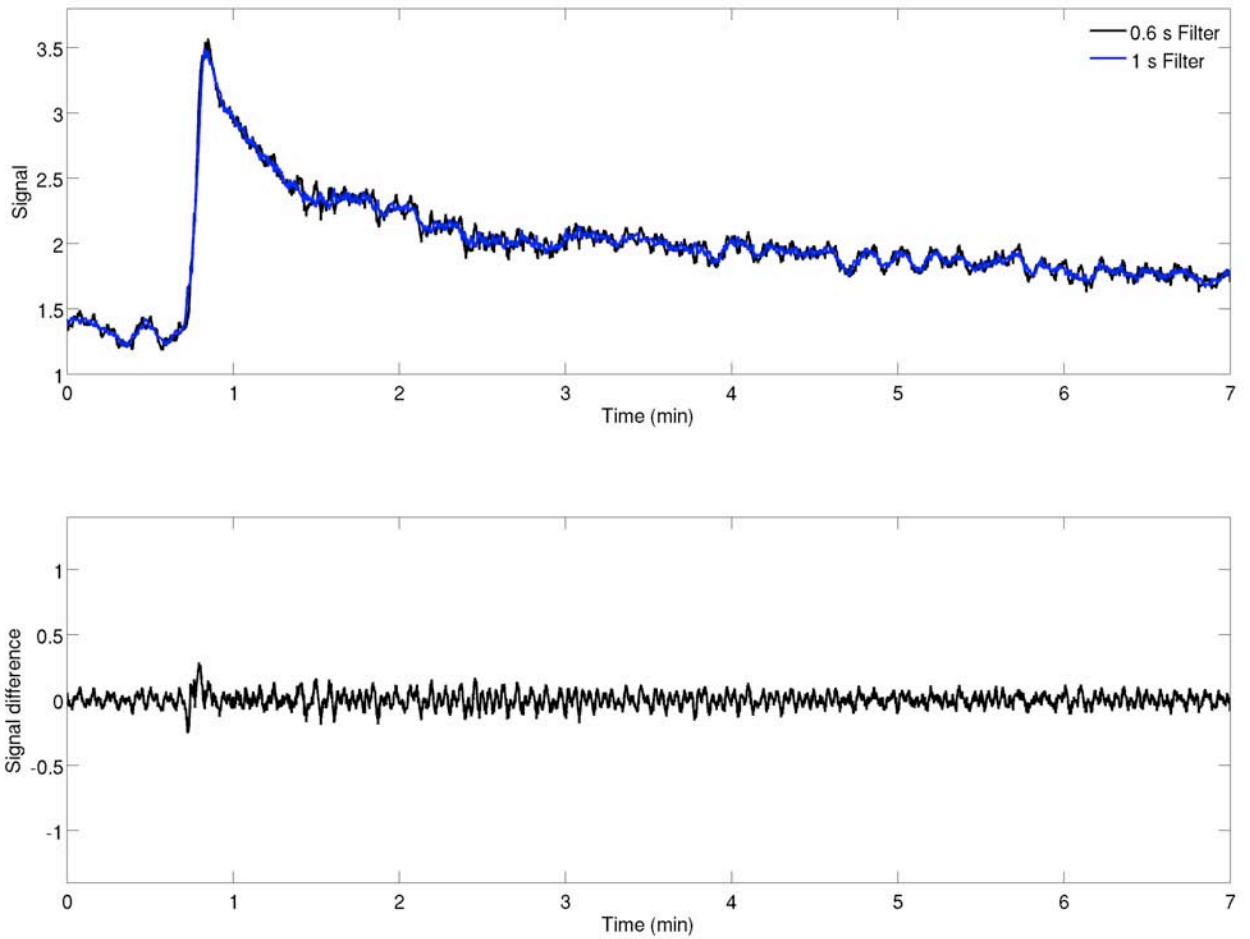
Figure 5-11 Comparison of a VIF measured with two different filter widths.

The curves generated by two different filter widths align quite closely (top), and only small fluctuations are seen in the difference curve (bottom).

		k_{fast} (1/min)	α	k_{slow} (1/min)	C (µmol)
0.6 s	Injection 1	3.21	1.70	0.147	105
	Injection 2	2.50	1.87	0.077	95
	Injection 3	2.75	1.86	0.119	56
1 s	Injection 1	3.11	1.66	0.145	105
	Injection 2	2.42	1.82	0.076	96
	Injection 3	2.53	1.82	0.118	55
CV	1s	13%	5%	31%	31%
	0.6 s	13%	5%	31%	30%

Table 5-6 Biexponential parameters calculated with two different filter widths applied.

5.7 Discussion

Robust and consistent VIF measurement is an outstanding challenge in small animal MRI. We have developed a strategy for reduced artifact acquisition of the VIF that relies upon measurement in the left ventricle, which provides resistance to partial volume effects and an improved signal to noise ratio due to its large size, and by using a constrained reconstruction approach, which provides high temporal resolution measurement of the VIF.

Our measurements of the VIF rise times indicate conventional encoding is not able to reliably measure the VIF dynamics in mice. The rise times were substantially wider than the width of the filter, indicating its effect on the measurement will be relatively slight.

Our measurements indicate a significant improvement in the within-mouse reproducibility of VIF measurement, as quantified by analyzing the variations in a biexponential representation of the VIF. The experimental setup was designed to maintain the

stability of the animal's physiology, ensuring that the variation in VIFs between injections is dominated by measurement effects and not by physiological drift. Although measurements were not performed of tumor enhancement, the VIF is an input into the parameter calculation and is known to strongly affect the resulting parameters(11,57). In addition, we observed both a reduction in the inter-animal variation and a significant change in the shapes of the VIFs compared to conventional vessel sampling.

6 Conclusions

6.1 Summary

This work consisted of three aims, with the objective of testing the hypothesis that rapidly sampled measurements of the VIF in the heart would produce more reproducible measurements than conventional local vessel sampling of the VIF. The first two aims involved the implementation and development of the technical components necessary to accomplish cardiac sampling of the VIF. The final aim was perform a comparison of the within-subject variation of VIF measurement using the newly developed and conventional techniques.

The first aim was concerned with the development of a novel RF pulse to mitigate the effects of flow enhancement on the VIF measurement. We considered two classes of pulses that combine spatial presaturation of flowing spins with excitation. One used a symmetric envelope of three sinc pulses; the other used an asymmetric envelope with a sinc pulse and a cosine-modulated sinc pulse. Phantom data showed that both families of pulses were able to reduce the signal of flowing water to its baseline level, however, simulations and measured data showed that the asymmetric pulse tended to produce an show fluctuations with the width of the sideband, rendering its suppression of out-of-slice signal suspect. For this reason, the symmetric pulse was determined to be preferable and was used in the remainder of the measurements in this body of work.

Our results also suggest that, while the use of this pulse is always able to increase the sensitivity of the MR signal to the presence of contrast agent, some residual flow enhancement in the case of straight-line flow may be present due to incomplete out-of-slice signal spoiling. This was indicated in simulations and measurements in the inferior vena cava. Suppression of flow enhancement in the left ventricle is less susceptible to this artifact because blood does not

follow a straight-line path in the thorax, the entirety of which can be covered by the presaturation region produced by the RF pulse. Blood enters the thorax through the vena cava and passes through the other three chambers of the heart and the lungs before arriving in the left ventricle. This both extends the effective width of the saturation region and prevents the signal bias from interfering with the measurement in the left ventricle.

Final measurements in the first aim demonstrate the that a VIF measured in the heart shows a much larger signal increase when measured with the composite pulse than with a sinc pulse with no additional flow suppression. Even in data sampled at low temporal resolution, the flow suppressed VIF showed more structure than the VIF acquired with conventional excitation. This both underscores the importance of flow enhancement suppression to VIF measurement and demonstrates the ability of this pulse to provide efficient flow suppression without sacrificing excessive time during the pulse sequence.

The second aim was devoted to the development of CACTUS, an anatomically constrained approach to data analysis which allows sampling of the signal from the left ventricle at extremely rapid rates. This technique relies upon the use of a manual segmentation to provide prior information that is used to reconstruct an approximate measure of the mean signal in each ROI.

Numerical simulations of the algorithms show that it is insensitive to random variations in the dynamics of the tissue. Non-random variations in the tissue dynamics, such as would result from segmentation errors, can produce artifacts, although these may be mitigated by the use of multiple projections. Phantom and *in vivo* measurements indicate accuracy to within 4% of the actual value in many cases when using a two projection protocol. The use of CACTUS was found to provide higher temporal resolution measurement of the VIF than full encoding, while capturing the low temporal resolution dynamics comparable to a full acquisition. This

technique was in fact able to identify the first pass of the contrast agent in mice, although recirculation of the contrast agent was not identifiable.

With these technical developments, we performed a reproducibility study of VIFs measured in small animal models. Measurements made with the techniques were compared to measurements made in blood vessels in the head and neck region using conventional sampling techniques. We found a statistically significant improvement ($p < 0.05$) in the intra-subject reproducibility, with the CV of model parameters decreasing by up to 56%. We also observed an improvement in the inter-subject reproducibility, although we did not image a sufficient number of mice to perform rigorous statistical comparisons.

6.2 Hypothesis

Our *in vivo* comparisons found a statistically significant reduction in the coefficients of variation of the biexponential parameters of VIFs measured using the techniques described here as compared to measurements in a local blood vessel. We also achieved sub-second temporal resolution of the measurement. Based on these two points, we find that that hypothesis is supported by the data.

6.3 Limitations and Future work

The comparison of VIF reproducibility was between measurements made in the heart with the developed techniques and measurements made with a conventional vessel measurement. Only a limited number of voxels were used in the measurements of the local vessel VIFs, which is a contributor to the noise of these measurements, although this is in part due to the greater volume of blood available in the heart for VIF measurement and in part a reflection of the difficulty in finding blood vessels that had similar VIF amplitudes and whose time courses were not offset in time. The reliability of the local vessel measurements could

have been improved by the use of dedicated flow suppression techniques to minimize inflow artifacts in those measurements, however, an objective of this work was to measure VIFs without the compromise in slice coverage that would be required. This rendered truly paired results impossible. Additionally, we found a substantial attenuation of inflow enhancement in local vessels due to residual saturation from the spin preparation in the thorax. For these reasons, the overall conclusion that a substantial improvement in VIF measurement is achieved with this technique is still valid.

Our technique provided considerably more reproducible measurements of the VIF than conventional measurements. Although it is expected that these techniques should lead to an improvement in the measurement of pharmacokinetic parameters, this was not directly demonstrated. *In vivo* testing with a tumor model would provide additional characterization of the technique and a more direct indication of the extent to which it improves upon existing techniques. However, those measurements are outside the scope of this work.

Further improvements to the technique are also possible. Because of the decreased signal from the ventricles, conventional filters for approaches to retrospective cardiac gating were not able to reduce the signal fluctuations due to cardiac motion. We reduced cardiac motion artifacts with a low pass filter, however, this decreased our temporal resolution. More intelligent denoising approaches, such as a Wiener filter (121) or wavelet-based approaches (122) may be more suitable this application.

The techniques used in this work allow the potential for very high temporal resolution. However, there is no established rate at which the temporal resolution of VIF measurement for use in pharmacokinetic parameter calculation in mice is optimized. Simulations should be performed to establish a required sampling rate for a given accuracy of the final parameters, as has been done in humans (56).

This work used the same acquisition protocols for both the tissue slices and the cardiac slice using interleaved encoding schemes, except for the *k*-space trajectory. However, the contrast agent concentrations reach higher peak levels in blood than they do in tissue, resulting in shorter relaxation times. As a result, larger flip angles are needed for optimal imaging of contrast agent concentrations in the blood than are needed for tissue (31). Because a separate slice is used for VIF measurement with the approach implemented here, the use of a different excitation angle for each is easily achieved, and consideration of these effects may lead to further improvements in VIF measurement.

6.4 Conclusions

We have developed a set of tools to address what has been called "a notoriously difficult problem" (71). Artifacts, such as inflow enhancement and partial volume effects, as well as limitations in the achievable temporal resolution, compromise the integrity of the VIFs used in small animal DCE-MRI studies. The techniques developed in this work have shown that they are capable of producing more reproducible measurements of the vascular input function, which will lead to more reliable and robust measurements of DCE-MRI pharmacokinetic parameters.

Appendix: Matlab reconstruction code

```matlab
function getAIFheart(varargin)

%% Front matter
%Here are the parameters this function uses:
grouping = 2; %Number of projections to use per constrained time point
              %It needs to divide the number of spokes
liverind = 4; %ROI position of the liver; should be 4
respthresh = .3; %Percentage of points to discard for respiratory triggering
order = 0;  %Order of the Taylor polynomial

%% Identify the directory to process
if nargin==0
    dirname = uigetdir;
else
    dirname = varargin{1};
    if isnumeric(dirname)
        dirname = num2str(dirname);
    end
end

%% Read in and reconstruct filtered backprojection images
tic
fbpname = fullfile(dirname, 'fbp.mat');
if exist(fbpname)
    load(fbpname, 'this');
else
    this = readHybridData(dirname);
    save(fbpname, 'this');
end
toc
% a=questdlg('Continue to segmentation?');
% if ~(a(1)=='Y')
%     return
% end

%% Perform manual segmentation
roisname = fullfile(dirname, 'rois.mat');
if exist(roisname)
    load(roisname, 'rois');
else
    %Choose the image with the greatest overall increase in image intensity
    temp = abs(squeeze(sum(sum(this.radimg, 1), 2)));
    gradient(2:length(temp)) = temp(2:end)-temp(1:end-1);
    argpeak = find(gradient==max(gradient));
    rois = guidedManualSegmentation(sum(this.radimg, 3));
%     rois = guidedManualSegmentation(abs(this.radimg(:, :, argpeak)));
    save(roisname, 'rois');
end

%% Expand ROIs
tic
%Expand ROI 1
radius = 1;
```

```matlab
old1 = rois(:, :, 1);
expansion = rois(:, :, 1);
contraction = ~rois(:, :, 1);
for ind = radius:-1:1
    contraction(2:end-1, :, 1) = contraction(2:end-1, :, 1) |
contraction(1:end-2, :, 1) | contraction(3:end, :, 1);
    contraction(:, 2:end-1, 1) = contraction(:, 2:end-1, 1) | contraction(:,
1:end-2, 1) | contraction(:, 3:end, 1);
end
contraction = ~contraction;
rois(:, :, 1) = contraction;
rois(:, :, 11) = expansion&~contraction;

for ind = 2:10
    rois(:, :, ind) = rois(:, :, ind)&~rois(:, :, 11);
end

%% Raw constrained reconstruction
[Nfreq Ntheta Nframe] = size(this.proj);
Nrois = size(rois, 3);
Ngroups = Ntheta/grouping;
Npoints = Nframe*Ngroups;
this.theta = reshape(this.theta, Ntheta, Nframe);
indices = reshape(1:Ntheta, grouping, Ngroups);

%For the Taylor expansion version
nterms = (order+2)*(order+1)/2;
[x, y] = ndgrid(linspace(-1, 1, size(rois, 1)), linspace(-1, 1, size(rois,
2)));

n = nterms;
for indO = order:-1:0
    for indP = indO+1:-1:1
        geom(:, :, n) = x.^(indP-1).*y.^(indO-indP+1);
        n = n-1;
    end
end



for ind = Nframe:-1:1
    refimg = this.radimg(:, :, ind);
    A = dPrepareConstrainedRecoTaylor(this.theta(:, ind), rois, (refimg));

%    A2 = dPrepareConstrainedReco(this.theta(:, ind), rois, refimg2);
    support = dPrepareConstrainedReco(this.theta(:, ind), any(rois, 3),
ones(size(refimg)))>0;
    support = reshape(support, size(support, 1)*grouping, Ngroups);
    heartros = dPrepareConstrainedReco(this.theta(:, ind), any(rois(:, :,
1:3), 3), ones(size(refimg)))>0;
%    A = reshape(A, Nfreq, Nrois, grouping, Ngroups);
    projections = reshape(this.proj(:, :, ind), Nfreq, grouping, Ngroups);
    offset = (size(A, 1)-size(projections, 1))/2;
    projections = cat(1, zeros(floor(offset), grouping, Ngroups),
projections, zeros(ceil(offset), grouping, Ngroups));
    for ind2 = Ngroups:-1:1
```

```matlab
        [tempz(:, :, ind2) condsigs(:, ind2, ind) res(:, ind2,
ind)] = dPerformConstrainedReconTaylor((projections(:, :, ind2)), A,
indices(:, ind2), [], rois, refimg);
    end
    thisimg = this.radimg(:, :, ind);
    res(:, :, ind) = res(:, :, ind).*support;
    ravg(:, ind) = mean(abs(res(:, :, ind)))./mean(support);
    heartros = reshape(heartros, size(projections));
    heartsig(:, :, :, ind) = projections.*heartros;
    heartres(:, :, ind) = res(:, :, ind).*reshape(heartros, size(res, 1),
size(res, 2));
    for ind2 = Nrois:-1:1
        fbpsigs(ind2, ind) = mean(thisimg(rois(:, :, ind2)));
    end
end
condsigs = reshape(condsigs, Nrois, Npoints);
condsigs(isnan(condsigs))=0;


cutoffind = round(respthresh*Ngroups);


liverpresent = any(any(rois(:, :, liverind), 1), 2);
if liverpresent
    liversigs = reshape(condsigs(liverind, :), Ngroups, Nframe);
    for ind = Nframe:-1:1
        fastliver = abs(liversigs(:, ind))-abs(fbpsigs(liverind, ind));
        temp = sort(fastliver);
        threshold = temp(cutoffind);
        respgate(:, ind) = fastliver>threshold;
    end
else
    respgate = true(Ngroups, Nframe);
end
respgate = respgate(:);
for ind = 2:length(respgate)-1
    if respgate(ind-1)&respgate(ind+1)
        respgate(ind) = true;
    end
end
for ind = 2:length(respgate)-1
    if ~respgate(ind-1)&~respgate(ind+1)
        respgate(ind) = false;
    end
end

%% Perform despiking



%% Perform cardiac triggering

% respgate(:) = true;

heartsig = reshape((sum(heartsig, 1))./sum(abs(heartsig)>1, 1), grouping,
Ngroups, Nframe);
tempgate = repmat(respgate, [1 grouping])';
tempgate = reshape(tempgate, grouping, Ngroups, Nframe);
```

```matlab
for ind = Nframe:-1:1
    temp = heartsig(:, :, ind);
    temp = temp(tempgate(:, :, ind));
    timedrift(1, ind) = mean(angle(temp));
end

heartsig = reshape(heartsig, Ntheta, Nframe);
tempgate = reshape(tempgate, Ntheta, Nframe);
for ind = Ntheta:-1:1
    temp = heartsig(ind, :);
    temp = temp(tempgate(ind, :));
    spacedrift(ind, 1) = mean(angle(temp));
end

heartphase = angle(heartsig)-repmat(timedrift, [Ntheta 1])-
repmat(spacedrift, [1 Nframe]);
heartphase = heartphase-mean(heartphase(tempgate(:)));
temp = heartphase(:);
threshold = std(temp(tempgate(:)))/2;
cgate = abs(heartphase)<threshold;
cardiacgate = all(reshape(cgate, grouping, []), 1)';

%% Perform residual gating

% ravg = reshape(mean(abs(res), 1), [], 1);
% rgate = false(size(ravg));
% rgate(2:end-1) = (ravg(2:end-1)<ravg(1:end-2)) & (ravg(2:end-
1)<ravg(3:end));

%% Filter

%Create a list of filterwidths
duration = Ntheta*Nframe*this.method.PVM_RepetitionTime/1000/60; %in minutes
tslow = linspace(0, duration, Nframe);
tfast = linspace(0, duration, Npoints);
fbpvif = abs(fbpsigs(1, :));
lvslow = interp1(tslow, fbpvif, tfast);

weights = (lvslow/min(lvslow(:))).^1;
% lvslow = lvslow-min(lvslow(:));

% for ind = Npoints:-1:1
%     percentile(ind) = sum(lvslow(ind)>lvslow)/Npoints;
% end
% weights = (log(100*percentile+exp(3))-2).^1.5;
%
% %Alternate approach
% weights = 4*lvslow/max(lvslow(:))+1;


lvsig = condsigs(1, :);
rvsig = condsigs(3, :);
filteredsig = zeros(size(lvsig));
windowwidth = 24/grouping;

%Hack to disable respgating
% respgate(:) = true;
```

```matlab
% windowwidth = 1;
weights(:) = 1;
for ind = Npoints:-1:1
    if respgate(ind)
        thiswidth = round(windowwidth/weights(ind));
        imax = min(Npoints, ind+thiswidth);
        imin = max(1, ind-thiswidth);
        localgate = respgate(imin:imax);
        localsigs = lvsig(imin:imax);
        filteredsig(ind) = mean(localsigs(localgate));
        localrsigs = rvsig(imin:imax);
        rvfilt(ind) = mean(localrsigs(localgate));
        tw(ind) = thiswidth;
    end
end

plot(tfast(respgate), abs(filteredsig(respgate)), tslow, fbpvif)

vifname = fullfile(dirname, 'heartvif.mat');
save(vifname, 'condsigs', 'filteredsig', 'tfast', 'tslow', 'fbpvif',
'respgate', 'res', 'heartsig', 'ravg', 'heartres', 'heartphase', 'rvfilt',
'rois');
toc
```

```matlab
function this = readHybridData(indir)

this = readBrukerDirectory(indir);
Nx = this.method.PVM_Matrix(1);
Ny = this.method.PVM_Matrix(2);
Ntheta = this.method.nTheta;
Nreps = this.method.PVM_NRepetitions;
deltatheta = this.method.loopskip;
Nslices = this.method.PVM_SPackArrNSlices(1); %Number of Cartesian slices
this.fid = reshape(this.fid, Nx, Nslices+1, Ny, Nreps); %For now, just
assume that there is only one radial slice
this.fid = permute(this.fid, [1 3 2 4]);
this.radfid = squeeze(this.fid(:, :, end, :));

n = Ny*Nreps;
thetaind = mod((0:(n-1))*deltatheta, Ntheta)+1;
theta = (thetaind-1)*180/Ntheta;
if isfield(this.method, 'cover')
    if strncmp(this.method.cover, 'Full', 4)
        theta(2:2:end) = theta(2:2:end)+180;
%        this.fid(:, 2:2:end, :, :) = this.fid(end:-1:1, 2:2:end, :, :);
    end
end
nRadImg = floor(Ny*Nreps/Ntheta); %Number of fully encoded radial images
fid = this.radfid;
proj = fftshift(ifft(ifftshift(fid), [], 1));
ptemp = mean(mean(proj, 2), 3);
ptemp = exp(i*angle(ptemp));
proj = proj./repmat(ptemp, [1 Ny Nreps]);
proj = reshape(proj, Nx, []);
proj = proj(:, 1:(Ntheta*nRadImg));
proj = reshape(proj, Nx, Ntheta, nRadImg);

proj = reshape(proj, Nx, Ntheta, nRadImg);
for ind = nRadImg:-1:1
    tind = Ntheta*(ind-1)+(1:Ntheta);
    cimg(:, :, ind) = iradon(real(proj(:, :, ind)), theta(tind), 'Ram-Lak',
'Linear', 1, Nx) + ...
        i*iradon(imag(proj(:, :, ind)), theta(tind), 'Ram-Lak', 'Linear', 1,
Nx);
%    cimg(:, :, ind) = iradon(abs(proj(:, :, ind)), theta(tind), 'Ram-Lak',
'Linear', 1, Nx);

end

this.proj = proj;
this.theta = theta;
this.thetaind = thetaind;
this.radimg = cimg;

%% Deal with body images
fid = this.fid(:, :, 1:end-1, :);
img = fftshift(fftshift(ifft2(ifftshift(ifftshift(fid, 1), 2)), 1), 2);
this.img = img;
```

```matlab
function output = readBrukerDirectory(directory, varargin)

if nargin == 0
    directory = uigetdir('/~', 'Directory for Dixon data');
end
if(directory(end)~='/')
    directory = [directory '/'];
end

output.acqp = readBrukerHeader([directory 'acqp']);
output.method = readBrukerHeader([directory 'method']);
output.fid = readBrukerFID(directory, output.method);
output.subject = readBrukerHeader([directory '../subject']);
```

```matlab
function struct = readBrukerHeader(filename)

fid = fopen(filename, 'r', 'l');

if (fid==-1)
    error('File not found in readBrukerHeader');
end


rawitems = textscan(fid, '%s', 'Delimiter', '\n');
fclose(fid);
rawitems = rawitems{1};

% rawdata = fread(fid, Inf, 'char=>char')';
%
% fclose(fid);
%
% temp = rawdata;
% index = 1;
%
% while ~isempty(temp)
%     [thisstring temp] = strtok(temp, sprintf('\n'));
%     if(strncmp(thisstring(end:-1:1), '$$', 2))
%         thisstring = thisstring(1:end-2);
%     end
%     rawitems{index} = thisstring;
%     index = index+1;
% end

index = 1;

while index<=length(rawitems)
    offset = 0;
    thisstring = rawitems{index};
    %The next line is a hack.  I'm okay with that.
    %Account for comment lines and other special cases
    if(strncmp(thisstring, '$$ @vis', 7))
        index = index + 1;
        continue
    end
    if(strncmp(thisstring, '##END=', 6))
        break
    end
    %Test that we're on a variable definition lines
    if(strncmp(thisstring, '##', 2))
        [name value] = strtok(thisstring, '=');
        %Trim off special characters
        name = name(3:end);
        if(name(1)=='$')
            name = name(2:end);
        end
        if ~isvarname(name)
            name = genvarname(name);
        end
        value = value(2:end);

        %Here's the case of just one item
```

```matlab
        if(~any(value=='('))
            num = str2num(value);
            if ~isempty(num)
                struct.(name) = num;
            else
                struct.(name) = value;
            end
            index = index+1;
            continue
        end

        %Now, consider the case of a string
        if(rawitems{index+1}(1)=='<')
            struct.(name) = rawitems{index+1}(2:end-1);
            index = index + 1;
            continue
        end

        %Check for an array
        if(strncmp(value, '( ', 2))
            array_is_numeric = true;
            %Parse the dimension description
            size = str2num(value(3:end-1));
            if(isscalar(size))
                size = [1 size];
            end
            n = prod(size);
            offset = 1;
            data = [];
            while (rawitems{index+offset}(1)~='#') &&
(rawitems{index+offset}(1)~='$')
                data = [data rawitems{index+offset}];
                offset = offset+1;
            end
            for index2 = 1:n
                [temptemp, data] = strtok(data);
                if(strncmp(temptemp((end-1):-1:1), '$$', 2))
                    temptemp = temptemp(1:end-2);
                end
                num = str2num(temptemp);
                if isempty(num)
                    array{index2} = temptemp;
                    array_is_numeric = false;
                else
                    array{index2} = num;
                end
            end
            if(array_is_numeric)
                array = cell2mat(array);
            end
            array = reshape(array, size);
            if n==1 && iscell(array)
                array = array{1};
            end
            struct.(name) = array;
            clear array
            index = index + offset;
            continue
```

```matlab
        end

        %Check for a cell array analogue
        if(strncmp(value, '(', 1))
            data = value(2:end);
            while ~any(data==')')
                offset = offset+1;
                data = [data rawitems{index+offset}];
            end
            data = data(1:end-1);
            index = index + offset;
            struct.(name) = data;
        end

        %Lastly, handle XYPOINTS
        if(strcmp(name, 'XYPOINTS'))
            offset = 1;
            ok = 1;
            while(ok)
                [data ok] = str2num(rawitems{index+offset});
                if(ok)
                    struct.XYPOINTS(offset, 1:2) = data;
                end
                offset = offset + 1;
            end
            index = index + offset;
        end
    end
    index = index+1;
end
```

```matlab
function fid = readBrukerFID(directory, varargin)


filename = fullfile(directory, 'fid');

fileid = fopen(filename, 'r', 'l');
fid = fread(fileid, Inf, 'int32');
fclose(fileid);

fid = fid(1:2:end) + i*fid(2:2:end);
```

```matlab
function rois = guidedManualSegmentation(refimg)

s.Default = 'Ok';
s.Interpreter = 'tex';


lv = false(size(refimg));
lvmyo = false(size(refimg));
heart = false(size(refimg));
vess = false(size(refimg));
portalvess = false(size(refimg));
allliver = false(size(refimg));
chest = false(size(refimg));
muscle = false(size(refimg));
body = false(size(refimg));
waterbed = false(size(refimg));


refimg = abs(refimg)/max(abs(refimg(:)));

answer = questdlg('Please contour the \bf{left ventricle}', 'Contouring',
'Ok', 'Not Present', 'Stop Now', s);
n = parse(answer);
if n == 0
    lv = roipoly(refimg);
    close(gcf);
elseif n == 2
    rois = stackROIs(lv, lvmyo, heart, vess, portalvess, allliver, chest,
muscle, body, waterbed);
    return
end

answer = questdlg('Please contour the \bf{outside of the myocardium}',
'Contouring', 'Ok', 'Not Present', 'Stop Now', s);
n = parse(answer);
if n == 0
    lvmyo = roipoly(refimg);
    close(gcf);
elseif n == 2
    rois = stackROIs(lv, lvmyo, heart, vess, portalvess, allliver, chest,
muscle, body, waterbed);
    return
end

answer = questdlg('Please contour the \bf{entire heart}', 'Contouring',
'Ok', 'Not Present', 'Stop Now', s);
n = parse(answer);
if n == 0
    heart = roipoly(refimg);
    close(gcf);
elseif n == 2
    rois = lv;
    return
end

answer = questdlg('Please contour any \bf{great vessels} present',
'Contouring', 'Ok', 'Not Present', 'Stop Now', s);
n = parse(answer);
if n == 0
```

```matlab
    vess = roipoly(refimg);
    close(gcf);
elseif n == 2
    rois = stackROIs(lv, lvmyo, heart, vess, portalvess, allliver, chest,
muscle, body, waterbed);
    return
end

answer = questdlg('Please contour any \bf{liver vessels} present',
'Contouring', 'Ok', 'Not Present', 'Stop Now', s);
n = parse(answer);
if n == 0
    portalvess = roipoly(refimg);
    close(gcf);
elseif n == 2
    rois = stackROIs(lv, lvmyo, heart, vess, portalvess, allliver, chest,
muscle, body, waterbed);
    return
end

answer = questdlg('Please contour the \bf{liver}', 'Contouring', 'Ok', 'Not
Present', 'Stop Now', s);
n = parse(answer);
if n == 0
    allliver = roipoly(refimg);
    close(gcf);
elseif n == 2
    rois = stackROIs(lv, lvmyo, heart, vess, portalvess, allliver, chest,
muscle, body, waterbed);
    return
end

answer = questdlg('Please contour the \bf{chest cavity}', 'Contouring',
'Ok', 'Not Present', 'Stop Now', s);
n = parse(answer);
if n == 0
    chest = roipoly(refimg);
    close(gcf);
elseif n == 2
    rois = stackROIs(lv, lvmyo, heart, vess, portalvess, allliver, chest,
muscle, body, waterbed);
    return
end

answer = questdlg('Please contour the \bf{body without fat layer}',
'Contouring', 'Ok', 'Not Present', 'Stop Now', s);
n = parse(answer);
if n == 0
    muscle = roipoly(refimg);
    close(gcf);
elseif n == 2
    rois = stackROIs(lv, lvmyo, heart, vess, portalvess, allliver, chest,
muscle, body, waterbed);
    return
end

answer = questdlg('Please contour the \bf{entire body}', 'Contouring', 'Ok',
'Not Present', 'Stop Now', s);
```

```matlab
n = parse(answer);
if n == 0
    body = roipoly(refimg);
    close(gcf);
elseif n == 2
    rois = stackROIs(lv, lvmyo, heart, vess, portalvess, allliver, chest,
muscle, body, waterbed);
    return
end

answer = questdlg('Please contour the \bf{waterbeds}', 'Contouring', 'Ok',
'Not Present', 'Stop Now', s);
n = parse(answer);
if n == 0
    waterbed = roipoly(refimg);
    close(gcf);
end

rois = stackROIs(lv, lvmyo, heart, vess, portalvess, allliver, chest,
muscle, body, waterbed);

end

function n = parse(answer)
switch answer
    case 'Ok'
        n = 0;
    case 'Not Present'
        n = 1;
    case 'Stop Now'
        n = 2;
end
end

function rois = stackROIs(lv, lvmyo, heart, vess, portalvess, allliver,
chest, muscle, body, waterbed)
myo = lvmyo&~lv;
rv = heart&~(lv|lvmyo);
liver = allliver&~portalvess;
lungs = chest&~(lv|lvmyo|heart|vess|portalvess|allliver);
muscle = muscle&~(lv|lvmyo|heart|vess|portalvess|allliver|chest);
body = body&~(lv|lvmyo|heart|vess|portalvess|allliver|chest|body);
waterbed =waterbed&~body;
rois(:, :, 1) = lv;
rois(:, :, 2) = myo;
rois(:, :, 3) = rv;
rois(:, :, 4) = liver;
rois(:, :, 5) = vess;
rois(:, :, 6) = portalvess;
rois(:, :, 7) = muscle;
rois(:, :, 8) = body;
rois(:, :, 9) = waterbed;
rois(:, :, 10) = lungs;
end
```

```matlab
function [weights] = dPrepareConstrainedRecoTaylor(theta, segments, img0, varargin)
%dPrepareConstrainedReco(theta, segments, img0, varargin)

%Flags is true if we are going to assume a constant value over the ROI

%First determine what format the rois are in...
if ~islogical(segments)
    %Convert indices into ROIs
    els = unique(segments(:));
    for ind = length(els):-1:1
        rois(:, :, ind) = segments==els(ind);
    end
else
    rois = segments;
end

order = 0;
nterms = (order+2)*(order+1)/2;

if nargin==3
    flags = false(1, size(rois, 3));
else
    flags = varargin{1};
end
[x, y] = ndgrid(linspace(-1, 1, size(rois, 1)), linspace(-1, 1, size(rois, 2)));
n = nterms;
%Hack for the case of using one line of Cartesian data
for indO = order:-1:0
    for indP = indO+1:-1:1
        geom = x.^(indP-1).*y.^(indO-indP+1);
        if theta == 90
            for ind = size(rois, 3):-1:1
                thisroi = rois(:, :, ind).*geom;
                if flags(ind)
                    weights(:, :, n, ind) = sum(thisroi, 2)*mean(img0(thisroi));
                else
                    weights(:, :, n, ind) = sum(thisroi.*img0, 2);
                end
            end
        elseif theta ==0
            for ind = size(rois, 3):-1:1
                thisroi = rois(:, :, ind).*geom;
                if flags(ind)
                    weights(:, :, n, ind) = sum(thisroi, 1)*mean(img0(thisroi));
                else
                    weights(:, :, n, ind) = sum(thisroi.*img0, 1);
                end
            end
        else
            for ind = size(rois, 3):-1:1
                thisroi = rois(:, :, ind).*geom;
                if flags(ind)
                    %     weights(:, :, ind) = radon(temp, theta);
```

```
                        weights(:, :, n, ind) = radon(thisroi,
theta)*mean(img0(thisroi));
                    else
                        weights(:, :, n, ind) = radon(thisroi.*real(img0),
theta)+i*radon(thisroi.*imag(img0), theta);
                    end
                end
            end
        n = n - 1;
    end
end
```

Bibliography

1.   Carmeliet P, Jain RK. Angiogenesis in cancer and other diseases. Nature 2000;407(6801):249-257.

2.   Miller JC, Pien HH, Sahani D, Sorensen AG, Thrall JH. Imaging angiogenesis: applications and potential for drug development. J Natl Cancer Inst 2005;97(3):172-187.

3.   Tofts PS, Brix G, Buckley DL, Evelhoch JL, Henderson E, Knopp MV, Larsson HB, Lee TY, Mayr NA, Parker GJ, Port RE, Taylor J, Weisskoff RM. Estimating kinetic parameters from dynamic contrast-enhanced T(1)-weighted MRI of a diffusable tracer: standardized quantities and symbols. Journal of magnetic resonance imaging : JMRI 1999;10(3):223-232.

4.   Kneeshaw PJ, Turnbull LW, Drew PJ. Current applications and future direction of MR mammography. Br J Cancer 2003;88(1):4-10.

5.   Drew PJ, Kerin MJ, Mahapatra T, Malone C, Monson JR, Turnbull LW, Fox JN. Evaluation of response to neoadjuvant chemoradiotherapy for locally advanced breast cancer with dynamic contrast-enhanced MRI of the breast. Eur J Surg Oncol 2001;27(7):617-620.

6.   Dowlati A, Robertson K, Cooney M, Petros WP, Stratford M, Jesberger J, Rafie N, Overmoyer B, Makkar V, Stambler B, Taylor A, Waas J, Lewin JS, McCrae KR, Remick SC. A phase I pharmacokinetic and translational study of the novel vascular targeting agent combretastatin a-4 phosphate on a single-dose intravenous schedule in patients with advanced cancer. Cancer Res 2002;62(12):3408-3416.

7. Leach MO, Brindle KM, Evelhoch JL, Griffiths JR, Horsman MR, Jackson A, Jayson G, Judson IR, Knopp MV, Maxwell RJ, McIntyre D, Padhani AR, Price P, Rathbone R, Rustin G, Tofts PS, Tozer GM, Vennart W, Waterton JC, Williams SR, Workman P. Assessment of antiangiogenic and antivascular therapeutics using MRI: recommendations for appropriate methodology for clinical trials. British Journal of Radiology 2003;76 Spec No 1:S87-91.

8. Leach MO, Brindle KM, Evelhoch JL, Griffiths JR, Horsman MR, Jackson A, Jayson GC, Judson IR, Knopp MV, Maxwell RJ, McIntyre D, Padhani AR, Price P, Rathbone R, Rustin GJ, Tofts PS, Tozer GM, Vennart W, Waterton JC, Williams SR, Workman P, Pharmacodynamic/Pharmacokinetic Technologies Advisory Committee DDOCRUK. The assessment of antiangiogenic and antivascular therapies in early-stage clinical trials using magnetic resonance imaging: issues and recommendations. British Journal of Cancer 2005;92(9):1599-1610.

9. Jackson A, O'Connor JP, Parker GJ, Jayson GC. Imaging tumor vascular heterogeneity and angiogenesis using dynamic contrast-enhanced magnetic resonance imaging. Clin Cancer Res 2007;13(12):3449-3459.

10. Pickup S, Zhou R, Glickson J. MRI estimation of the arterial input function in mice. Academic Radiology 2003;10(9):963-968.

11. O'Connor JP, Jackson A, Parker GJ, Jayson GC. DCE-MRI biomarkers in the clinical evaluation of antiangiogenic and vascular disrupting agents. Br J Cancer 2007;96(2):189-195.

12. McDonald DM, Baluk P. Significance of blood vessel leakiness in cancer. Cancer Research 2002;62(18):5381-5385.

13.   Kransdorf MJ, Murphey MD. Radiologic evaluation of soft-tissue masses: a current perspective. AJR American journal of roentgenology 2000;175(3):575-587.

14.   Sorensen AG. Magnetic resonance as a cancer imaging biomarker. J Clin Oncol 2006;24(20):3274-3281.

15.   Sourbron S, Heilmann M, Biffar A, Walczak C, Vautier J, Volk A, Peller M. Bolus-tracking MRI with a simultaneous T1 and T2* measurement. Magnetic Resonance in Medicine 2009;62(3):672-681.

16.   Jackson A, Jayson GC, Li KL, Zhu XP, Checkley DR, Tessier JJ, Waterton JC. Reproducibility of quantitative dynamic contrast-enhanced MRI in newly presenting glioma. British Journal of Radiology 2003;76(903):153-162.

17.   Kneeshaw PJ, Turnbull LW, Smith A, Drew PJ. Dynamic contrast enhanced magnetic resonance imaging aids the surgical management of invasive lobular breast cancer. Eur J Surg Oncol 2003;29(1):32-37.

18.   Hara N, Okuizumi M, Koike H, Kawaguchi M, Bilim V. Dynamic contrast-enhanced magnetic resonance imaging (DCE-MRI) is a useful modality for the precise detection and staging of early prostate cancer. Prostate 2005;62(2):140-147.

19.   Hawighorst H, Libicher M, Knopp MV, Moehler T, Kauffmann GW, Kaick G. Evaluation of angiogenesis and perfusion of bone marrow lesions: role of semiquantitative and quantitative dynamic MRI. J Magn Reson Imaging 1999;10(3):286-294.

20.   Padhani AR. MRI for assessing antivascular cancer treatments. British Journal of Radiology 2003;76 Spec No 1:S60-80.

21. Padhani AR, Husband JE. Dynamic contrast-enhanced MRI studies in oncology with an emphasis on quantification, validation and human studies. Clinical Radiology 2001;56(8):607-620.

22. Rehman S, Jayson GC. Molecular imaging of antiangiogenic agents. Oncologist 2005;10(2):92-103.

23. Hylton N. Dynamic contrast-enhanced magnetic resonance imaging as an imaging biomarker. J Clin Oncol 2006;24(20):3293-3298.

24. Zahra MA, Hollingsworth KG, Sala E, Lomas DJ, Tan LT. Dynamic contrast-enhanced MRI as a predictor of tumour response to radiotherapy. Lancet Oncol 2007;8(1):63-74.

25. Jarnagin WR, Schwartz LH, Gultekin DH, Gonen M, Haviland D, Shia J, D'Angelica M, Fong Y, Dematteo R, Tse A, Blumgart LH, Kemeny N. Regional chemotherapy for unresectable primary liver cancer: results of a phase II clinical trial and assessment of DCE-MRI as a biomarker of survival. Ann Oncol 2009;20(9):1589-1595.

26. Pickles MD, Manton DJ, Lowry M, Turnbull LW. Prognostic value of pre-treatment DCE-MRI parameters in predicting disease free and overall survival for breast cancer patients undergoing neoadjuvant chemotherapy. Eur J Radiol 2009;71(3):498-505.

27. Haacke EM, Filleti CL, Gattu R, Ciulla C, Al-Bashir A, Suryanarayanan K, Li M, Latif Z, DelProposto Z, Sehgal V, Li T, Torquato V, Kanaparti R, Jiang J, Neelavalli J. New algorithm for quantifying vascular changes in dynamic contrast-enhanced MRI independent of absolute T1 values. Magn Reson Med 2007;58(3):463-472.

28. Aref M, Handbury JD, Xiuquan Ji J, Aref S, Wiener EC. Spatial and temporal resolution effects on dynamic contrast-enhanced magnetic resonance mammography. Magn Reson Imaging 2007;25(1):14-34.

29. Parker GJ, Padhani AR. T1-w DCE-MRI: T1-weighted Dynamic Contrast-enhanced MRI. In: Tofts P, editor. Quantitative MRI of the Brain: Measuring changes caused by disease. Chichester: John Wiley & Sons; 2004. p 341-364.

30. Haacke EM. Fast imaging in the steady state. Magnetic Resonance Imaging: Physical Principles and Sequence Design. New York: John Wiley & Sons; 1999. p 703-740.

31. Schabel MC, Parker DL. Uncertainty and bias in contrast concentration measurements using spoiled gradient echo pulse sequences. Phys Med Biol 2008;53(9):2345-2373.

32. Jansen SA, Shimauchi A, Zak L, Fan X, Wood AM, Karczmar GS, Newstead GM. Kinetic Curves of Malignant Lesions Are Not Consistent Across MRI Systems: Need for Improved Standardization of Breast Dynamic Contrast-Enhanced MRI Acquisition. Am J Roentgenol 2009;193(3):832-839.

33. Hayes C, Padhani AR, Leach MO. Assessing changes in tumour vascular function using dynamic contrast-enhanced magnetic resonance imaging. NMR in Biomedicine 2002;15(2):154-163.

34. Walker-Samuel S, Leach MO, Collins DJ. Evaluation of response to treatment using DCE-MRI: the relationship between initial area under the gadolinium curve (IAUGC) and quantitative pharmacokinetic analysis. Physics in Medicine & Biology 2006;51(14):3593-3602.

35. Roberts C, Issa B, Stone A, Jackson A, Waterton JC, Parker GJ. Comparative study into the robustness of compartmental modeling and model-free analysis in DCE-MRI studies. Journal of Magnetic Resonance Imaging 2006;23(4):554-563.

36. Kety S. The Theory and Applications of the Exchange of Inert Gas at the Lungs and Tissues. Pharmacological Reviews 1951;3(1):1-41.

37. Harrer JU, Parker GJ, Haroon HA, Buckley DL, Embelton K, Roberts C, Baleriaux D, Jackson A. Comparative study of methods for determining vascular permeability and blood volume in human gliomas. Journal of Magnetic Resonance Imaging 2004;20(5):748-757.

38. Haroon HA, Buckley DL, Patankar TA, Dow GR, Rutherford SA, Baleriaux D, Jackson A. A comparison of Ktrans measurements obtained with conventional and first pass pharmacokinetic models in human gliomas. Journal of Magnetic Resonance Imaging 2004;19(5):527-536.

39. Buckley DL. Uncertainty in the analysis of tracer kinetics using dynamic contrast-enhanced T1-weighted MRI. Magnetic Resonance in Medicine 2002;47(3):601-606.

40. Larsson HB, Stubgaard M, Sondergaard L, Henriksen O. In vivo quantification of the unidirectional influx constant for Gd-DTPA diffusion across the myocardial capillaries with MR imaging. Journal of Magnetic Resonance Imaging 1994;4(3):433-440.

41. Larsson HB, Rosenbaum S, Fritz-Hansen T. Quantification of the effect of water exchange in dynamic contrast MRI perfusion measurements in the brain and heart. Magnetic Resonance in Medicine 2001;46(2):272-281.

42. Li KL, Jackson A. New hybrid technique for accurate and reproducible quantitation of dynamic contrast-enhanced MRI data. Magnetic Resonance in Medicine 2003;50(6):1286-1295.

43. St Lawrence KS, Lee TY. An adiabatic approximation to the tissue homogeneity model for water exchange in the brain: I. Theoretical derivation. Journal of cerebral blood flow and metabolism : official journal of the International Society of Cerebral Blood Flow and Metabolism 1998;18(12):1365-1377.

44. St Lawrence KS, Lee TY. An adiabatic approximation to the tissue homogeneity model for water exchange in the brain: II. Experimental validation. Journal of cerebral blood flow and metabolism : official journal of the International Society of Cerebral Blood Flow and Metabolism 1998;18(12):1378-1385.

45. Pont F, Duvillard L, Verges B, Gambert P. Development of compartmental models in stable-isotope experiments: application to lipid metabolism. Arterioscler Thromb Vasc Biol 1998;18(6):853-860.

46. Koh TS, Zeman V, Darko J, Lee TY, Milosevic MF, Haider M, Warde P, Yeung IW. The inclusion of capillary distribution in the adiabatic tissue homogeneity model of blood flow. Physics in medicine and biology 2001;46(5):1519-1538.

47. Phongkitkarun S, Kobayashi S, Kan Z, Lee TY, Charnsangavej C. Quantification of angiogenesis by functional computed tomography in a Matrigel model in rats. Academic Radiology 2004;11(5):573-582.

48. Schalla M, Weiss M. Pharmacokinetic curve fitting using numerical inverse Laplace transformation. European Journal of Pharmaceutical Sciences 1999;7(4):305-309.

49. Yankeelov TE, Rooney WD, Li X, Springer CS, Jr. Variation of the relaxographic "shutter-speed" for transcytolemmal water exchange affects the CR bolus-tracking curve shape. Magnetic Resonance in Medicine 2003;50(6):1151-1169.

50. Kim S, Quon H, Loevner LA, Rosen MA, Dougherty L, Kilger AM, Glickson JD, Poptani H. Transcytolemmal water exchange in pharmacokinetic analysis of dynamic contrast-enhanced MRI data in squamous cell carcinoma of the head and neck. Journal of magnetic resonance imaging : JMRI 2007;26(6):1607-1617.

51.   Schmid VJ, Whitcher B, Padhani AR, Yang GZ. Quantitative Analysis of Dynamic Contrast-Enhanced MR Images Based on Bayesian P-Splines. Ieee Transactions on Medical Imaging 2009;28(6):789-798.

52.   Sourbron S, Dujardin M, Makkat S, Luypaert R. Pixel-by-pixel deconvolution of bolus-tracking data: optimization and implementation. Physics in medicine and biology 2007;52(2):429-447.

53.   Dale BM, Jesberger JA, Lewin JS, Hillenbrand CM, Duerk JL. Determining and optimizing the precision of quantitative measurements of perfusion from dynamic contrast enhanced MRI. J Magn Reson Imaging 2003;18(5):575-584.

54.   Dowell NG, Tofts PS. Fast, accurate, and precise mapping of the RF field in vivo using the 180 degrees signal null. Magn Reson Med 2007;58(3):622-630.

55.   Evelhoch JL. Key factors in the acquisition of contrast kinetic data for oncology. Journal of Magnetic Resonance Imaging 1999;10(3):254-259.

56.   Henderson E, Rutt BK, Lee TY. Temporal sampling requirements for the tracer kinetics modeling of breast disease. Magn Reson Imaging 1998;16(9):1057-1073.

57.   Yang C, Karczmar GS, Medved M, Stadler WM. Estimating the arterial input function using two reference tissues in dynamic contrast-enhanced MRI studies: fundamental concepts and simulations. Magn Reson Med 2004;52(5):1110-1117.

58.   Cheng HL. T1 measurement of flowing blood and arterial input function determination for quantitative 3D T1-weighted DCE-MRI. J Magn Reson Imaging 2007;25(5):1073-1078.

59.   Faranesh AZ, Yankeelov TE. Incorporating a vascular term into a reference region model for the analysis of DCE-MRI data: a simulation study. Phys Med Biol 2008;53(10):2617-2631.

60.   McIntyre DJ, Ludwig C, Pasan A, Griffiths JR. A method for interleaved
        acquisition of a vascular input function for dynamic contrast-enhanced MRI in
        experimental rat tumours. NMR Biomed 2004;17(3):132-143.

61.   Parker GJ, Roberts C, Macdonald A, Buonaccorsi GA, Cheung S, Buckley DL, Jackson
        A, Watson Y, Davies K, Jayson GC. Experimentally-derived functional form for a
        population-averaged high-temporal-resolution arterial input function for dynamic
        contrast-enhanced MRI. Magn Reson Med 2006;56(5):993-1000.

62.   Walker-Samuel S, Leach MO, Collins DJ. Reference tissue quantification of DCE-MRI
        data without a contrast agent calibration. Physics in Medicine & Biology
        2007;52(3):589-601.

63.   Yankeelov TE, Cron GO, Addison CL, Wallace JC, Wilkins RC, Pappas BA, Santyr
        GE, Gore JC. Comparison of a reference region model with direct measurement of an
        AIF in the analysis of DCE-MRI data. Magnetic Resonance in Medicine
        2007;57(2):353-361.

64.   Leach MO, Brindle KM, Evelhoch JL, Griffiths JR, Horsman MR, Jackson A, Jayson
        G, Judson IR, Knopp MV, Maxwell RJ, McIntyre D, Padhani AR, Price P, Rathbone R,
        Rustin G, Tofts PS, Tozer GM, Vennart W, Waterton JC, Williams SR, Workman P.
        Assessment of antiangiogenic and antivascular therapeutics using MRI:
        recommendations for appropriate methodology for clinical trials. Br J Radiol 2003;76
        Spec No 1:S87-91.

65.   Cheng HL. Investigation and optimization of parameter accuracy in dynamic contrast-
        enhanced MRI. J Magn Reson Imaging 2008;28(3):736-743.

66. Hansen A, Pedersen H, Rostrup E, Larsson HB. Partial volume effect (PVE) on the arterial input function (AIF) in T1-weighted perfusion imaging and limitations of the multiplicative rescaling approach. Magnetic resonance in medicine 2009;In press.

67. Ahearn TS, Staff RT, Redpath TW, Semple SI. The effects of renal variation upon measurements of perfusion and leakage volume in breast tumours. Phys Med Biol 2004;49(10):2041-2051.

68. Karmonik C, Jackson EF. Monte-Carlo simulation study to determine the confidence limits for the plasma and tissue concentration time curves in dynamic Gd-DTPA enhanced MRI. 1999; Philadelphia, PA.

69. Zhou R, Pickup S, Yankeelov TE, Springer CS, Jr., Glickson JD. Simultaneous measurement of arterial input function and tumor pharmacokinetics in mice by dynamic contrast enhanced imaging: effects of transcytolemmal water exchange. Magnetic Resonance in Medicine 2004;52(2):248-257.

70. Roberts C, Buckley DL, Parker GJ. Comparison of errors associated with single- and multi-bolus injection protocols in low-temporal-resolution dynamic contrast-enhanced tracer kinetic analysis. Magn Reson Med 2006;56(3):611-619.

71. Yankeelov TE, Luci JJ, Lepage M, Li R, Debusk L, Lin PC, Price RR, Gore JC. Quantitative pharmacokinetic analysis of DCE-MRI data without an arterial input function: a reference region model. Magnetic Resonance Imaging 2005;23(4):519-529.

72. Weinnman HJ, Laniado M, Mutzel W. Pharmacokinetics of GdDTPA/Dimeglumine after IV injection into healthy volunteers. Physiological Chemistry and Physics and Medical NMR 1984;16(2):167-172.

73. Tofts PS, Kermode AG. Measurement of the blood-brain barrier permeability and leakage space using dynamic MR imaging. 1. Fundamental concepts. Magn Reson Med 1991;17(2):357-367.

74. Port RE, Knopp MV, Brix G. Dynamic contrast-enhanced MRI using Gd-DTPA: interindividual variability of the arterial input function and consequences for the assessment of kinetics in tumors. Magnetic Resonance in Medicine 2001;45(6):1030-1038.

75. Ashton E, Raunig D, Ng C, Kelcz F, McShane T, Evelhoch J. Scan-rescan variability in perfusion assessment of tumors in MRI using both model and data-derived arterial input functions. J Magn Reson Imaging 2008;28(3):791-796.

76. Wang Y, Huang W, Panicek DM, Schwartz LH, Koutcher JA. Feasibility of using limited-population-based arterial input function for pharmacokinetic modeling of osteosarcoma dynamic contrast-enhanced MRI data. Magn Reson Med 2008;59(5):1183-1189.

77. Rausch M, Scheffler K, Rudin M, Radu EW. Analysis of input functions from different arterial branches with gamma variate functions and cluster analysis for quantitative blood volume measurements. Magn Reson Imaging 2000;18(10):1235-1243.

78. Mouridsen K, Christensen S, Gyldensted L, Ostergaard L. Automatic selection of arterial input function using cluster analysis. Magn Reson Med 2006;55(3):524-531.

79. Simpson NE, He Z, Evelhoch JL. Deuterium NMR tissue perfusion measurements using the tracer uptake approach: I. Optimization of methods. Magn Reson Med 1999;42(1):42-52.

80. Walker-Samuel S, Parker CC, Leach MO, Collins DJ. Reproducibility of reference tissue quantification of dynamic contrast-enhanced data: comparison with a fixed vascular input function. Physics in Medicine & Biology 2007;52(1):75-89.

81. Planey CR, Welch EB, Xu L, Chakravarthy AB, Gatenby JC, Freehardt D, Mayer I, Meszeoly I, Kelley M, Means-Powell J, Gore JC, Yankeelov TE. Temporal sampling requirements for reference region modeling of DCE-MRI data in human breast cancer. Journal of Magnetic Resonance Imaging 2009;30(1):121-134.

82. Taylor NJ, Rowland IJ, Tanner SF, Leach MO. A rapid interleaved method for measuring signal intensity curves in both blood and tissue during contrast agent administration. Magn Reson Med 1993;30(6):744-749.

83. Haacke EM. Introductory Signal Acquisition Methods. Magnetic Resonance Imaging: Physical Principles and Sequence Design. New York: John Wiley & Sons; 1999. p 111-137.

84. Haacke EM, Brown RW, Thompson MR, Venkatesan R. A Closer Look at RF Pulses. Magnetic Resonance Imaging: Physical Principles and Sequence Design. New York: John Wiley & Sons; 1999.

85. Hinshaw WS, Lent AH. An Introduction to Nmr Imaging - from the Bloch Equation to the Imaging Equation. Proceedings of the Ieee 1983;71(3):338-350.

86. Doddrell DM, Bulsing JM, Galloway GJ, Brooks WM, Field J, Irving M, Baddeley H. Discrete Isolation from Gradient-Governed Elimination of Resonances - Digger, a New Technique for Invivo Volume-Selected Nmr-Spectroscopy. Journal of Magnetic Resonance 1986;70(2):319-326.

87. Hartley CJ, Michael LH, Entman ML. Noninvasive measurement of ascending aortic blood velocity in mice. Am J Physiol 1995;268(1 Pt 2):H499-505.

88. Peters DC, Korosec FR, Grist TM, Block WF, Holden JE, Vigen KK, Mistretta CA. Undersampled projection reconstruction applied to MR angiography. Magn Reson Med 2000;43(1):91-101.

89. Vigen KK, Peters DC, Grist TM, Block WF, Mistretta CA. Undersampled projection-reconstruction imaging for time-resolved contrast-enhanced imaging. Magn Reson Med 2000;43(2):170-176.

90. Tsao J, Boesiger P, Pruessmann KP. k-t BLAST and k-t SENSE: dynamic MRI with high frame rate exploiting spatiotemporal correlations. Magn Reson Med 2003;50(5):1031-1042.

91. Gamper U, Boesiger P, Kozerke S. Compressed sensing in dynamic MRI. Magn Reson Med 2008;59(2):365-373.

92. Jung H, Ye JC, Kim EY. Improved k-t BLAST and k-t SENSE using FOCUSS. Phys Med Biol 2007;52(11):3201-3226.

93. Lustig M, Donoho D, Pauly JM. Sparse MRI: The application of compressed sensing for rapid MR imaging. Magn Reson Med 2007;58(6):1182-1195.

94. Johnson KM, Velikina J, Wu Y, Kecskemeti S, Wieben O, Mistretta CA. Improved waveform fidelity using local HYPR reconstruction (HYPR LR). Magn Reson Med 2008;59(3):456-462.

95. Mistretta CA, Wieben O, Velikina J, Block W, Perry J, Wu Y, Johnson K, Wu Y. Highly constrained backprojection for time-resolved MRI. Magn Reson Med 2006;55(1):30-40.

96. O'Halloran RL, Wen Z, Holmes JH, Fain SB. Iterative projection reconstruction of time-resolved images using highly-constrained back-projection (HYPR). Magn Reson Med 2008;59(1):132-139.

97.   Wu Y, Wieben O, Mistretta CA, Korosec FR. Evaluation of temporal and spatial characteristics of 2D HYPR processing using simulations. Magn Reson Med 2008;59(5):1090-1098.

98.   Hanson JM, Liang ZP, Wiener EC, Lauterbur PC. Fast dynamic imaging using two reference images. Magn Reson Med 1996;36(1):172-175.

99.   Liang ZP, Lauterbur PC. A generalized series approach to MR spectroscopic imaging. IEEE Trans Med Imaging 1991;10(2):132-137.

100.   Liang ZP, Lauterbur PC. An efficient method for dynamic magnetic resonance imaging. IEEE Trans Med Imaging 1994;13(4):677-686.

101.   Webb AG, Liang ZP, Magin RL, Lauterbur PC. Applications of reduced-encoding MR imaging with generalized-series reconstruction (RIGR). J Magn Reson Imaging 1993;3(6):925-928.

102.   Xu D, Liang ZP, Wu Y, Kevin Hitchens T, Ho C. High-resolution dynamic imaging of contrast agent uptake in a beating heart. Conf Proc IEEE Eng Med Biol Soc 2005;7:7397-7400.

103.   Xu D, Ying L, Liang ZP. Parallel generalized series MRI: algorithm and application to cancer imaging. Conf Proc IEEE Eng Med Biol Soc 2004;2:1052-1055.

104.   Heidemann RM, Ozsarlak O, Parizel PM, Michiels J, Kiefer B, Jellus V, Muller M, Breuer F, Blaimer M, Griswold MA, Jakob PM. A brief review of parallel magnetic resonance imaging. Eur Radiol 2003;13(10):2323-2337.

105.   Tsao J, Behnia B, Webb AG. Unifying linear prior-information-driven methods for accelerated image acquisition. Magn Reson Med 2001;46(4):652-660.

106. Liang ZP, Madore B, Glover GH, Pelc NJ. Fast algorithms for GS-model-based image reconstruction in data-sharing Fourier imaging. IEEE Trans Med Imaging 2003;22(8):1026-1030.

107. Hu X, Levin DN, Lauterbur PC, Spraggins T. SLIM: spectral localization by imaging. Magnetic Resonance in Medicine 1988;8(3):314-322.

108. Kak AC, Slaney M. 7 Algebraic Reconstruction Algorithms. Principles of Computerized Tomographic Imaging; 1988.

109. Liang ZP. Spatiotemporal imaging with partially separable functions. 2007; Proceedings of the NFSI & ICFBI. p 181-182.

110. Foster M. An Application of the Wiener-Kolmogorov Smoothing Theory to Matrix Inversion. Journal of the Society for Industrial and Applied Mathematics 1961;9(3):387-392.

111. Aerts HJ, van Riel NA, Backes WH. System identification theory in pharmacokinetic modeling of dynamic contrast-enhanced MRI: influence of contrast injection. Magnetic resonance in medicine : official journal of the Society of Magnetic Resonance in Medicine / Society of Magnetic Resonance in Medicine 2008;59(5):1111-1119.

112. Padhani AR, Hayes C, Landau S, Leach MO. Reproducibility of quantitative dynamic MRI of normal human tissues. NMR in Biomedicine 2002;15(2):143-153.

113. Larson AC, White RD, Laub G, McVeigh ER, Li D, Simonetti OP. Self-gated cardiac cine MRI. Magnetic Resonance in Medicine 2004;51(1):93-102.

114. Esparza-Coss E, Ramirez MS, Bankson JA. Wireless self-gated multiple-mouse cardiac cine MRI. Magnetic Resonance in Medicine 2008;59(5):1203-1206.

115. Polson MJ, Barker AT, Gardiner S. The effect of rapid rise-time magnetic fields on the ECG of the rat. Clinical Physics & Physiological Measurement 1982;3(3):231-234.

116. Gill PE, Murray W. Algorithms for Solution of Non-Linear Least-Squares Problem. Siam J Numer Anal 1978;15(5):977-992.

117. Lawson RS. Application of mathematical methods in dynamic nuclear medicine studies. Physics in medicine and biology 1999;44(4):R57-98.

118. Hotelling H. The Generalization of Student's Ratio. The Annals of Mathematical Statistics 1931;2(3):360-378.

119. Ahearn TS, Staff RT, Redpath TW, Semple SI. The use of the Levenberg-Marquardt curve-fitting algorithm in pharmacokinetic modelling of DCE-MRI data. Physics in Medicine & Biology 2005;50(9):N85-92.

120. Nilsson M, Connell MA, Davis AL, Morris GA. Biexponential fitting of diffusion-ordered NMR data: practicalities and limitations. Anal Chem 2006;78(9):3040-3045.

121. King MA, Doherty PW, Schwinger RB, Penney BC. A Wiener filter for nuclear medicine images. Med Phys 1983;10(6):876-880.

122. Wink AM, Roerdink JB. Denoising functional MR images: a comparison of wavelet denoising and Gaussian smoothing. IEEE Trans Med Imaging 2004;23(3):374-387.

Vita

Dustin Kenneth Ragan was born in the city of Greeneville, TX, on January 15, 1981, the son of Ken and Jennie Ragan. He graduated from Sulphur Springs High School in 1999, after which he attended Trinity University. In 2003, Dustin graduated from Trinity with a Bachelors of Arts in Mathematics and Physics, and that fall he matriculated into The University of Texas Health Science Center at Houston Graduate School of Biomedical Sciences. In 2006 he received the degree of Master of Science and continued his graduate studies. Sometime later, on Pi Day 2009, he married Gwendolyn Maria Bethenis Hoben and is looking forward to living happily ever after.